B Vi

INTRO

Quick Submit

Quick Submit

Indian Institute of Science Education and Research (IISER) Bhopal

Document Details

Submission ID
trn:oid:::1:3578509214

Submission Date
May 25, 2026, 1:18 PM GMT+5:30

Download Date
May 25, 2026, 2:01 PM GMT+5:30

File Name
thesis_-_Copy_1.pdf

File Size
3.1 MB

123 Pages

33,326 Words

192,310 Characters

6% Overall Similarity

The combined total of all matches, including overlapping sources, for each database.

Filtered from the Report

- Small Matches (less than 12 words)

Exclusions

- 4 Excluded Sources
- 4 Excluded Matches

Match Groups

113 Not Cited or Quoted 6%
Matches with neither in-text citation nor quotation marks

1 Missing Quotations 0%
Matches that are still very similar to source material

0 Missing Citation 0%
Matches that have quotation marks, but no in-text citation

0 Cited and Quoted 0%
Matches with in-text citation present, but no quotation marks

Top Sources

4% Internet sources
4% Publications
0% Submitted works (Student Papers)

Integrity Flags

2 Integrity Flags for Review

Replaced Characters
130 suspect characters on 35 pages
Letters are swapped with similar characters from another alphabet.

Hidden Text
29 suspect characters on 1 page
Text is altered to blend into the white background of the document.

Our system's algorithms look deeply at a document for any inconsistencies that would set it apart from a normal submission. If we notice something strange, we flag it for you to review.

A Flag is not necessarily an indicator of a problem. However, we'd recommend you focus your attention there for further review.

Match Groups

- **113** Not Cited or Quoted 6%
  Matches with neither in-text citation nor quotation marks
- **1** Missing Quotations 0%
  Matches that are still very similar to source material
- **0** Missing Citation 0%
  Matches that have quotation marks, but no in-text citation
- **0** Cited and Quoted 0%
  Matches with in-text citation present, but no quotation marks

Top Sources

4% Internet sources
4% Publications
0% Submitted works (Student Papers)

Top Sources

The sources with the highest number of matches within the submission. Overlapping sources will not be displayed.

1	Internet	
www.webtoons.com		<1%
2	Publication	
Ramcharan Meena, Rajendra S. Dhaka. "Dielectric properties and impedance spec...		<1%
3	Publication	
Vishal Singh, Bharti Singh. "MoS2-PVDF/PDMS Based Flexible Hybrid Piezo-Triboel...		<1%
4	Internet	
www.mdpi.com		<1%
5	Internet	
www.rsc.org		<1%
6	Publication	
Hou-Qing Wang, Jing-Wen Wang, Xin-Zhu Wang, Xin-Hua Gao, Guo-Chao Zhuang, ...		<1%
7	Internet	
arxiv.org		<1%
8	Publication	
Gagan Sharma, Deshraj Meena. "Optimization of SnO2/MXene/PVDF composites f...		<1%
9	Publication	
Vishal Singh, Deshraj Meena, Himani Sharma, Ashutosh Trivedi, Bharti Singh. "Inv...		<1%
10	Publication	
Shilpa Rana, Vishal Singh, Bharti Singh. "Recent trends in 2D materials and their ...		<1%

11 Publication
Vishal Singh, Bharti Singh. "PDMS/PVDF- MoS2 based flexible triboelectric nanoge... <1%

12 Internet
scholar.ufs.ac.za <1%

13 Publication
Huidrom Hemojit Singh, Simrjit Singh, Neeraj Khare. "Design of flexible PVDF/Na... <1%

14 Publication
Huidrom Hemojit Singh, Simrjit Singh, Neeraj Khare. " Enhanced -phase in PVDF ... <1%

15 Publication
H.C. Madhusudhana, S.N. Shobhadevi, B.M. Nagabhushana, B.V. Chaluvaraju et al... <1%

16 Internet
coek.info <1%

17 Internet
repository.um.edu.my <1%

18 Internet
www.coursehero.com <1%

19 Internet
mxeneconference.coe.drexel.edu <1%

20 Internet
files01.core.ac.uk <1%

21 Publication
Pei, Bo, Hongxu Yao, Weixin Zhang, and Zeheng Yang. "Hydrothermal synthesis o... <1%

22 Internet
iopscience.iop.org <1%

23 Internet
aaltodoc.aalto.fi <1%

24 Internet
esd.monroe-electronics.com <1%

25 Publication
Samarakoon, Disna Priyadarshani. "Effects of Processing Conditions and Testing ... <1%

26 Internet
manualzz.com <1%

27 Internet
theses.hal.science <1%

28 Publication
Eric Deconinck. "Spectroscopic techniques, from (onsite) screening and identificat... <1%

29 Publication
Kalim Deshmukh, M. Basheer Ahamed, Rajendra R. Deshmukh, Kishor Kumar Sad... <1%

30 Publication
Yixuan Liu, Wenhua Xue, Jian Ye, Ruilong Zhang, Yuchao Shao, Akkammagari Putt... <1%

31 Internet
scholar.hit.edu.cn <1%

32 Internet
tudr.thapar.edu <1%

33 Internet
www.frontiersin.org <1%

34 Internet
www.u-ldevinci.fr <1%

35 Publication
A. T. Raghavender. "Dielectric properties of Al-substituted Co ferrite nanoparticle... <1%

36 Publication
David A. Sager. "Diffusion of Neodymium into Sputtered Films of Tantalum Pento... <1%

37 Publication
Kyu-Seog Hwang, Tae-Il Choi, Seung Hwangbo. "Electrostatic Spraying Deposition... <1%

38 Internet
dyuthi.cusat.ac.in <1%

39 Internet
hdl.handle.net <1%

40 Internet
ksascholar.dri.sa <1%

41 Internet
library.iyte.edu.tr <1%

42 Internet
uh-ir.tdl.org <1%

43 Internet
vjs.ac.vn <1%

44 Internet
www.erbium.nl <1%

45 Internet
www2.mdpi.com <1%

46 Publication
Fogg, Joshua James. "Au(Hkl): Surface X-Ray Diffraction Studies at the Electroche... <1%

47 Publication
K. Vijaya Sankar, R. Kalai Selvan. "Fabrication of flexible fiber supercapacitor usin... <1%

48 Publication
Rajinder Pal. "Rheology of Particulate Dispersions and Composites", CRC Press, 20... <1%

49 Internet
eprints.lib.hokudai.ac.jp <1%

50 Internet
scholar.uoc.ac.in <1%

51 Internet
sutir.sut.ac.th:8080 <1%

52 Internet
www.jstage.jst.go.jp <1%

53 Publication
Babak Jaleh, Shima Sodagar, Amir Momeni, Ameneh Jabbari. "Nanodiamond parti... <1%

54 Publication
C. Joseph, P. Bourson, M. D. Fontana. "Amorphous to crystalline transformation in... <1%

55 Publication
Govind Shreenivas Ekbote, Mohammed Khalifa, Balasubramanian Venkatesa Per... <1%

56 Publication
Nitesh Kumar NATH, Rajanikanta PARIDA, Bichitra Nanda PARIDA, Nimai C. NAYA... <1%

57 Publication
Qian Wu, Mandi Fang, Shizhe Jiao, Siyuan Li et al. "Phase regulation enabling den... <1%

58 Publication
Qinghuang Lin. "Low dielectric constant nanocomposite thin films based on silica... <1%

59 Publication
Shamsuzzaman, Hena Khanam, Ashraf Mashrai, Mohd Asif, Abad Ali, Assem Bara... <1%

60 Publication
Shenglin Jiang, Hongyan Wan, Huan Liu, Yike Zeng, Jianguo Liu, Yunyi Wu, Guang... <1%

61 Publication
Shobhna Choudhary, R. J. Sengwa. "Investigation on Structural and Dielectric Pro... <1%

62 Internet
dokumen.pub <1%

63 Internet
dypatilunikop.org <1%

64 Internet
ir.unisa.ac.za <1%

65 Internet
link.springer.com <1%

66 Internet
neuroquantology.com <1%

67 Internet

next.gr <1%

68 Internet

pure.uos.ac.kr <1%

69 Internet

scienary.blog <1%

70 Internet

sioc-journal.cn <1%

71 Internet

www.freepatentsonline.com <1%

CHAPTER 1

Introduction

This chapter provides a comprehensive introduction to the growing demand for sustainable green energy and the critical role of mechanical energy harvesters in addressing this global challenge. The rapid expansion of wireless networks and wearable electronics imposes severe constraints on traditional, battery-reliant power supplies. Therefore, the development of renewable and independent power sources has become a fundamental necessity. There are various established energy harvesting principles including electromagnetic, thermoelectric, triboelectric, and piezoelectric mechanisms etc. Herein, a specific focus is placed on piezoelectric and triboelectric nanogenerators (PENGs and TENGs) that include their fabrication, working principles and the real time applications. As they have drawn significant attention for their ability to harvest ubiquitous ambient mechanical energy from human motion, wind, and fluid flow. However, these nanogenerators alone do not work properly for continuous device operation as their electrical output from ambient mechanical stimuli is inherently irregular and intermittent. To resolve this, the chapter also introduces the vital integration of energy storage configurations, specifically detailing the development of self-charging piezo-supercapacitors. By using materials that have the potential to harvest as well as store energy, a self-charging device can be prepared. By coupling these two systems in one, the device can effectively buffer fluctuating voltages, providing a stable, uninterrupted power supply for next-generation self-powered sensors and wearable electronics. The chapter finally concludes with the brief description of the objectives and layout of the thesis.

1.1 Overview

The escalating global demand for energy, started by rapid industrialization and a surging population that has placed an immense strain on tradition power generation infrastructures. For over a century, the global economy has been inextricably linked to the combustion of fossil fuels. However, these non-renewable resources are finite in nature. Additionally, they have the catastrophic environmental consequences of greenhouse gas emissions that has forced a critical paradigm shift [1,2]. Therefore, the transition toward sustainable and renewable energy generation is no longer merely advantageous, it is an absolute global requirement. Various sustainable and renewable energy sources present in our surroundings has been shown in Figure 1.1. While large-scale renewable sources such as solar and wind power are highly recognized, they exhibit fundamental intermittency. Solar energy is strictly governed by sun cycles, weather patterns, and the angle of incidence, rendering it highly unreliable for continuous indoor or night time operation [3,4]. Thermoelectric generators (TEGs), which exploit the Seebeck effect to convert thermal gradients into electricity, perform optimally in industries with extreme heat dissipation. However, they suffer massive efficiency drops in tropical or ambient climates [5,6]. Additionally, their high energy production is not suitable for powering small wearable and portable electronic gadgets. Among these environmental and operational constraints, wasted mechanical energy emerges as an exceptionally reliable and weather-independent resource. Ambient mechanical vibrations are omnipresent. They originate from the operation of industrial machinery, aerodynamic flows, and routine human physiological movements (such as locomotion, respiration, and cardiac rhythms) [7–9]. This represents a vast, underutilized reservoir of energy spanning a broad frequency spectrum.

Concurrently, with the bigger picture of energy crisis, a parallel technological revolution at small level is also crucial. The relentless progression of nanotechnology and micro-electromechanical systems (MEMS) has precipitated a massive influx of multifunctional, miniaturized, and portable electronic devices [10]. World is currently witnessing a transformative era defined by the Internet of Things (IoT), wireless sensor networks (WSN), and implantable biomedical devices etc. Crucially, the power consumption of these smart sensors has dropped from the milliwatt (mW) range down to the microwatt (μW) range [11,12]. This drastic reduction in power requirements has opened a highly viable pathway for ambient energy harvesting. The energy such as body moments, vibrations etc. that is traditionally dissipated as waste in the ambient environment can

be captured systematically. And this captured energy can be converted into a regulated, functional electrical form that can be useful for low power electronics [13,14].

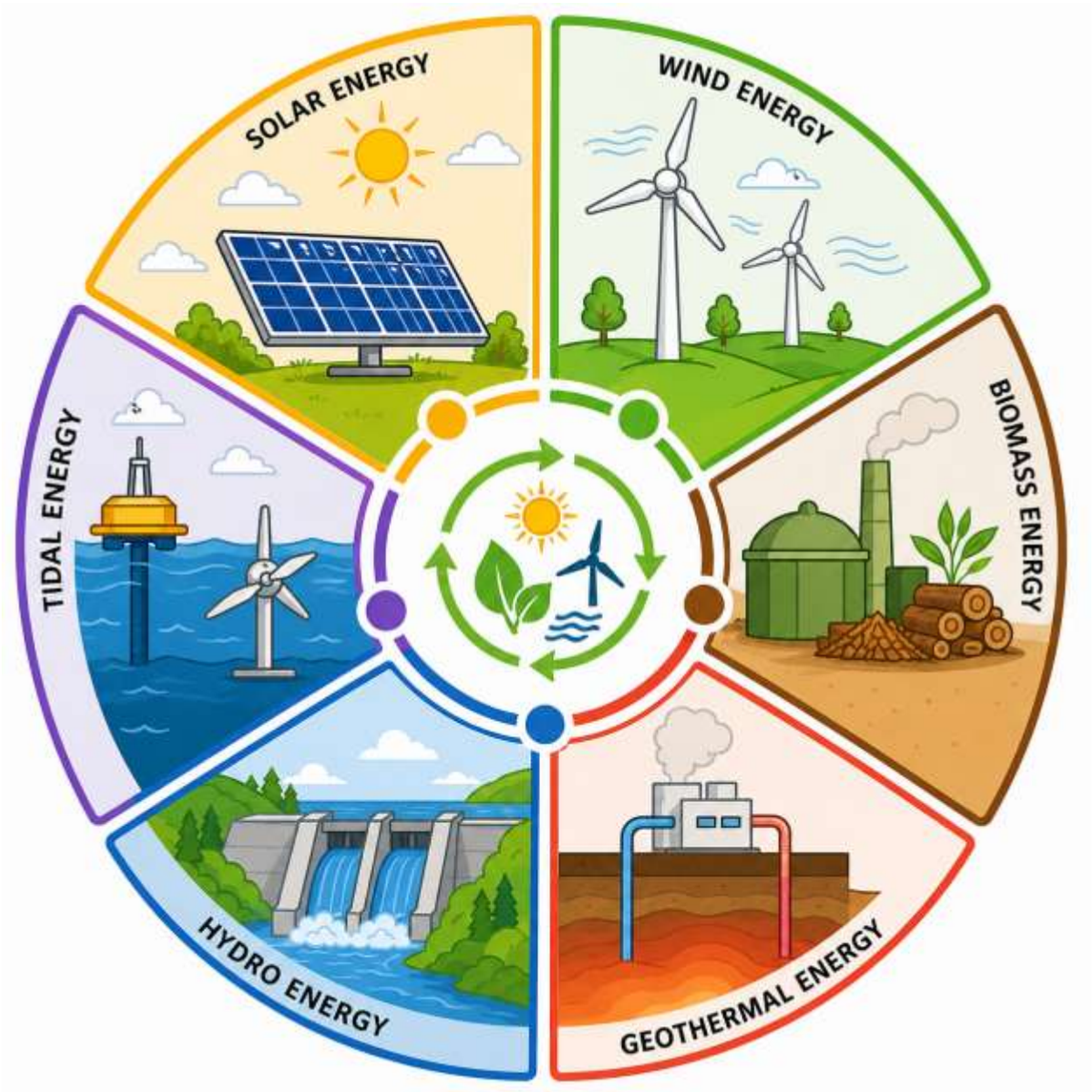

Figure 1.1. A schematic illustration of different renewable energy sources present in our surroundings (created using ChatGPT/DALL·E AI tool)

Presently, the universal solution for powering these portable and remote electronic systems relies on electrochemical batteries, predominantly Lithium-ion (Li-ion) cells. While these conventional power sources suffer from several intrinsic limitations such as, finite operational lifespan and fundamentally constrained by limited charging and discharging cycles [15,16]. These constraints critically hinder the deployment of next-generation, self-sustained electronic systems. This necessitates periodic maintenance and replacement, which is economically and logistically unfeasible for large-scale, decentralized sensory networks or surgically implanted bio-devices. The lifecycle of chemical batteries (from the extraction of rare-earth metals to their eventual disposal)

also poses severe environmental hazards including heavy metal leaching and soil contamination. Furthermore, traditional electrochemical cells are inherently rigid and possess high mass densities. As modern electronics evolve toward skin-like, conformal, lightweight and flexible architectures, the rigidity of conventional batteries serves as a primary physical setback [17,18]. As United states of America predicted that the consumer market of flexible materials will raise to 3800.39 million USD in 2026, which was 996.5 million USD in 2020 [19]. This rapid growth shows the major significance of flexible materials in upcoming time.

To prepare flexible devices for harvesting the wasted mechanical energy successfully, a fundamental redesign of the harvester's physical structure is necessary. To efficiently couple with the human body or dynamic structural components without causing mechanical impedance or discomfort, the energy-harvesting device must be structurally compliant. Rigid ceramic piezoelectric materials (ex., Lead Zirconate Titanate) are susceptible to brittle fracture and fatigue failure under cyclic loading [20]. Consequently, there is an urgent demand for flexible, lightweight and mechanically stable nanocomposites that can withstand high-strain deformations over millions of cycles while maintaining superior electromechanical energy conversion efficiencies.

Within this context, the present thesis elucidates advanced methodologies for extracting ambient mechanical energy by using both piezoelectric and triboelectric phenomenon. While each physical mechanism is highly potent independently, they also exhibit complementary electrical characteristics in hybrid mode. The central focus of this research is dedicated to the development of the hybrid devices that can extract mechanical energy and can also store the extracted energy. This work aims to prepare efficient PVDF nanocomposites based piezoelectric and triboelectric nanogenerators. Additionally, to engineer a flexible nanogenerator that can also solve the power fluctuation problem and is robustly flexible, economically scalable, and environment friendly. Ultimately, this research strives to advance the paradigm of energy harvesting beyond instantaneous power generation toward the realization of fully integrated self-charging piezo-supercapacitors, thereby providing a sustainable and ecologically responsible solution to the future demands of global micro-electronics.

1.2 Nanogenerators for Mechanical Energy Harvesting

Nanogenerators represent a paradigm-shifting technology designed to convert ambient mechanical energy into functional electrical signal at the micro and nanoscale. As the global technological ecosystem rapidly expands to include the Internet of Things (IoT), implantable biomedical devices, and flexible wearable electronics, the demand for decentralized and sustainable power solutions has intensified [21]. Nanogenerators directly address this demand by scavenging localized, low-frequency mechanical energy that is otherwise dissipated as waste heat or sound. By establishing a reliable and continuous power supply, these compact devices eliminate the traditional reliance on electrochemical batteries. As they effectively overcome the limitations associated with finite operational lifespans, rigidness, and the ecological burden of chemical waste disposal [22].

The history of this transformative field can be traced back to 2006, marked by the pathbreaking work of Professor Zhong Lin Wang and his research group. They conceptualized and successfully demonstrated the first piezoelectric nanogenerator by utilizing the unique electromechanical properties of one-dimensional nanomaterials [23,24]. In their experiment, a conductive Atomic Force Microscope (AFM) tip was used to mechanically deflect vertically aligned Zinc Oxide (ZnO) nanowires. This nanoscale deformation induced a strain-driven charge separation across the nanowire, and the resulting potential difference was measured as a measurable electrical output. This fundamental breakthrough established a completely new paradigm for solid-state power generation, proving that nanomaterials could effectively convert minute, ambient forces into electricity via the piezoelectric effect.

Building upon the success of piezoelectric energy harvesting, Professor Wang's group introduced a secondary, equally revolutionary energy harvesting mechanism in 2012 i.e., Triboelectric Nanogenerator (TENG) [25]. This innovative approach harnessed the ubiquitous phenomena of contact electrification and electrostatic induction. When two materials with differing electron affinities are brought into physical contact and subsequently separated, a surface charge transfer occurs that establish a strong potential difference. The inherent flexibility, coupled with high power output, cost-effectiveness, and facile fabrication, has made these nanogenerators a focal point for modern sustainable energy solutions [26]. Additionally, the generated electrical signal (voltage or current) is directly proportional to the applied mechanical stimulus, these devices do not require an external power source to operate. This leads to their direct application in advanced

motion tracking, tactile and pressure sensing, human-machine interfaces, and structural health monitoring [26–31]. Figure 1.2 illustrates the different applications of nanogenerators in this world. The forthcoming sections of this chapter will provide a comprehensive description of both piezoelectric and triboelectric nanogenerators along with their fundamental operational mechanisms. Moreover, chapter also explore the specific material requirements for practical

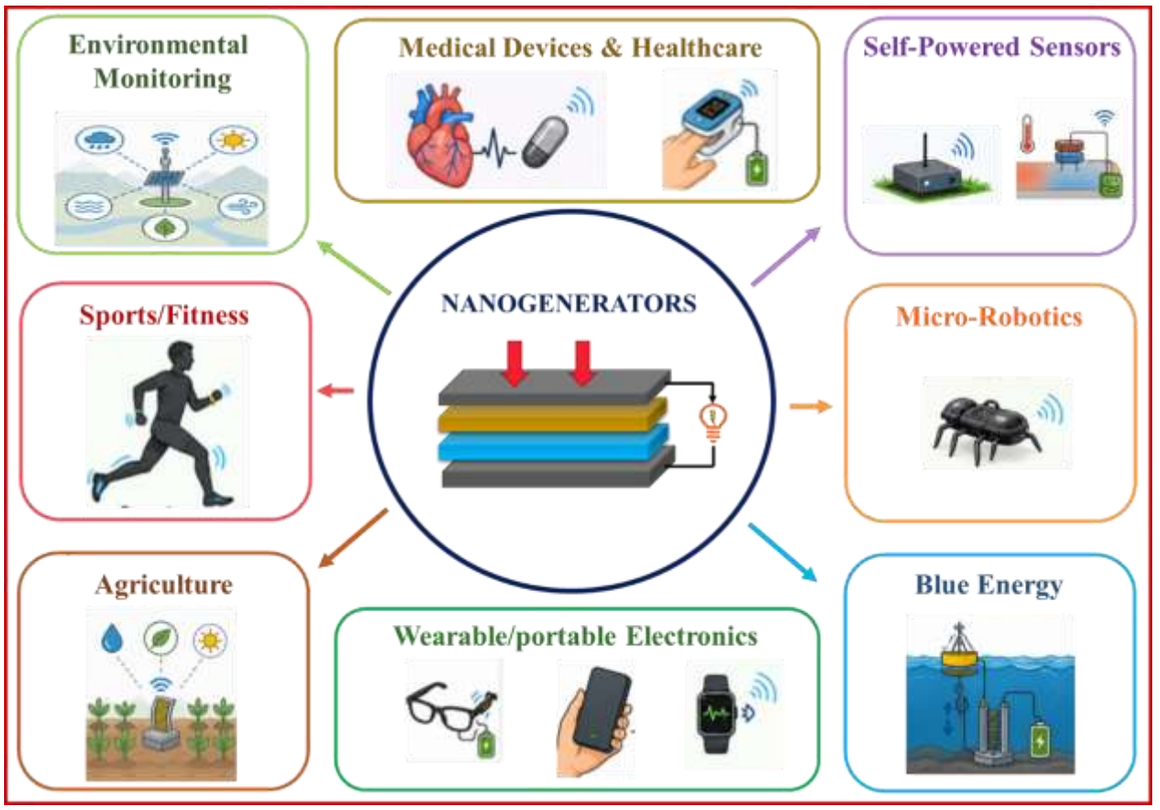

flexible energy harvesting applications.

Figure 1.2 Various applications of Nanogenerators

1.2.1 Piezoelectric Nanogenerators (PENG)

The Piezoelectric Nanogenerator provide a direct pathway for converting mechanical energy into electrical power. The underlying principle of these devices relies on the piezoelectric effect. The piezoelectric effect describes that the application of mechanical stress on a piezoelectric material induces an internal potential difference [21,32]. This generated potential gradient leads to the free charge carrier's movement between the parallel metallic electrodes that are deposited on the material's opposing surfaces. The materials that show piezoelectric phenomenon are known as piezoelectric materials [33]. This phenomenon was initially discovered in naturally occurring crystals like quartz, topaz and Rochelle salt etc. by Pierre and Jacques Curie in 1880 [34]. The fundamental prerequisite for a material to exhibit piezoelectricity is a non-centrosymmetric crystal

structure [35]. In a standard symmetric crystal, the spatial distribution of ions is perfectly balanced. The effective centre of the positive charges (cations) perfectly overlaps with the centre of the negative charges (anions). Consequently, the net electric dipole moment of the unit cell is zero. However, in non-centrosymmetric materials, this equilibrium is highly susceptible to external mechanical forces. When compressive or tensile stress is applied to the crystal lattice, structural deformation occurs. This deformation forces a spatial divergence between the positive and negative charge centres. The separation of these charge centres generates microscopic electric dipoles. The accumulation of these aligned dipoles across the bulk material results in a net electrical polarization, establishing a potential difference (piezo-potential) at the material's surface boundaries. To drive electrons through an external circuit, metal electrodes are deposited on opposing surfaces of the material [21]. A schematic representation of the mechanism involved in PENG is shown in Figure 1.3.

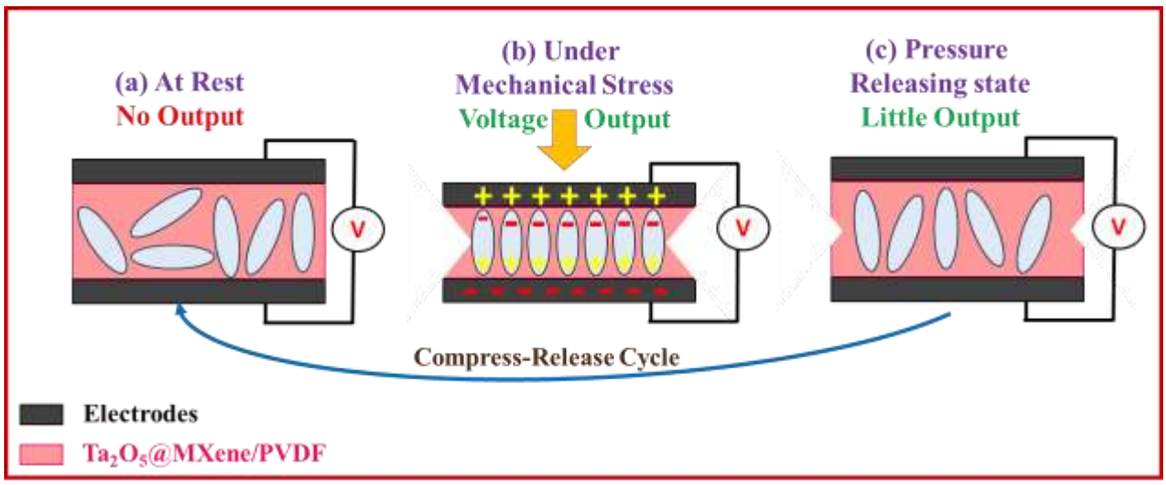

Figure 1.3 Schematic diagram for the working mechanism of PENG

The generation of piezoelectric charges is mathematically described by coupled constitutive equations that relate the mechanical and electrical tensors of the material. In its fundamental linear form, the resulting polarization (P_i) is directly proportional to the applied mechanical stress (T_j), represented in equation 1.1.

$$P_i = d_{ij}T_j \tag{1.1}$$

Where, d_{ij} represents the piezoelectric charge coefficient which serves as the primary figure of merit for the material's energy conversion efficiency. The indices i and j denote the electrical and mechanical directional axes, respectively. Based on this directional dependency, PENGs are typically designed to operate in one of two primary modes [36], described below.

- **d_{33} Mode:** In this configuration, the mechanical compressive force is applied in the exact same direction as the material's polarization axis. This mode generally yields the highest output voltage and is commonly utilized in vertical impact or footstep harvesters. The generated piezoelectric charge and the corresponding piezoelectric potential for the open circuit are obtained using equation 1.2 and 1.3, respectively.

$$Q = A\sigma d_{33} \tag{1.2}$$

$$V = t\sigma g_{33} \tag{1.3}$$

Where, σ is the stress in the same direction of applied force, A and t are the cross-sectional area and thickness of piezoelectric material respectively, d_{33} is the piezoelectric charge coefficient, g_{33} is the piezoelectric voltage coefficient.

- **The d_{31} Mode:** In this mode, the mechanical stress is applied perpendicularly to the axis of polarization. This mode is highly effective for harvesting energy from lateral bending, stretching, or cantilever vibrations. For this, the generated piezoelectric charge and the piezoelectric potential for the open circuit can be calculated through equation 1.4 and 1.5, respectively.

$$Q = A\sigma d_{31} \tag{1.4}$$

$$V = t\sigma g_{31} \tag{1.5}$$

Moreover, it is important to enhance the output performance of the PENG to make them applicable in the real practical applications. This performance boost is typically realized through a combination of structural modifications and sophisticated fabrication processes such as hot pressing, electrospinning, poling (applying strong electric field) and 3D printing [37]. Such techniques allow for the fine tuning of the material's internal dipole alignment and surface morphology, which in turn significantly amplifies the resulting power output. By optimizing these

parameters, the practical utility of piezoelectric nanogenerators is greatly extended, facilitating their deployment in self-powered sensors and smart wearable technologies.

1.2.2 Triboelectric Nanogenerator (TENG)

While the piezoelectric effect relies on internal crystal deformation, the Triboelectric Nanogenerator (TENG) operates on different physical principles. It is the synergistic combination of contact electrification (triboelectrification) and electrostatic induction. First pioneered by Professor Zhong Lin Wang's research group in 2012, the TENG transforms the ubiquitous and historically problematic phenomenon of static electricity into a highly efficient mechanism for micro-scale energy harvesting [23]. The macroscopic occurrence of the triboelectric effect has been recognized for centuries, most commonly observed when brushing dry hair with a plastic comb or rubbing glass with fur. However, translating this everyday occurrence into a reliable, nanoscale power source required a profound understanding of interfacial surface physics and advanced materials engineering. Today, TENGs are known for their exceptional capability to generate high output voltages at low frequencies and their lightweight architecture. Additionally, their unparalleled versatility in harvesting diverse mechanical energies, ranging from tidal waves to subtle biomechanical movements makes them applicable in different applications such as, self-powered sensors [27,28,31], wearable electronics [38–40], Artificial Intelligence [30,32,41], biomedical devices [9,29,42] etc. To understand the charge generation mechanism in a TENG, examination of the interface of the materials at the atomic level is important. Every material possesses a unique electron affinity. When two distinct solid surfaces are physically separated by a macroscopic distance, their respective electrons remain tightly bound to their parent atoms [43]. However, when an external mechanical force presses these materials together, the intermolecular distance decreases consequently. Once the separation distance reaches the atomic bonding length, the electron clouds enveloping the surface atoms physically intersect. This quantum mechanical overlap significantly lowers the potential barrier between the atoms, prompting electrons to migrate from the material with lower electron affinity to the material with higher electron affinity. Upon separation, this transferred charge is retained on the surfaces, resulting in a net positive charge on one material and a net negative charge on the other.

The contact electrification is fundamentally an interfacial phenomenon, the electrical output of a TENG is heavily dictated by the strategic pairing of its constituent materials. Materials are

empirically ranked according to their tendency to gain or lose electrons in a hierarchy known as the triboelectric series [44]. To maximize the potential difference, a TENG is typically constructed by pairing a highly tribo-positive material (one that readily donates electrons) with a highly tribo-negative material (one that readily accepts electrons). In the pursuit of flexible, wearable energy harvesters, engineered polymers have become the materials of choice. For instance, Nylon is frequently utilized as a robust tribo-positive layer. Conversely, fluorinated polymers such as Polytetrafluoroethylene (PTFE) and Polyvinylidene fluoride (PVDF) occupy the extreme negative end of the series. In this thesis, the tribo-negative properties of PVDF are further amplified through the incorporation of nanofillers, fundamentally altering the surface charge density.

Depending on the mechanical source and the desired electrode configuration, TENGs can be engineered into four fundamental operational modes [21,44], as described below and represented in Figure 1.4.

- **Vertical Contact-Separation mode:** In this mode, two dissimilar dielectric materials are placed facing each other with metal electrodes deposited on their back surfaces. An external force brings the surfaces into physical contact vertically, generating surface charges through triboelectrification.
- **Lateral Sliding mode:** this is similar to the contact-separation mode, it uses two dielectric layers with back electrodes, but the mechanical force is applied horizontally.
- **Single-Electrode mode:** This mode consists of only one dielectric layer and one metallic electrode. In this case, the conductive material making contact also serves as the electrode. When a freely moving object contacts and then separates from the dielectric layer, it induces a charge transfer between the single electrode and the ground.
- **Freestanding Triboelectric-Layer mode:** This mode features a pair of symmetric electrodes placed beneath a dielectric layer, while a freestanding layer moves between or above them.

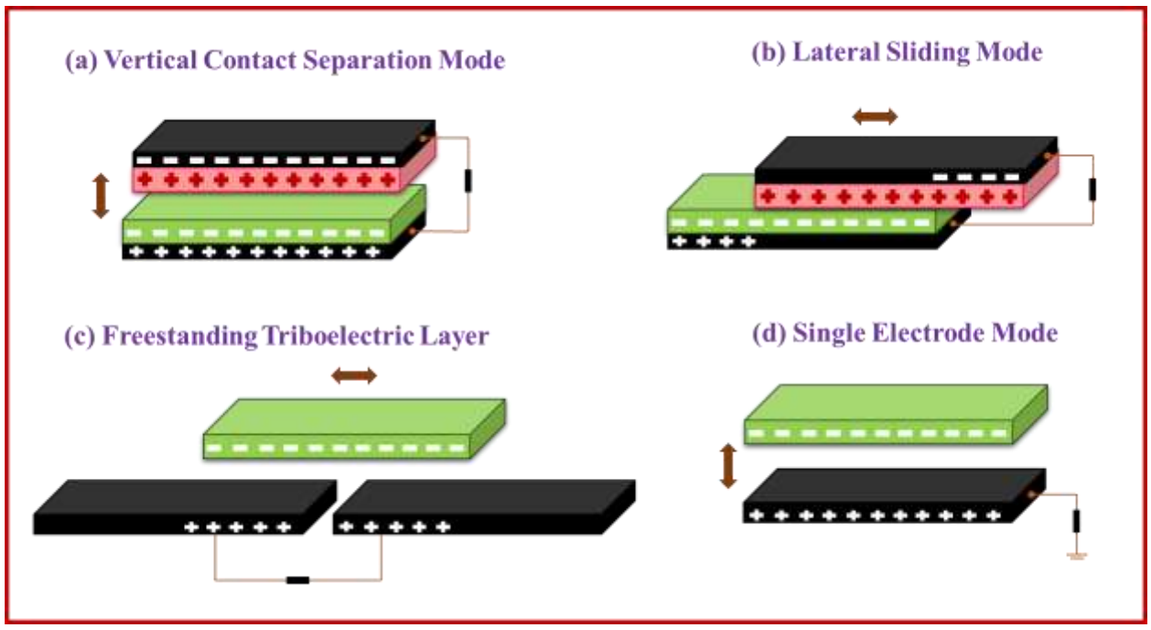

Figure 1.4 The fundamental operational modes of TENG includes: (a) vertical contact separation mode, (b) lateral sliding mode, (c) freestanding triboelectric layer and (D) single electrode mode

The Vertical Contact-Separation mode has been selected as the primary mode configuration for the research presented in this thesis. The step-by-step cycle of Vertical Contact-Separation mode has been described and shown in Figure 1.5. In the initial state (prior to mechanical stimulation), the surfaces are neutral, and no potential difference exists (Figure (a)). A dynamic shaker is used to compresses the layers. The overlapping electron clouds cause electrons to migrate from the triboelectric layer 1 (T1) to the triboelectric layer 2 (T2) (Figure (b)). As the mechanical force is released and the layers separate, a strong dipole moment is established. Because the polymer matrices are highly insulating, the charges cannot easily neutralize across the air gap. Instead, an electrical potential difference is induced across the corresponding metal electrodes, driving free electrons through the external circuit to balance the potential (Figure (c)). Once maximum separation is reached, electrostatic equilibrium is achieved, and current ceases (Figure (d)). Upon re-compression, the spatial gap closes, the induced potential diminishes, and electrons flow back through the external circuit in the opposite direction, generating an electrical signal (Figure (e)).

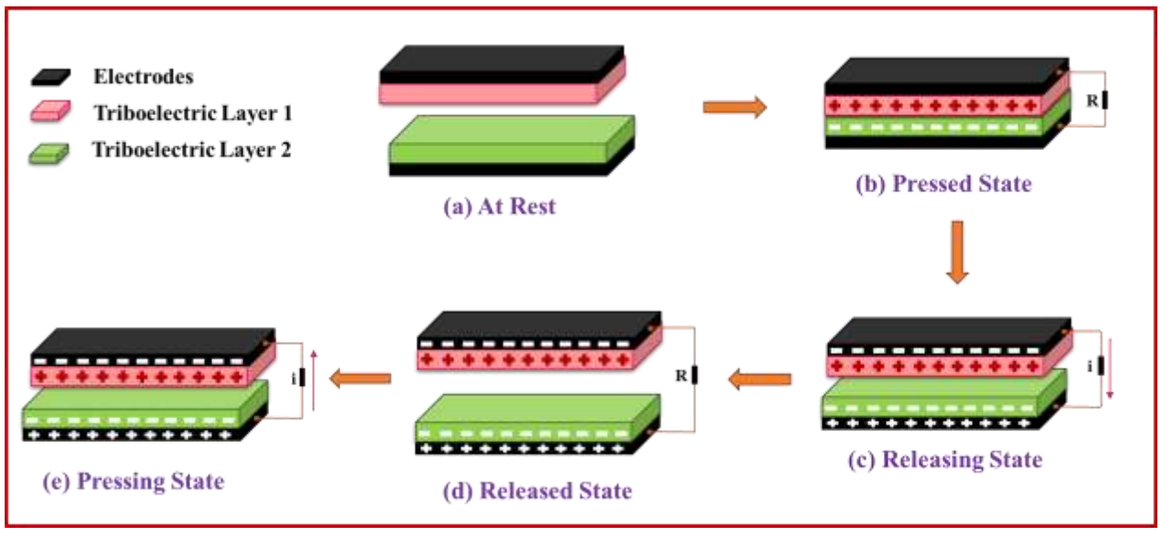

Figure 1.5 A schematic illustration of step-by-step cycle of Vertical Contact-Separation mode in TENG

The electrical behavior of a TENG operating in the contact-separation mode can be mathematically modelled by treating the system as a variable capacitor. Two dielectric materials (M1 and M2) with thickness d1 and d2 operating in contact-separation mode shown in Figure 1.6. After on contact-separation cycle there is charge accumulation on the materials' surfaces due to electrification process. The generated charge density on the surfaces of M1 and M2 has been represented by +σ and -σ, respectively. This opposite charge generation give rise to an electric potential that results in the charge transfer between the two electrodes. The potential created between these electrodes can be calculated by V-Q-x relation as represented in equation 1.6.

$$V = -\frac{Q}{C(x)} + V_{oc}(x) \tag{1.6}$$

Where V_{oc} is the open circuit voltage, Q and C(x) are the transferred charge and the dynamic capacitance between the electrodes. This fundamental equation is derived from Gauss's theorem for the electric fields within the dielectrics and the air gap between the dielectric materials. It defines the inherent capacitive relationship between the generated voltage (V), the transferred charge (Q), and the separation distance (x).

This equation highlights that the current generated by a TENG is a product of two distinct phenomena. One is the change in voltage across the non-contacting electrodes over time, and other is the variation in the system's capacitance resulting from the cyclic mechanical contact and

separation. Under the short circuit condition, charges moving across the electrode (Q_{sc}) cancel out the voltage that is generated by this triboelectric charge completely. Then the relation between V_{oc}, Q_{sc} and C modifies as

$$Q_{sc}(x) = CV_{oc}(x) \tag{1.8}$$

By optimizing these parameters specifically by increasing the surface charge density (σ) through nanocomposite engineering, power density of the TENGs can be enhanced.

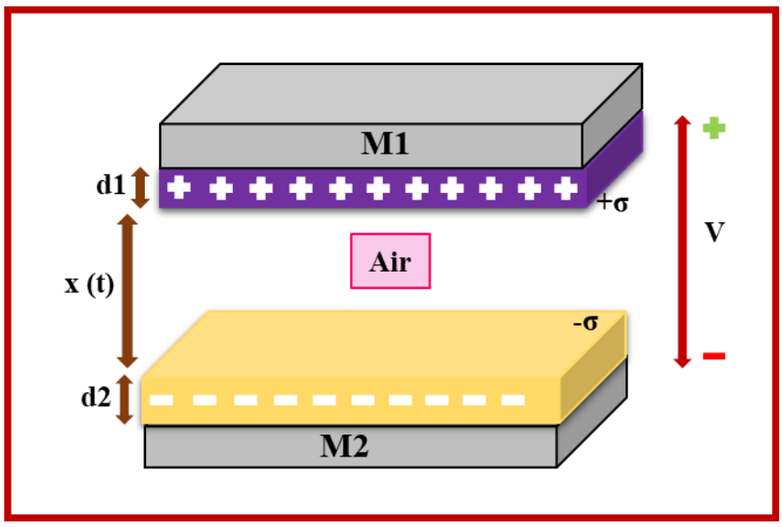

Figure 1.6 A schematic diagram depicting the separation of the two interacting materials subsequent to the creation of equally opposing charge densities (σ) on their respective surfaces

1.3 Self-Charging Piezo-Capacitor (SCPC)

The piezoelectric and triboelectric nanogenerators significantly enhances the total electromechanical power output. However, ambient mechanical vibrations such as human footsteps, irregular wind gusts, or structural oscillations etc. are inherently irregular, instantaneous, intermittent, and of low-frequency. Consequently, the electrical output generated by PENGs and TENGs have highly irregular voltage peaks and fluctuating frequencies [45,46]. Modern microelectronics, wireless sensor networks, and IoT devices cannot be driven directly by this fluctuating voltage. They require a stable, continuous, and regulated power supply to function reliably. Therefore, the mere harvesting of ambient energy is insufficient. There is a gap between instantaneous mechanical energy harvesting and continuous device operation. Therefore, it is necessary to integrate an intermediate energy storage and management system or to develop a device that can generate and store the energy at the same time.

The seamless integration of a flexible nanogenerator and an energy storage unit culminates in the realization of a self-charging piezo-supercapacitor (SCPC) [46,47]. By continuously converting wasted mechanical energy and capturing that energy in a storage unit, an SCPC can operate entirely autonomously. It effectively eliminates the reliance on external power grids and traditional electrochemical batteries. Hence, providing a sustainable and infinite-lifespan power solution for the next generation of decentralized smart electronics.

1.4 Polymers for Energy Applications

The architectural foundation of any high-performance nanogenerator is intrinsically tied to the mechanical and electrical properties of its constituent materials. For decades, the domain of mechanical to electrical energy conversion was monopolized by inorganic piezoceramics, for example Lead Zirconate Titanate (PZT) and Barium Titanate ($BaTiO_3$) etc. [20,34]. While these ceramics exhibit remarkably high intrinsic piezoelectric coefficients, their application in the energy harvesting is severely restricted by their mechanical rigidity and inherent brittleness. When subjected to the continuous, repetitive mechanical stress from ambient vibrations or human motion, rigid ceramics are highly susceptible to micro-fracture propagation and catastrophic fatigue failure [43]. Consequently, the scientific focus has definitively shifted toward the development of flexible and electroactive polymers. Polymers which possess the unique ability to absorb mechanical shocks, conform to irregular surfaces, and sustain millions of deformation cycles without structural degradation. Additionally, in 1960s, a discovery of piezoelectric behaviours in synthetic organic polymers such as polymethyl methacrylate (PMMA) and polyvinyl chloride (PVC) has been revealed. These early observations introduced the concept of smart polymeric materials, expanding the boundaries of current materials science research towards flexible polymer-based electronics.

A monumental breakthrough in this domain occurred in 1969 when H. Kawai demonstrated that electrically poled Polyvinylidene fluoride (PVDF) exhibited a good piezoelectric coefficient of approximately 6 to 7 pC/N [48]. This value was unprecedented, surpassing the electromechanical output of any other known polymer at that time. Subsequent investigations in the late 1970s by researchers such as Kepler and Anderson further elucidated the intrinsic ferroelectric and pyroelectric properties of PVDF, establishing it as a highly versatile material for nanogenerator [49]. Numerous other electroactive polymers have been also explored since

including polyamides (Nylon) [50], polytetrafluoroethylene (PTFE) [51], polyacrylonitrile (PAN) [52], and polyvinyl acetate (PVA) [53]. But PVDF and its fluorinated copolymers remain the undisputed most efficient polymer for flexible energy harvesting [54].

The dominance of PVDF in the fabrication of modern nanogenerators stems from its exceptional mechanical resilience, environmental stability, biocompatibility, and superior electroactive performance [55]. PVDF is a semi-crystalline polymer characterized by a highly adaptable molecular structure with the atoms of carbon, hydrogen and fluorine. The structural and functional characteristics of PVDF and its synergistic integration with nanofillers has been explained further subsequent sections of this chapter.

1.4.1 PVDF: Polymer for next generation flexible nanogenerators

Polyvinylidene fluoride (PVDF) is the primary polymer used for the preparation of nanogenerators in this study. PVDF is a semi-crystalline polymer synthesized through the repetitive polymerization of vinylidene difluoride (-CH_2-CF_2-) monomeric units. The spatial arrangement of these polymeric chains gives rise to a complex structural polymorphism, allowing the material to crystallize into various distinct phases (α, β, δ, Ɛ and γ) [54–56]. The energy-harvesting capabilities of the polymer are fundamentally dictated by which of these crystalline phases dominates the internal matrix. The thermodynamically most stable and naturally occurring state of PVDF is the α-phase, characterized by a trans-gauche-trans-gauche (TGTG') molecular conformation. In this structural arrangement, the inherent dipole moments of the carbon-fluorine (C-F) and carbon-hydrogen (C-H) bonds are oriented anti-parallel to one another [57]. This alternating geometry results in a complete nullification of the macroscopic dipole moment, rendering the α-phase strictly non-polar and electroactively inert. Conversely, the β-phase exhibits an all-trans (TTTT) planar zigzag conformation. This unique structural alignment forces all molecular dipoles of the individual monomers to orient in strict parallel formation on opposite sides of the carbon backbone. This alignment generates a massive permanent net dipole moment. Consequently, the β-phase possesses an exceptionally high net spontaneous polarization. It is this highly polar structural configuration that endows PVDF with its extraordinary intrinsic piezoelectric, pyroelectric, and ferroelectric properties [58,59]. These two are the commonly visible phases of PVDF and their atoms' arrangement has been depicted in Figure 1.7.

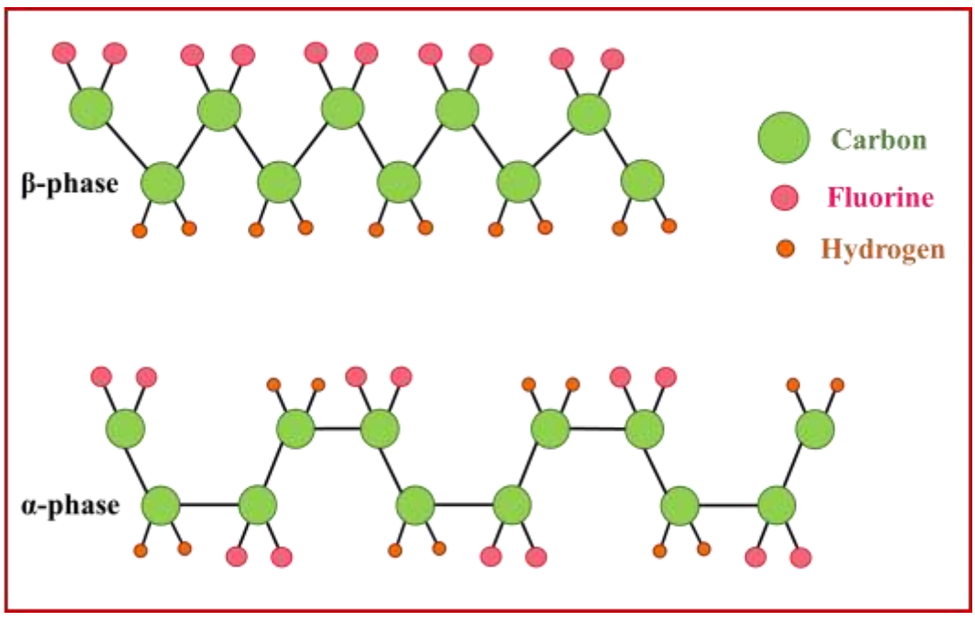

Figure 1.7 The schematic representation of orintation of β and α-phase of PVDF polymer

Beyond its internal piezoelectric capabilities, PVDF holds a premier position in the fabrication of Triboelectric Nanogenerators (TENGs) due to its unique atomic composition. The polymer chain is densely populated with fluorine atoms, which are highly electronegative [60]. This electron affinity dictates that when PVDF makes physical contact with a dissimilar material, it aggressively attracts and retains surface electrons. This innate, highly tribo-negative characteristic significantly amplifies the interfacial charge density during continuous contact-separation cycles. Therefore, this dual functionality of PVDF helps in developing the efficacious flexible nanogenerators. When utilized in an integrated device, PVDF simultaneously generates internal voltage via piezoelectric strain and drives massive external charge transfer via contact electrification. Despite its innumerable advantages, the intrinsic piezoelectric coefficient of pristine PVDF remains lower than that of its ceramic counterparts. To bridge this performance gap without sacrificing flexibility, contemporary research has been going on to develop strategies that can enhance the piezoelectric coefficient, thus energy harvesting performance of PVDF based nanogenerators.

1.4.1.1 Strategies for Enhancing the Electroactive Performance of PVDF

To fully exploit the energy-harvesting potential of a PVDF-based nanogenerator, it is imperative to maximize the electroactive β-phase of PVDF. To achieve this goal, several advanced physical and chemical strategies are actively employed in contemporary research. Historically, the phase transition from the non-polar α-phase to the polar β-phase has been driven through rigorous post-

processing techniques. Such as, uniaxial or biaxial mechanical stretching at elevated temperatures, coupled with high-voltage electric field poling, are traditional methods utilized to forcibly rearrange the TGTG' chains and permanently align the molecular dipoles [61–63]. Researchers worldwide have also worked on the other post processing strategies such as surface functionalization (addition of polar functional groups), surface modification engineering (SME) to increase the roughness of the film and organic and inorganic coating processes [64,65]. While these strategies are effective to enhance β-phase of PVDF, it often introduces manufacturing complexities and structural instabilities over time. And some of them like as, SME or coating techniques are limited to superficial improvements only.

On the other hand, there are some strategies that work in the pre or during the processing stage. Such as, recently morphological modifications through electrospinning have gained prominence [66]. The high shear forces and localized electric fields inherent to the electrospinning process simultaneously stretch the polymer jets and align the β-phase crystals during the processing. Furthermore, electrospinning generates a network of nanofibers, which exponentially increases the active surface-area-to-volume ratio. This enhanced surface roughness drastically improves the contact area available for triboelectric charge generation, making it a highly effective fabrication technique for energy devices [39,67]. Another technique is copolymerization where a slightly bulkier monomer into the PVDF chain has been added during synthesis, creating copolymers for example, P(VDF-TrFE) (Polyvinylidene fluoride-co-trifluoroethylene) [62,68]. The extra fluorine atoms in the TrFE units create steric hindrance along the carbon chains. It restricts the formation of α-phase and force PVDF chains to crystallize directly into the β-phase without any stretching required. Other pre-processing techniques like as, rapid cooling, low-temperature solvent evaporation etc. are also useful [69–71]. Furthermore, a sophisticated and highly reliable strategy in pre- processing stage is the synthesis of PVDF-based nanocomposites via the dispersion of efficient nanofillers [56,72,73]. The incorporation of inorganic nanostructures disrupts the ordered crystal structure of PVDF that promotes the crystalline electroactive β-phase. These fillers act as highly active nucleation sites, thermodynamically lowering the energy barrier for the localized growth of the electroactive β-phase.

Hence, the strategic incorporation of nanofillers into the PVDF matrix has been selected as the primary methodology for β-phase enhancement of the polymer. The high-surface-area nanofillers

not only serve as exceptional β-phase nucleating agents but also introduce their own intrinsic piezoelectric and dielectric characteristics to the composite. The addition of the optimized combinations of the specific nanofillers profoundly enhances the dielectric constant and electron affinity of the film, resulting in superior charge transfer dynamics. By synthesizing these advanced PVDF-nanocomposite films, this research fundamentally investigates the synergistic amplification of both internal piezoelectric polarization and external triboelectric surface charge, culminating in the design of robust, next-generation mechanical energy harvesting nanogenerators.

1.5 Materials for Nanofillers

The operational efficiency of PVDF-based nanogenerators can be amplified through the strategic incorporation of diverse piezoelectric, conductive, and insulating nanofillers at optimized concentrations. These nanofillers induce critical modifications at both the molecular and structural levels, thereby facilitating superior charge generation. A broad spectrum of materials including ceramics, perovskites, metal oxides, and 2D nanostructures etc. have been leveraged as functional fillers to enhance the performance of PVDF based nanogenerators [74,75]. However, the inorganic and ceramics materials such as TiO_2 [76], SnO_2 [77], $BaTiO_3$ [78,79], lead zirconate titanate (PZT) [80], etc. with high dielectric constant help in the enhancement of the dielectric properties of PVDF. These fillers interact synergistically with the PVDF matrix to promote dipole alignment and boost electrical output.

However, practical implementation of some of these materials faces significant drawbacks. For instance, the lead content in PZT raises pervasive environmental concerns, while lead-free alternatives like $BaTiO_3$ exhibit an inherent brittleness and high internal electric field gradient that restricts their utility in flexible or wearable electronics. Their independent use compromises with the desired dielectric loss, deteriorates breakdown strength, flexibility and crystallinity of the PVDF. Additionally, the integration of nanofillers requires high weight-fraction loadings creating inhomogeneity and agglomeration of nanofillers in the polymer that critically degrade the mechanical flexibility of the polymer film. On the other hand, the conducting nanofillers for example carbon nanotubes, graphene, MXene etc. can easily enhance dielectric constant and conductivity at small concentrations. However, at the same time they also increase the dielectric losses and degrade energy storage density due to the formation of conductive pathways within the polymer matrix [81–83].

To address these limitations, a nanocomposite filler with the optimized combination of inorganic and conducting fillers proves to be an efficient approach to enhance the dielectric response, nanogenerator performance, flexibility, and energy storage density of the PVDF based device, simultaneously [73,84–86]. Like as, H.Q. Wang et al. designed a polymer dielectric nanocomposite with significantly improved energy storage density by using a MoS_2@MXene core-shell heterostructure as a hybrid filler in a PVDF matrix [73]. They reported strong interfacial polarization induced by MXene and MoS_2 layer enhanced the breakdown strength of the film and reduced dielectric loss by hindering direct MXene-MXene contact, which suppressed leakage current. Similarly, Lu Yang et al. constructed PVDF based flexible force sensor with MXene@MnO_2 heterostructure reinforcement [86]. They demonstrated that the synergistic effect of microarrays patterning and MXene@MnO_2 nano-reinforcements boosted the piezo-activity of PVDF efficiently. They also reported MXene@MnO_2 incorporation strengthened the Young's modulus of the PVDF film upto 2.6 GPa. Therefore, the precise selection of nanofillers comprising different structural and moderate dielectric configurations of composites, with their optimized loading, and variating the surface chemistry of filler, considerably upgrades the output performance of the self-sustained energy device.

In this thesis, metal oxide specifically tantalum pentoxide (Ta_2O_5) has been selected as the primary nanofillers to optimize nanogenerator performance. The integration of Ta_2O_5 into the PVDF matrix elevates its dielectric constant due to high polarizability of Ta_2O_5 and interfacial polarization that streamlines charge transfer between the interfaces. Moreover, a combination of conducting nanofiller, 2D MXene nanosheets along with Ta_2O_5 have also been used as a nanofiller. As MXene can provides effective charge-trapping sites and conductive pathways. Hence, these nanofillers amplifies the polarization efficiency and generate a higher density of dipoles. Such attributes render these nanomaterials a pivotal choice in flexible, sustainable, and high-efficiency energy harvesting PENGs and TENGs.

1.5.1 Tantalum Pentoxide (Ta_2O_5)

Tantalum Pentoxide (Ta_2O_5) is a dielectric ceramic with good permittivity that has gained significant attention in the forefront of materials science due to its versatile physical and chemical profile. Naturally occurring as a white, high-melting-point powder, Ta_2O_5 is characterized by its non-toxic nature and exceptional chemical inertness, making it a sustainable alternative to lead-

based piezo-ceramics [87]. The crystallographic phases of Ta_2O_5 can be divided into two groups: low-temperature phase (β-Ta_2O_5 (600-1360 ºC)) and the high-temperature phase (α-Ta_2O_5 (above 1360 ºC)). Its high polarizability and substantial dielectric constant (~ 25) originate from the strong ionic character of the Ta-O bonds. Additionally, a wide electronic bandgap of approximately 3.5-4.4 eV endows the material with excellent electrical insulation and high breakdown strength [88,89]. These inherent attributes combined with its excellent thermal stability position Ta_2O_5 as a pivotal candidate for advanced energy storage and microelectronic applications [90–92]. When incorporated as a nanofiller within the polyvinylidene fluoride (PVDF) matrix, Ta_2O_5 can functions as more than just a passive additive. It can act as a nucleating agent that fundamentally reconfigures the PVDF's internal structure. The surface of Ta_2O_5 nanoparticles is rich in oxygen atoms which may engage in hydrogen bonding with the electron-deficient hydrogen atoms (CH_2 groups) of the PVDF chains. This interaction is expected to catalyze the transition from the coiled TGTG' (α-phase) to the all-trans TTTT (β-phase) conformation, which is the foundational requirement for high piezoelectric sensitivity. The dielectric contrast between the Ta_2O_5 fillers and the PVDF matrix can trigger the Maxwell-Wagner-Sillars (MWS) effect as well. That can lead to the accumulation of space charges at the filler-polymer interface, significantly augmenting the overall dielectric permittivity and enhance the charge-trapping capabilities of the composite.

Unlike heavier or more brittle ceramic fillers, Ta_2O_5 can be synthesized into various morphologies (such as nanoparticles or nanorods) that ensure a uniform dispersion. That streamlines the mechanical stress transfer within the film, preventing the inherent brittleness often associated with high-filler loading. The high dielectric constant of Ta_2O_5 significantly can elevate the energy storage capabilities of PVDF, allowing the nanocomposite to store a higher density of electrical energy within the same physical volume. This enhanced charge-trapping capability is further supported by its wide bandgap of Ta_2O_5, which acts as a robust insulation barrier, effectively suppressing leakage currents and preventing premature dielectric breakdown under high-frequency mechanical strain. Ultimately, the inclusion of Ta_2O_5 can optimize the electroactive phase content while simultaneously providing the charge reservoirs necessary for high-performance energy harvesting. This makes the Ta_2O_5@PVDF nanocomposite a prominent choice to test the ability for the energy harvesting performance. Moreover, the integration of Ta_2O_5 may transforms the capacitive nature of the PVDF matrix. Thus, making it a critical component for self-charging

piezo-supercapacitors (SCPC). Consequently, Ta_2O_5@PVDF nanocomposites can surpass the traditional materials by offering a pivotal solution for long-term power stability in remote IoT nodes and wearable electronics, where a constant energy supply is mandatory.

1.5.2 MXene

Recently, MXenes, a family of two-dimensional (2D) transitional metal carbides, nitrides, and carbonitrides have emerged as excellent candidates for the nanofillers due to their high electrical conductivity, robust electron-accepting nature, and large surface area making them ideal for charge density and interfacial polarization effects. The general molecular formula for MXenes is $M_{n+1}X_nT_x$. Where M is the transition metal, X is the carbon or nitrogen, nitrogen or carbonitrides, and T is the surface terminations [93,94]. In our research work, we have used Titanium Carbide MXene ($Ti_3C_2T_x$) as the nanofiller. $Ti_3C_2T_x$ is derived from the selective etching of the aluminium layer from its bulk MAX phase (Ti_3AlC_2), resulting in a distinctly layered morphology that can be further exfoliated into ultra-thin nanosheets [95,96]. The 'T_x' in its chemical formula represents surface terminations, specifically hydroxyl (-OH), oxygen (-O), and fluorine (-F) functional groups. These terminations render the nanosheets highly hydrophilic and chemically active, endowing them with a massive specific surface area and excellent charge-carrier mobility [93]. Unlike traditional ceramic fillers that rely on localized electric fields, MXene operates via direct molecular-level coupling. The electronegative functional groups (-F, -OH, -O) on the $Ti_3C_2T_x$ surface form strong hydrogen bonds and dipole-dipole interactions with the electropositive CH_2 dipoles of the PVDF chains [82,83]. This strong interfacial interaction heavily restricts the relaxation of the polymer chains during crystallization, effectively pinning them into the highly extended, all-trans (TTTT) conformation. Consequently, MXene acts as a highly potent nucleating agent, significantly accelerating the α-to-β phase transformation and maximizing the electroactive content of the composite.

Another phenomenon is the microcapacitor effect. As $Ti_3C_2T_x$ is highly conductive while PVDF is an insulator, dispersing these 2D nanosheets throughout the polymer creates a vast network of microcapacitors where two conductive MXene sheets act as electrodes separated by a thin layer of insulating PVDF chains. Such as, Trilochan Bhatta et al. synthesized PVDF/MXene composite nanofibers via electrospinning at varying concentration of MXene. They reported addition of MXene enhanced the composite's dielectric constant upto 270% and improved the triboelectric

voltage output by 1.5 times. This improvement in the PVDF/MXene composite has been driven by the formation of microscopic dipoles due to electrostatic attraction between the functional groups on the MXene surface and the hydrogen/fluorine atoms in the PVDF chain along with the creation of a micro-capacitor network. Further, they reported conductive MXene nanosheets create interconnected conductive pathways within the polymer matrix, allowing triboelectric charges to transfer much more quickly and efficiently that improved triboelectric performance. However, they reported increased leakage current and higher dielectric losses and reduced dielectric constant at higher concentration of the MXene (>20wt%) due to reaching its percolation limit [83]. According to percolation theory, as the filler concentration approaches the percolation threshold, this structure form continuous conductive bridge within the matrix. The material suddenly transitions from being an insulator to a conductor that leaks charge. That results in a drastic reduction in the dielectric properties of the film [82,97]. Hence, $Ti_3C_2T_x$ exponentially enhances the output voltage, short-circuit current, and overall energy conversion efficiency of PVDF-based nanogenerators till percolation threshold. However, the problem, such as high leakage current, uniform dispersion and elevated dielectric losses remain beyond the percolation limit. Additionally, their tendency to restack and the inherent complexity of their surface chemistry can sometimes limit their effectiveness [85,94].

The above-mentioned problems with the MXene as nanofiller can be resolved by selecting an optimized combination of nanofillers. For instance, L. Kou et al. demonstrate that incorporating a novel nitrogen, sulfur, and phosphorus tri-doped graphene (NSPG) and Ti_3CNT_x MXene quasi-3D heterostructure into a PVDF matrix significantly enhances the PENG's electrical output. This performance boost is attributed to the heterostructure acting as a potent nucleating agent, which promoted the electroactive β-phase crystallization of the PVDF. Moreover, the NSPG solves the inherent restacking problem of MXene sheets through a synergistic structural interaction. The identical high surface electronegativity of both nanofillers creates electrostatic repulsion that prevents flat stacking, while strong interfacial van der Waals attraction forces the NSPG sheets to bind with the MXene in a nonparallel, crosswise manner. This creates a stable quasi-3D nanoarchitecture where the NSPG provides mechanical support and physically spaces the MXene layers apart, ensuring a homogeneous distribution and maximizing the active interfacial area within the composite [98]. Similarly, forming the heterostructure of MXene and Ta_2O_5 can solve the restacking problem of MXene. Ta_2O_5 can effectively isolates the MXene sheets, as the

nanoparticles of Ta_2O_5 can enter between the MXene nanosheets that also helps in suppressing leakage and maintaining low dielectric losses.

1.6 Research Gap

(i) A critical knowledge gap still remains regarding the fundamental properties of the nanofillers that dictate energy conversion efficiency. PVDF offers exceptional flexibility, but its intrinsic piezoelectric and triboelectric outputs are insufficient for scale-up. Therefore, there is a pressing need to optimize the polymer matrix through the strategic incorporation of optimized combination of nanofillers. Understanding how these fillers modify molecular crystallization, enhance surface charge density, and influence the interfacial polarization is still lacking. Additionally, to keep the weight percentage loading minimum and the flexibility and eco-friendliness maximum is also the primary challenge.

(ii) To replace toxic, lead-based piezoceramics or brittle fillers, researchers are seeking highly efficient metal oxides. However, while Tantalum Pentoxide (Ta_2O_5) possesses a suitable dielectric constant, high structural stability, and great polarizability, its application as a nanofiller in flexible, polymer-based nanogenerators remains vastly unexplored. Investigating Ta_2O_5 within a PVDF matrix addresses a major material gap. Fully understanding how the highly polarizable nature of Ta_2O_5 affects the polymeric chains of PVDF could establish a new direction for the flexible nanogenerators.

(iii) While individual 2D materials (like MXenes) and metal oxides have been studied, the specific synergistic coupling of Ta_2O_5 nanoparticles with highly conductive MXene nanosheets is essentially unexplored in the context of mechanical energy harvesting. By preparing a novel MXene@Ta_2O_5 heterostructure provides a unique opportunity to simultaneously resolve multiple material limitations. The MXene sheets can provide a massive surface area for charge trapping, while the Ta_2O_5 acts as a polarizable core within the polymer matrix.

(iv) Despite the rapid expansion of piezoelectric and triboelectric nanogenerators (PENGs and TENGs), several fundamental constraints continue to impede their widespread commercialization and deployment in autonomous electronic systems. The most prominent challenge is the fluctuating and relatively low power density inherent to these devices. While PENGs and TENGs excel at harvesting ubiquitous mechanical energy, their electrical output is highly susceptible to

factors such as, vibration frequency, physical amplitude, and mechanical degradation. To circumvent the issue of intermittent power, there is an urgent need to transition from isolated energy harvesters to integrated Self-Charging Peizo-Supercapacitors (SCPCs). However, combining energy harvesting, power management, and energy storage into a singular operational platform introduces a severe integration challenge. Achieving a sustained power supply required by a device that can simultaneously scavenge mechanical energy and store it electrochemically within the same flexible device can bridge the gap between fluctuating generation and continuous consumption.

1.7 Thesis Problem

Based on the research gap aforementioned, this thesis aims to design, fabricate, and optimize high-performance, flexible nanogenerators and integrated self-charging piezo-supercapacitors utilizing polyvinylidene fluoride (PVDF) nanocomposites. By strategically incorporating advanced lead-free nanofillers, specifically ($Ti_3C_2T_x$ MXene) and moderate dielectric metal oxides (Ta_2O_5) along with their optimized concentrations this research seeks to fundamentally modify the PVDF's internal structure, thereby enhancing β-phase nucleation, maximizing interfacial polarization, and balancing internal electrical field gradient. The primary objective is to engineer a unified, lightweight PVDF based nanocomposite films that can utilize piezoelectric and triboelectric conversion mechanisms to efficiently harvest broad-frequency ambient mechanical energy. Along with that seamless integration of capacitive energy storage within the same device has also analysed. Ultimately, this work endeavors to overcome the limitations of intermittent energy generation, providing a robust, autonomous, and sustained power solution for the next generation wearable electronics.

1.7.1 Thesis Objectives

- To synthesize and explore structural and dielectric properties of Ta_2O_5 with varying sintering temperature
- To optimize Ta_2O_5@PVDF flexible nanocomposite films towards their mechanical and dielectric properties
- To prepare Ta_2O_5@MXene reinforced PVDF nanocomposite flexible films and study their dielectric and mechanical characteristics

- To investigate the energy harvesting performance of the synthesized flexible nanocomposite as PENG and TENG
- To prepare a potential self-charging piezo-supercapacitor for energy harvesting and storage application

1.7.2 Thesis Layout

The present thesis comprises seven chapters, and a brief summary of each chapter is presented as follows:

Chapter 1: Introduction

This chapter sets the foundation for the entire thesis by initiating with a brief introduction outlining the origin of the core energy and materials problem that the research addresses, detailing the need for high-performance, flexible dielectric systems. The primary focus is established by discussing the motivation of the research work, which centers on overcoming the intrinsic limitations of PVDF and developing hybrid nanocomposites for advanced energy applications. A comprehensive overview of the current literature is presented, covering the dielectric constraints of PVDF. The chapter ensures a strong conceptual understanding by including the fundamental concepts of PVDF's phases and the role of nanofillers. Finally, the chapter highlights the specific importance of the selected materials (PVDF, Ta_2O_5, and MXene) and outlines the precise objectives of the thesis work at the end.

Chapter 2: **Experimental Methodology – Synthesis and Characterization Techniques**

This chapter outlines various experimental methods that have been employed to synthesis and analyse the prepared samples. Among the various synthesis techniques, hydrothermal method has been used for the synthesis of Ta_2O_5 and Ta_2O_5-based heterostructures. Further, a simple solution casting method has been employed for the preparation of polymer nanocomposite films.

The structural, morphological and mechanical analysis has been done using X-ray diffraction (XRD), field emission scanning electron microscopy (FESEM), transmission electron microscopy (TEM) and universal tensile machine (UTM). The impedance spectroscopy has been used to study the dielectric properties of the synthesized materials. A brief introduction of all the characterization methods used to examine the prepared samples are presented in depth.

Chapter 3: Exploration of Structural and Dielectric Properties of Ta_2O_5 at Different Sintering Temperature

This chapter delves into the synthesis of tantalum pentoxide (Ta_2O_5) via hydrothermal method and its dielectric characteristics, with a particular focus on elucidating the influence of sintering temperature, applied field frequency (ranging from 20 Hz to 2 MHz) and operating temperature (from 80K to 400 K). The synthesised powder was calcinated at different temperature to analyse the phases of Ta_2O_5. The most stable orthorhombic phase of Ta_2O_5 has been obtained. The comprehensive characterizations of the prepared nanostructures were performed to validate their crystal structures, morphological attributes, functional groups, and their dielectric properties. XRD analysis confirms the crystal structure transformation from amorphous nature to hexagonal and orthorhombic phase on increasing the calcination temperature. Further, prepared material has been sintered at different temperatures, and their dielectric properties has been studied using impedance spectroscopy. Remarkably, Ta_2O_5 nanoparticles sintered at 950 ºC exhibited substantial dielectric constant (ε′), registering 20 and 25 at 100 Hz for room temperature and 400 K, respectively. This temperature dependent behaviour highlights their adaptability across diverse operational conditions. The sintering process increased the dielectric constant to 25 coupled with a reduction in the dielectric losses to < 0.025 within the nanostructures. The observed improvement in the dielectric properties is attributed to the thermally activated charge carriers, enhanced grain size and the effects of the orientational and interfacial polarization. This investigation affirms the potential utility of Ta_2O_5 nanostructures as a dielectric material in electronic devices for the advancement of next generation energy storage devices.

Chapter 4: Optimizing Dielectric and Mechanical Characteristics of Ta_2O_5 Reinforced PVDF Flexible Nanocomposite Films

This chapter focuses on the preparation of Ta_2O_5@PVDF nanocomposite thin films using a solution casting method with different weight % of Ta_2O_5 NPs (0.625, 1.25, 2.5 and 5 wt%) as nanofillers. The dielectric results evince that the value of ε′ increases along with concentration of filler up to 1.25 wt% (TaP2) in the thin films and for the higher concentrations, ε′ values decreases but still more than that of pure PVDF film. The ε′ of TaP2 was found to be around 7 times higher than that of pure PVDF film because of the addition of Ta_2O_5 nanofillers, magnified orientation and interfacial polarization. Besides, mechanical properties of the films divulge the enhanced

tensile strength and upgraded elasticity with the addition of Ta_2O_5 NPs. Overall, the incorporation of nanofillers (1.25 wt%) with optimized low concentrations in the PVDF based thin films helped in retaining a higher degree of crystallinity and increased dielectric constant (~ 40 at 120°C & 1 KHz), magnified tensile strength (~21 MPa) with low dissipation loss (~0.024) without affecting the molecular chain of PVDF film which is much better than the reported data of other inorganic fillers. As a result, the present study suggests that flexible Ta_2O_5@PVDF nanocomposite thin films can be an efficient material for wearable electronic devices, lithium-polymer batteries etc.

Chapter 5: Study of Ta_2O_5@MXene Reinforced PVDF Nanocomposite Films towards its Dielectric and Mechanical Properties

This chapter describes the successful development and characterization of a novel hybrid material system. This began with the synthesis of the Ta_2O_5@MXene nanofiller via a scalable hydrothermal method. Structural and compositional integrity were confirmed through rigorous analysis: XRD and XPS characterization of the filler successfully validated the formation and chemical stability of the Ta_2O_5@MXene heterostructure. These nanofillers with different concentration (0.625, 1.25, 2.5 and 5 wt%) were then homogeneously integrated into a PVDF polymer matrix through film fabrication. Systematic dielectric and mechanistic investigations have been followed, including impedance spectroscopy, which confirmed an enhancement in the nanocomposite's dielectric constant. This improved dielectric property was directly linked to the intensification of interfacial polarization, which successfully promoted the formation of the highly polar β-phase of PVDF, a prerequisite for amplified electrical output in the finished devices. Moreover, the mechanical properties of the optimized flexible Ta_2O_5@MXene/PVDF nanocomposite films were also tested.

Chapter 6: Applications of the synthesized Nanocomposite Films Towards Mechanical Energy Harvesting and Storage Devices

This chapter includes the flexible energy harvesting performance of the previously synthesised Ta_2O_5@PVDF and Ta_2O_5@MXene/PVDF nanocomposite films. The resulting Piezoelectric Nanogenerator (PENG) exhibited a remarkable performance enhancement, generating a voltage output of ~ 56 and 75 V for Ta_2O_5@PVDF and Ta_2O_5@MXene/PVDF nanocomposite based nanogenerators at the optimized concentration of the nanofillers. The highest voltage output has been observed for Ta_2O_5@MXene/PVDF-based PENG at 1.25 wt% which was 2.5 times higher than that of the pristine PVDF-based PENG device. Furthermore, the scalability of the technology was extended to Triboelectric Nanogenerator (TENG) applications, where performance was

confirmed to scale linearly with increasing device dimensions, yielding competitive power outputs. The measured power densities of ~ 125 W/cm^2 for the Ta_2O_5@MXene/PVDF-based PENG and ~ 196 W/cm^2 for the TENG across varying load resistances confirm the devices' capability to efficiently drive low-power wearable electronics. Furthermore, MXene@Ta_2O_5/PVDF has also been tested for its supercapacitor capabilities towards self-charging piezo-supercapacitor. It showed good areal capacitance of ~159 mF/g at scan rate of 5mV/s. Collectively, the Ta_2O_5@MXene/PVDF nanocomposite represents a stable and scalable material solution for the next generation of flexible and self-powered systems. Additionally, the real time applications of the fabricated devices have been displayed to check the practicality of the nanocomposite-based PENG and TENG devices.

Chapter 7: Conclusion, Future Scope & Social Impact

This chapter summarizes the key research outcomes based on the data obtained from preceding chapters of the thesis. Further, it outlines the future directions of the work, culminating in a discussion of the potential social and industrial impact of the research findings.

CHAPTER 2

Synthesis and Characterization Techniques

This chapter provides the detailed procedures for the chemical synthesis of the diverse nanostructured materials and development of flexible nanocomposite films used in this research. Further, it includes in depth review of the characterization tools along with their underlying working principles used to analyse the structural, morphological, dielectric and mechanical properties of the samples. It also describes the specialized instruments and experimental setups used for high-precision electrical measurements to validate the energy harvesting and storage performance of the fabricated devices.

2.1 Overview

A wide variety of techniques are available to prepare and modify metal oxide nanostructures, allowing precisely tailor their structural and morphological properties for specific applications. Fundamentally, these synthesis methods are categorized into two primary approaches, (i) top-down and (ii) bottom-up. Top-down approach involves breaking down macroscopic, bulk materials into nanoscale structures using mechanical, thermal, or chemical energy for example, solid-state route etc. While effective for bulk production, it can sometimes introduce impurities and structural defects. In contrast, bottom-up approach is a constructive method where atoms and molecules nucleate and self -assemble into complex nanostructures [99]. Examples include sol-gel process, chemical vapor deposition, hydrothermal method etc. this approach provides superior control over the material's purity, particle size, and morphology. Establishing a viable synthesis route is fundamental prerequisite for analysing material properties and enabling large-scale commercial production. Therefore, our research utilizes a simple, eco-friendly hydrothermal approach to synthesize the targeted metal oxide nanostructures.

2.1.1 Hydrothermal Method

The hydrothermal method is a wet-chemical process used to create nanomaterials by chemical reactions. The process is carried out in a sealed, high pressure reaction vessel known as Teflon-lined stainless-steel autoclave. Chemical precursors are dissolved or dispersed in an aqueous solvent, sealed within the autoclave, and subjected to elevated temperatures. Under these elevated temperatures and pressure conditions, the physical and chemical properties of the solvent change dramatically. A specific volume of aqueous precursors is sealed within the Teflon beaker to generate the necessary internal pressure. Additionally, maintaining an optimal fill level is critical to prevent leakage or overflow during the thermal process. By precisely controlling the reaction temperature, duration, and pressure within a high-temperature oven, a significant yield of well crystallized structures can be synthesized [100]. A schematic arrangement of the hydrothermal autoclave has been depicted in Figure 2.1 used for the synthesis.

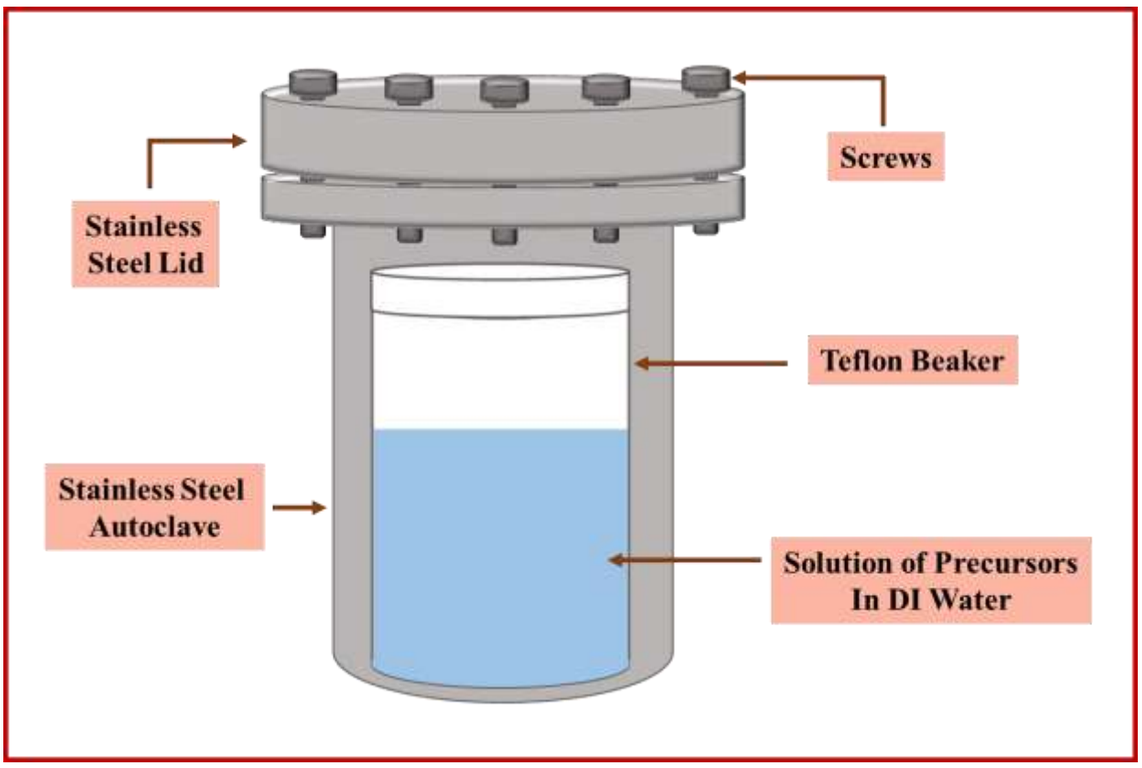

Figure 2.1 A schematic diagram of autoclave used for hydrothermal synthesis

The chemical formulation for hydrothermal synthesis consists of several functional components that work together under high pressure to grow crystals, as follows:

(i) **Reactant precursors:** These are the primary reactants that involves in chemical reaction within solvents to form desired nanomaterials. They provide the metal atoms that will eventually form the crystal lattice.

(ii) **Mineralizers:** these are added to the solvent to control the pH of the solution and increase the solubility of the precursors. They act as catalysts that speed up the hydrolysis process. By making the environment more acidic or basic, they help the metal ions react and nucleate.

(iii) **Structure-Directing Agents/Surfactants:** these are surface-active molecules added to control the anisotropic growth of the nanostructures. They selectively adsorb onto specific crystallographic planes, allowing for the engineering of shapes, such as nanorods, nanosheets etc.

(iv) **Supplementary additives:** There are some other additives that are used in the hydrothermal synthesis like capping agents, reducing or oxidizing agents, chelating agents, stabilizers. Theses additives are essential to control the oxidation state of the metal ions and final morphology of the desired nanostructures.

Key advantages of the hydrothermal method:

(i) This method produces comparatively highly crystalline phases and high purity metal oxides.

(ii) Hydrothermal technique provides good morphological and size control over the nanomaterials. By precisely tuning the reaction parameters, such as the processing temperature, time, solvent pH, precursor concentration etc. one can direct the crystal growth to form specific shapes.

(iii) As the reaction is contained in a sealed autoclave at relatively moderate temperatures, it prevents the escape of the toxic vapors and consumes less overall energy making it eco-friendly and energy efficient technique.

(iv) The setup for hydrothermal synthesis is simplistic in nature ensures operational ease and facilitates cyclic production of nanomaterials.

2.2 Deposition of Films

There are many deposition techniques to prepare the polymeric thin films, such as spin coating, drop casting, spray coating etc. Among which drop casting technique was used for the preparation of thin films in this research work.

2.2.1 Drop Casting Method

Drop casting is one of the most straightforward and cost-effective liquid deposition techniques used to fabricate thin films from chemically synthesized materials. In this method, a precisely measured volume of a solution containing the active material such as PVDF dissolved in a volatile solvent is dropped using a micropipette onto a stationary substrate. The film formation is governed by the subsequent evaporation of the solvent, which leaves behind a solid layer of the dissolved or dispersed material. A schematic diagram of the synthesis of thin films via drop casting technique has been shown in Figure 2.2. To achieve a high quality and uniform films, the optimization of several experimental parameters such as solvent volatility, substrate temperature etc. is important.

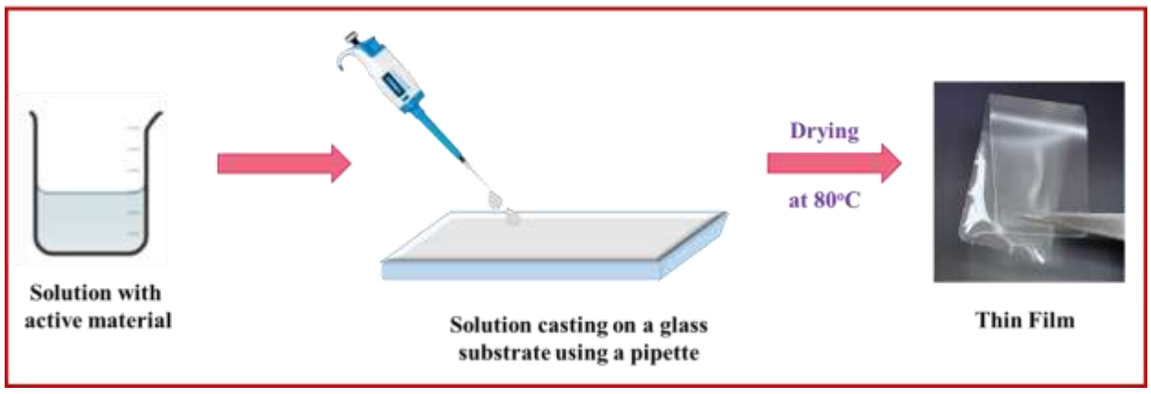

Figure 2.2 A schematic diagram showing the synthesis of thin films via drop casting technique

2.3 Characterization Techniques

To validate the successful synthesis of nanofillers and their subsequent integration into PVDF-based nanocomposite thin films, various analytical techniques has been employed. A systematic characterization strategy is essential to confirm the structural integrity of the prepared materials and to establish the relationship between their physical properties and their performance in energy harvesting applications. The structural evaluation has been done using X-ray Diffraction (XRD) to identify crystalline phases and lattice parameters. To investigate the surface topography and morphology, Field Emission Scanning Electron Microscopy (FESEM) and Transmission Electron Microscopy (TEM) are utilized. Fourier Transform Infrared Spectroscopy (FTIR) has been conducted to analyse chemical bonding and functional groups attachment. Further, Impedance Spectroscopy is used to observe the dielectric behaviour of the synthesised materials with respect to frequency and operating temperatures. Universal Tensile Machine (UTM) is utilized to perform tensile tests and to identify key mechanical parameters. The followed sections of this chapter provide a detailed explanation of the fundamental working mechanisms of the instruments used in this research work.

2.3.1 X-Ray Diffraction (XRD)

In material science ang engineering, XRD is non-destructive technique used for a wide range of evaluation such as, to identify crystalline nature and structural phases, to determine crystallite size, to measure lattice strain, to calculate degree of crystallinity, dislocation density etc. The historical development of XRD as a structural start with Wilhelm Conrod Rontgen's 1895 discovery of X-rays, which provided the foundational radiation source for atomic-scale analysis. This was further

refined by W. H. Bragg and W. L. Bragg who subsequently formulated the Bragg's law which transformed the XRD from a theoretical observation into a practical analytical method [101].

The working mechanism of a XRD instrument relies on a precisely coordinated interaction between its primary components: an X-ray tube, a sample holder, and a detector illustrated in Figure 2.3. Inside the X-ray tube, a filament is heated to produce electrons, which are then accelerated toward a metal target (usually Copper) under high voltage. The resulting collision generates a monochromatic X-ray beam that is collimated and directed toward the sample [102]. A schematic diagram of the X-Ray tube has been shown in Figure 2.4. As the instrument operates, the X-ray source and the detector move along an arc, varying the angle of incidence (θ). The operational importance of X-rays stems from their extremely short wavelengths (0.1 Å to 100 Å), which allow them to penetrate deep into the matter and interact with the electron clouds of atoms. When an X-ray beam strikes a crystalline sample, distinct patterns of X-rays is produced. In most directions, these scattered waves cancel each other out through destructive interference. However, at certain incident angles and wavelengths defined by the geometric arrangement of the atoms, the waves reinforce one another, creating high intensity radiation peaks.

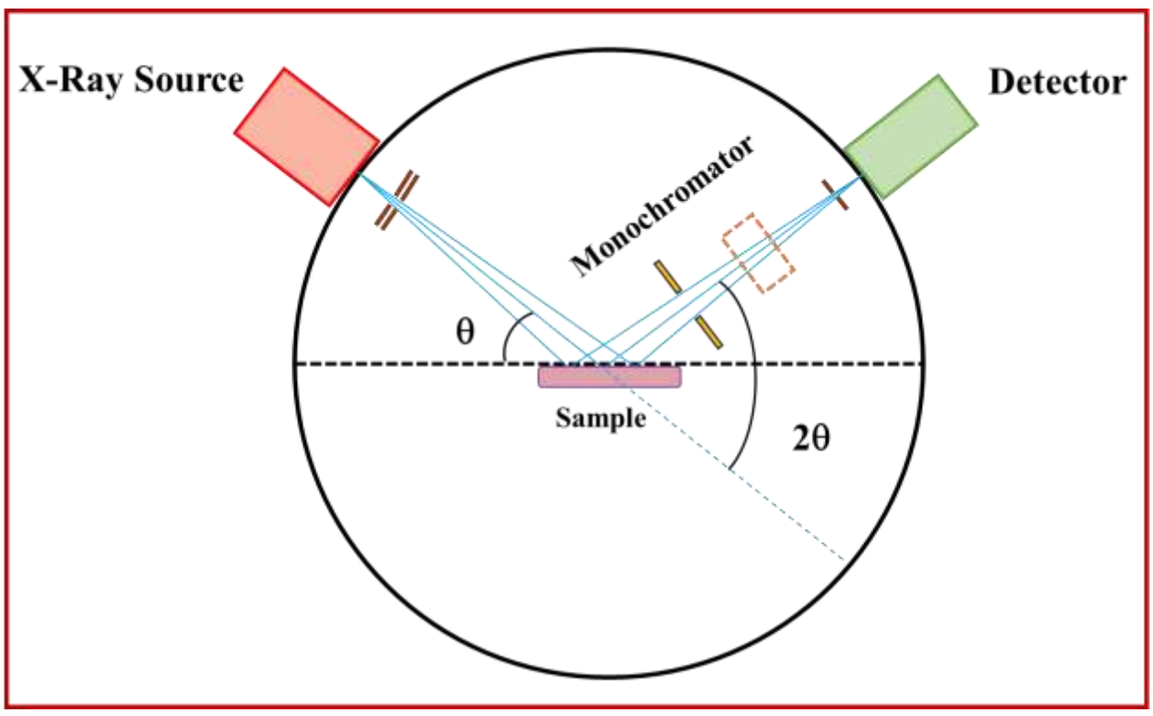

Figure 2.3 A schematic diagram representing components of XRD instrument

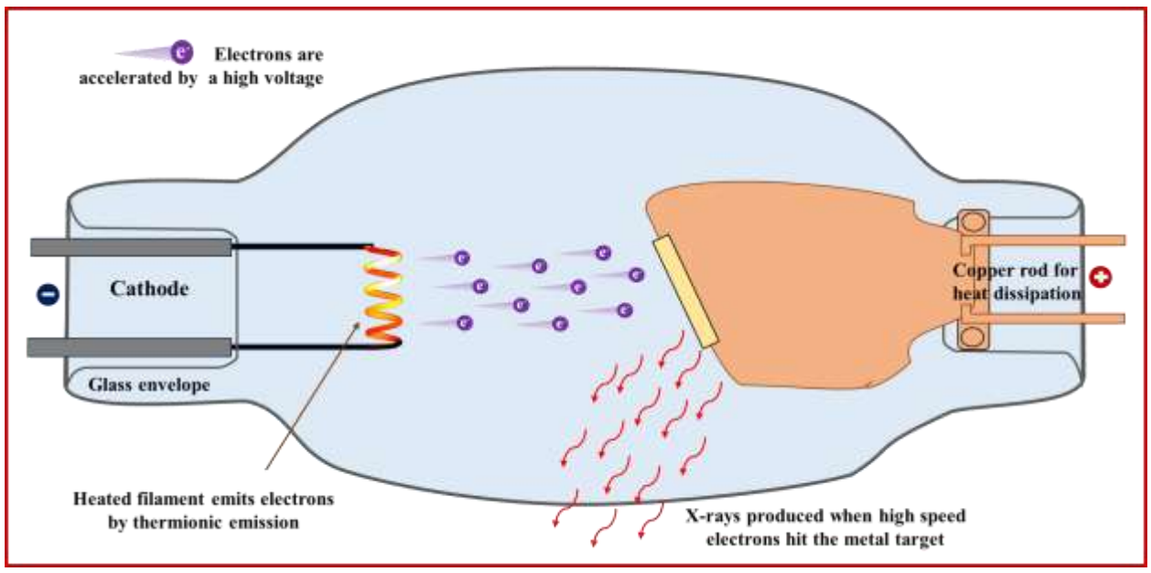

Figure 2.4 Schematic diagram showing the generation of X-rays in X-ray tube

46 According to W. L. Bragg, a crystal is viewed as a series of parallel atomic planes separated by a specific interplanar distance (d). When incident X-rays are scattered by ions within these successive layers, they undergo constructive interference that results in sharp diffraction peaks as illustrated in Figure 2.5. This phenomenon occurs only when the path difference between the waves, defined as 2dsinθ, is equal to an integer multiple of the wavelength (nλ) [103]. This fundamental relationship given by the equation 2.1, known as Bragg's law defines the crystalline diffraction domain where $\lambda \leq 2d$.

$$2dsin\theta = n\lambda \tag{2.1}$$

where n is the order of the diffraction.

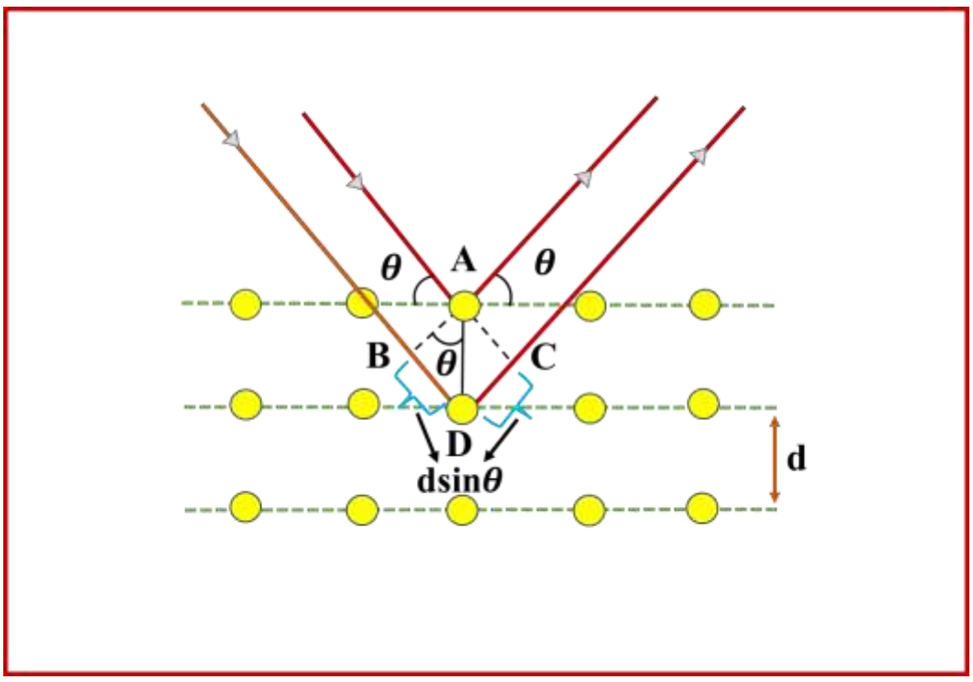

Figure 2.5 Schematic showing the diffraction of X-rays obeying Bragg's law

The positioning of these diffraction peaks is governed by the unit cell dimensions and the underlying crystal symmetry, while the peak intensities are determined by the structure factor, F_{hkl}, expressed as:

$$F_{hkl} = \Sigma f_n e^{2\pi i(hu_n kv_n lw_n)} \quad (2.2)$$

In this equation u,ν, w represents the atomic coordinates, h, k, l are the Miller indices and fn denotes the atomic scattering factor. When analyzing samples in a powdered state, the radiation interacts with all possible crystallographic planes simultaneously. Furthermore, the broadening of these peaks can be utilized to estimate the average crystallite size (D) via the Scherrer equation:

$$D = k\lambda/\beta cos\theta \quad (2.3)$$

For the structural characterization in this study, a D8 Advance Bruker X-ray diffractometer was employed, utilizing CuK_α (λ = 1.5406 Å) as the primary X-ray source. The diffraction patterns were recorded at room temperature with a meticulous step size of 0.02° and a scanning rate of 2° per minute. The resulting XRD spectra were validated by comparing them against standard JCPDS database and published literature.

2.3.2 Fourier Transform Infrared Spectroscopy (FT-IR)

FT-IR spectroscopy is a versatile and non-destructive analytic technique widely employed to identify functional groups and elucidate the molecular architecture of both organic and inorganic compounds. The fundamental utility of FT-IR lied in its ability to act as a molecular "fingerprint", where specific chemical bonds exhibit unique vibrational frequencies. The technique is based on the interaction of infrared radiation with the dipole moments of molecular bonds. When a sample is exposed to the electromagnetic spectrum specifically in mid-infrared region (400-4000 cm^{-1}), the molecules absorb energy at specific resonant frequencies that correspond to the energy differences between their vibrational ground and excited states. For absorption to occur, the vibrational motion must result in a net change in the molecule's dipole moment. These molecular vibrations generally occur in two primary modes: stretching (changes in bond length) and bending (changes in bond angle). The exact frequency at which a bond vibrates is governed by several physical parameters, including the atomic masses of the bonded elements and the strength of the chemical bonds. Consequently, complex molecules containing various functional groups (such as -OH, -NH, or -CH) produce a sophisticated spectral signature. By comparing these observed peaks with established IR databases, the chemical constituents and bonding environments of the synthesized materials can be precisely identified [104].

Modern FT-IR spectrometers offer significant advantages over traditional dispersive instruments, including superior signal-to-noise ratios, high spectral resolution, and rapid data acquisition. The core component of the instrument is the Michelson interferometer, which modulates the infrared radiation emitted from a broadband source. As demonstrated in Figure 2.6, the interferometer utilizes a beam splitter to divide the incident radiation into two separate paths. One beam reflects off a fixed mirror, while the other reflects off a moving mirror. This arrangement creates a variable path difference, or optical retardation, leading to constructive and destructive interference. The recombined beams form a complex signal known as a interferogram, which contains data for all sample, which selectively absorbs frequencies characteristic of its molecular bonds. The transmitted of reflected light is then captured by a detector.

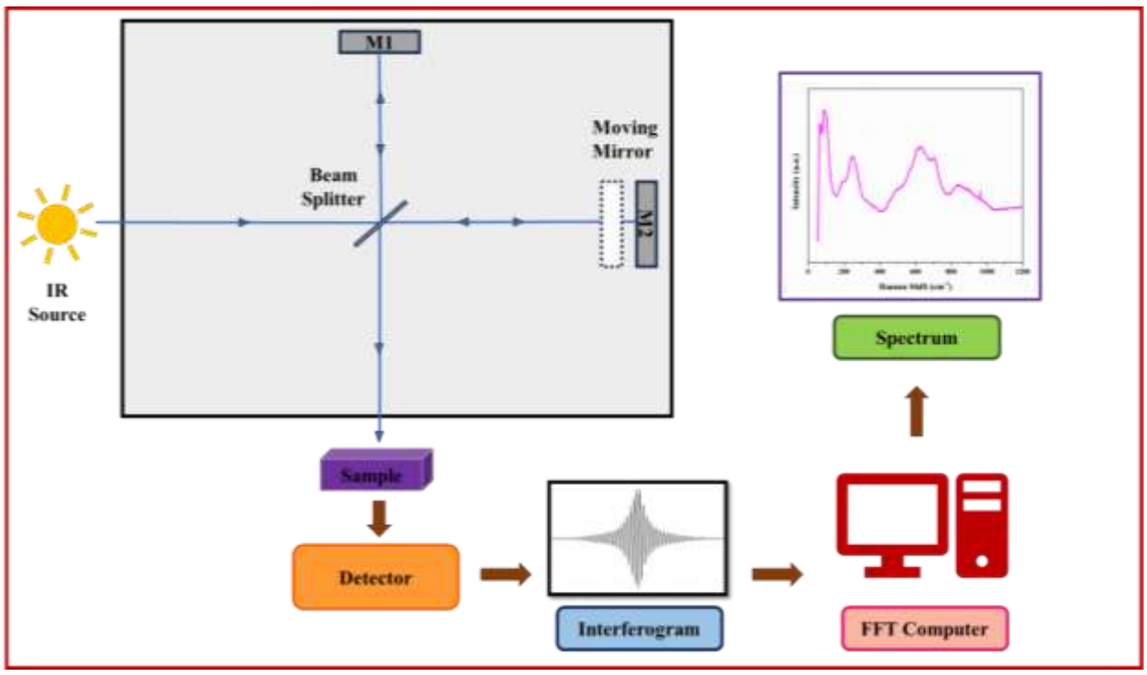

Figure 2.6 Schematic diagram representing FTIR spectroscopy

The raw interferogram data is mathematically converted into a readable spectrum using the Fourier Transform algorithm. This process translates the signal from the "time domain" into the "frequency domain" resulting in a plot typically represented as transmittance (%) or absorbance vs wavenumber (cm^{-1}). In the present study, FT-IR spectra were recorded using a PerkinElmer Fourier Transform Spectrometer. This analysis was primarily utilized to evaluate the transformation of the PVDF crystalline structure. Specifically, the characteristic peaks at 763 cm^{-1} (representing the α-phase) and 840 cm^{-1} (representing β-phase) were analyzed to determine the relative percentage of the piezoelectric phase within the various PVDF-based thin films. In the context of this research work, FT-IR is crucial for quantifying the electroactive β-phase in PVDF- based nanocomposites films as transition from the non-polar α-phase to the polar β-phase is marked by distinct changes in the infrared absorption spectra.

2.3.3 Raman Spectroscopy

Raman spectroscopy is a non-destructive analytic technique used to examine the vibrational, rotational, and additional frequency modes shown by the samples. By measuring these modes, it generates a unique structural fingerprint for the specific molecular identification of the specimen. This technique is based on a phenomenon called Raman effect, which involves the inelastic scattering of light [105]. When a sample is illuminated by a highly focused monochromatic light,

its photons interact with the specimen that results in absorption, reflection or scattering of photons. The vast majority of these photons bounce off the molecules with the same exact same energy and as the incoming laser, known as elastic scattering. This results in the emission of the Rayleigh scattered light. However, a very small fraction of the incident light scatters inelastically, resulting in a change in frequency. In Rayleigh Raman scattering, the frequencies of incident and scattered light are identical. And if the scattered light has a lower frequency than the incident laser, it produces Stokes lines, which are the primary signals analyzed in Raman spectroscopy. Conversely, if the scattered light has a higher frequency, it produces anti-Stokes lines. The resulting Raman spectrum plots the intensity of this scattered light against the energy difference, which is recorded as the Raman shift [106].

At the fundamental level, when the electric field (E) of the incoming photon interacts with a molecule, it distorts the molecule's electron cloud and induces a dipole moment (P). This relationship is expressed mathematically as:

$$P = \alpha E \tag{2.4}$$

Where α represents the polarizability of the molecule. For a specific molecular bond to be considered "Raman active" and appear on the spectrum, the vibration must cause a change in this polarizability [107].

A Raman spectrometer consists of three main components: an intense laser source to ensure a high signal-to-noise ratio, a sample illumination pathway, and a detector system. Depending on the setup, these systems typically utilize charge-coupled devices (CCD) or germanium-cooled detectors integrated with Fourier-transform infrared (FTIR) architectures. A simplified schematic of this equipment is illustrated in Figure 2.7. As an analytical tool, Raman spectroscopy offers distinct advantages over traditional IR spectroscopy as it is highly effective for characterizing inorganic compounds and can be easily used in aqueous environments. Furthermore, it requires small sample volume, making it an ideal, non-destructive method for evaluating structural additives and impurities in both liquid dispersions and solid films, enabling precise qualitative and quantitative analysis.

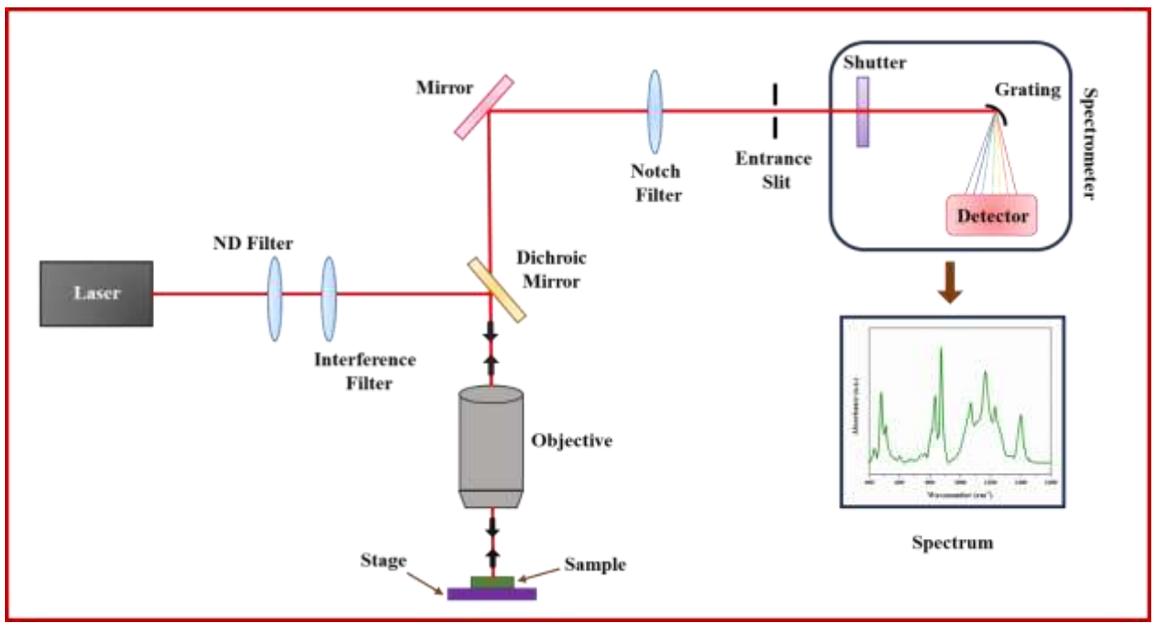

Figure 2.7 Schematic representation of Raman spectrometer

2.3.4 UV-Visible Spectroscopy

UV-Visible spectroscopy measures the attenuation of light as it passes through or reflects off a sample in the ultraviolet and visible wavelength ranges (190 nm to 800 nm). A light source emitting a broad spectrum of radiation is used. This light passes through a monochromator, which act as filter to select a single specific wavelength. The monochromatic beam is directed through a cuvette containing the sample solution. When a material is exposed to photons with energy matching or exceeding its bandgap energy, electrons are excited from the valence band to the conduction band. Then a detector measures the intensity of the light that made it through. A schematic diagram of the UV-Visible spectrometer shown in Figure 2.8. The spectrometer records the intensity of the light in two modes. One is transmittance mode where light passes through the material and another is reflectance mode where light bounces back compared to a reference beam. This recorded data is converted into an absorbance spectrum (absorbance vs wavelength). This absorbance is governed by the Beer-Lamber Law represented by equation 2.5, where A is the absorbance, ε is the molar coefficient, l is the path length and c is the concentration.

$$A = \varepsilon l c \tag{2.5}$$

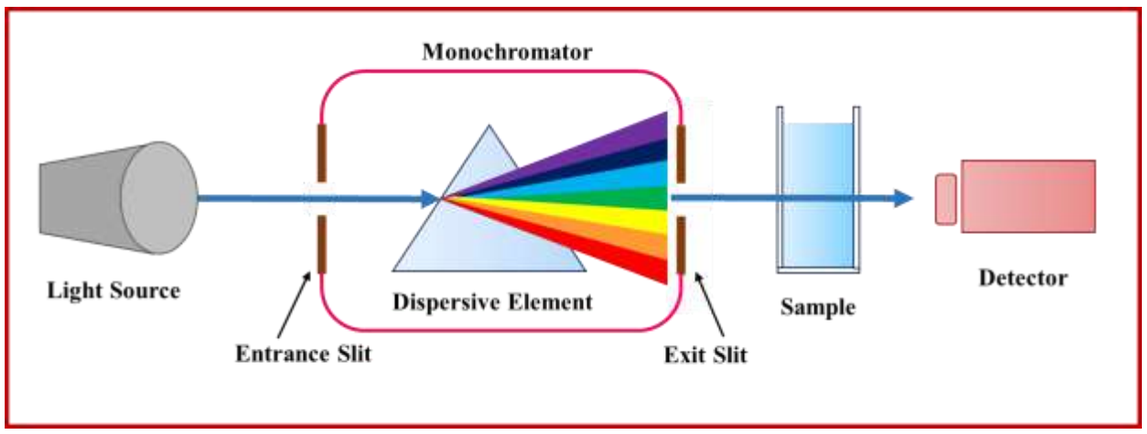

Figure 2.8 Schematic diagram illustrating UV-visible spectrometer

Further, to determine the bandgap, a Tauc plot is structured by plotting $(\alpha h\nu)^{1/n}$ on the y-axis against the photon energy ($h\nu$) on the x-axis. The linear portion of intersection gives the exact optical bandgap of the synthesized materials. If the linear portion of the graph fitted best for n = 1/2 or n = 2, then it represents the direct or indirect bandgap, respectively [108]. Hence, UV-Visible spectroscopy is important to calculate the bandgap to confirm the successful synthesis of the material and to observe any bandgap narrowing or widening caused by different treatments.

2.3.5 Scanning Electron Microscopy (SEM)

Scanning Electron Spectroscopy is a sophisticated imaging technique that utilizes a focused beam of high-energy electrons, rather than visible light, to analyze the surface characteristics of solid samples. By scanning the electron beam across the sample in a systematic raster pattern, the instrument generates high-resolution three-dimensional representations of the material's topography, morphology, and elemental composition. This method is exceptionally versatile, capable of analyzing a wide range of organic and inorganic materials from the micrometre down to the nanometre scale. A schematic diagram of the scanning electron microscope is shown in Figure 2.9. The imaging process in an SEM relies on the interaction between the incident electron beam and the specimen's surface. These interactions produce several distinct signals, most notable secondary electrons (SE) and backscattered electrons (BSE) [109]. Secondary electrons, which are emitted from the uppermost layers of the sample with energies below 50 eV, are highly sensitive to surface geometry and a primary responsible for producing high-contrast topographical images. In contrast, backscattered electrons result from elastic scattering and possess higher energy (> 50 eV), allowing them to emerge from deeper regions [110].

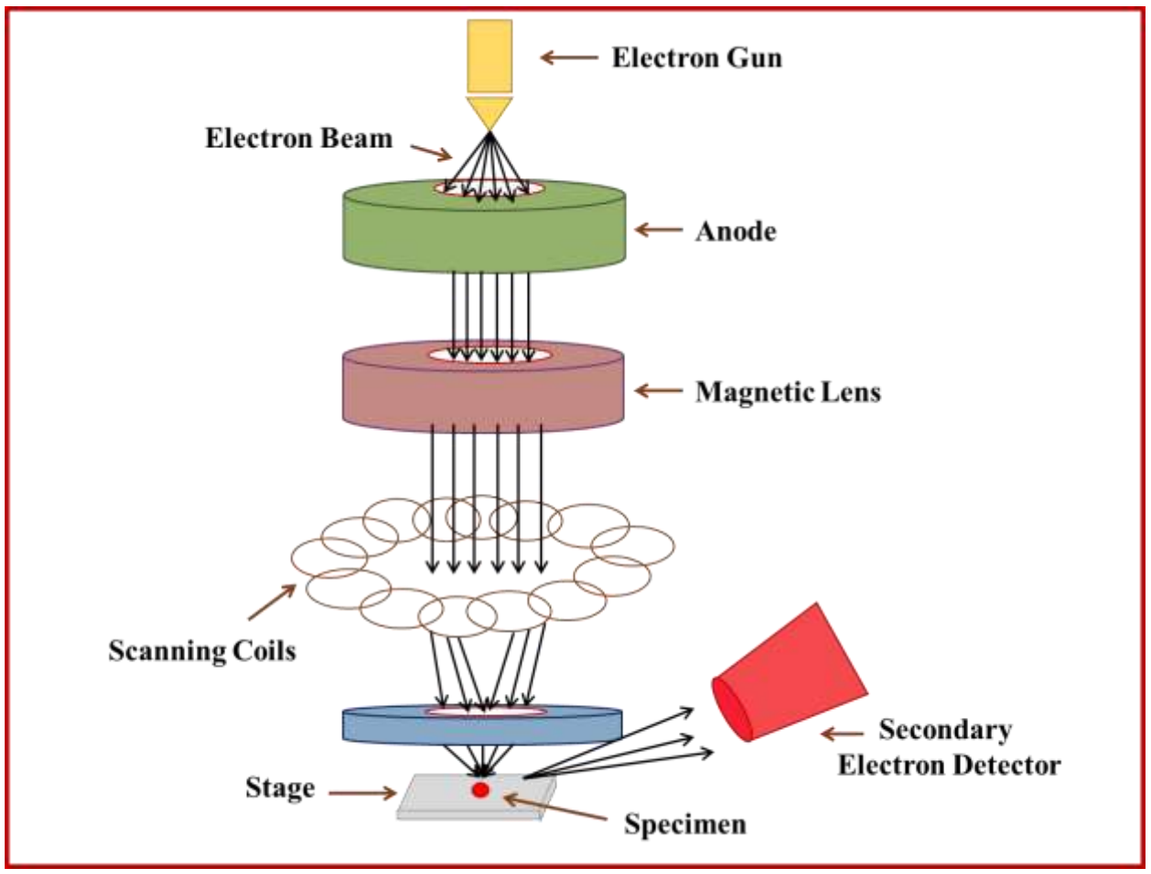

Figure 2.9 Schematic diagram showing the components of a scanning electron microscope

50 SEM is an invaluable tool for discerning variations in chemical composition as the intensity of the BSE signal is directly proportional to the atomic number of the elements present. And, heavier elements appear as brighter regions due to their higher electron-scattering efficiency. To ensure high quality imaging and prevent the accumulation of static charge (charge effect), especially non-conductive samples must be properly prepared. This typically involves mounting the specimen on conductive carbon tape and applying a nanometric coating of noble metals, such as gold (Au) or Platinum (Pt) [111]. This conductive layer facilitates a stable path for incident electrons, reducing electrostatic distortions and enhancing image clarity.

2.3.5.1 Field Emission Scanning Electron Microscopy (FE-SEM)

While conventional SEM is a powerful tool, its resolution is often limited by the thermal electron source (typically a tungsten filament), which can struggle to resolve features smaller than 50 nm. FESEM addresses this limitation by utilising a field emission gun. This source produces an electron beam that is significantly narrower, more monochromatic, and up to 1000 times higher than tradition filaments [112]. Consequently, FESEM provides superior spatial resolution (0.5 - 2

nm) and a much greater depth of field, allowing for clear visualization of ultra-fine nanostructures. In this study, surface morphology of the prepared materials and films were investigated using a JEOL 7610F Plus FESEM. This advanced system enables the capture of sharp, high-magnification images with minimal electrostatic interference, providing critical insights into the interfacial distribution of the synthesized samples.

2.3.6 Transmission Electron Spectroscopy (TEM)

TEM is a powerful analytical technique that utilizes a high-energy bean to penetrate ultrathin specimen, providing unparalleled insights into the internal morphology, crystallographic, and atomic structure of materials. Unlike SEM, which scans the surface, TEM relied on the transmission of electrons through the sample. TEM can achieve spatial resolutions down to the atomic level because the de Broglie wavelength of accelerated electrons is significantly shorter than that of visible light, making it indispensable for studying 1D and 2D nanostructures. A schematic diagram of transmission electron microscope is illustrated in Figure 2.10.

The TEM architecture consists of an electron gun that generates coherent beam of electrons, which is then accelerated through a vacuum column using high voltages (typically between 100kV and 300 kV). A series of electromagnetic condenser lenses focus this beam onto a specimen mounted on a conductive copper grid. For successful imaging, the specimen must be extremely thin, generally less than 100 nm to allow the electron beam to pass through without total absorption [113]. As the beam traverses the sample, the electrons undergo two types of scattering:

- **Elastic Scattering:** results from interactions with the atomic nuclei. This coherent scattering provides information regarding the crystal lattice and produces distinct spot or ring patterns in Selected Area Electron Diffraction (SAED) mode.
- **Inelastic Scattering:** occurring through interactions with the sample's electrons. This process results in energy loss and is used to identify the chemical composition and electronic state of the material.

The contrast in TEM images is primarily generated through the use of an objective aperture. In bright Field imaging, the aperture allows the direct transmitted beam to pass while blocking the diffracted beams. This results in a high-intensity background where dense or crystalline areas appear dark [114]. Conversely, in Dark Field imaging, the direct beam is blocked, and only specific diffracted rays are used to form the image. This highlights crystalline features and defects against

a dark background, which is particularly useful for identifying specific grain orientations in nanocomposites.

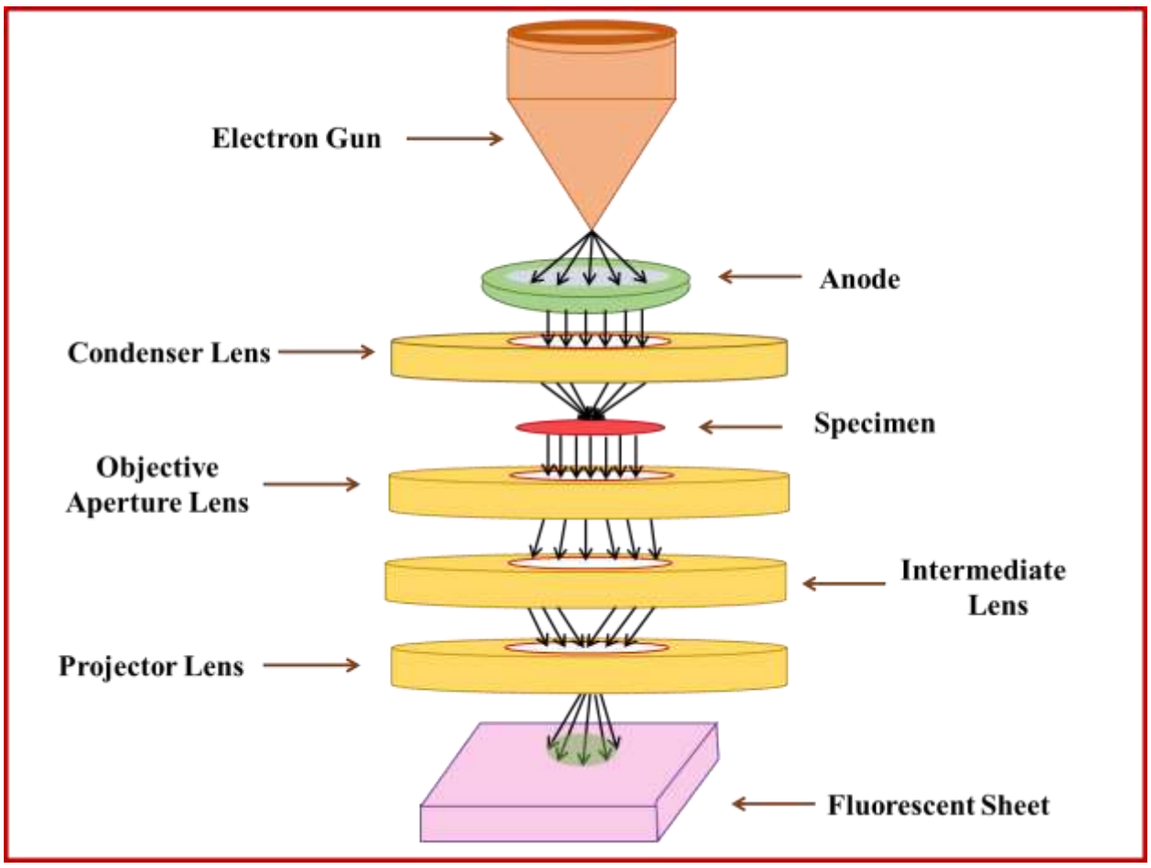

Figure 2.10 Schematic diagram representing the setup of transmission electron microscope

Moreover, at the highest levels of magnification, High-Resolution TEM (HR-TEM) allows for the direct visualization of atomic planes and lattice fringes. By increasing the accelerating voltage to 200-300 kV, the electron wavelength is further reduced, enhancing the point resolution. This mode is crucial for measuring the interplanar d-spacing of 2D materials and the selected area electron diffraction (SAED) patterns. SAED patterns provide a reciprocal space map of the crystal that confirm whether the synthesized nanostructures are single-crystalline, polycrystalline or amorphous.

2.3.7 Dielectric/Impedance Spectroscopy

Impedance spectroscopy is a fundamental characterization tool used to study the electrical dynamics, charge transport mechanisms, and interfacial polarization within nanocomposites. By applying a small AC voltage and measuring the resulting current response, this technique allows for the determination of parameters such as complex impedance (Z*), dielectric permittivity (ε*), loss and electrical conductivity (σ) etc. with respect to applied field frequency or operating

temperature. The real (ε′) component of the complex dielectric permittivity represents how well the material can store electrical energy when subjected to an external electric field. The imaginary (ε″) component provides insights about energy dissipation developed due to polarization lag that is produced on applying external electric field. The equation 2.6 is used to calculate the value of total dielectric constant (ε′). To calculate the dielectric loss (ε″) and loss tangent (tanδ) within the samples, equation 2.7 is utilized.

$$\varepsilon'(\omega) = \frac{C_p}{C_0} = \frac{C_p d}{\varepsilon_0 A} \tag{2.6}$$

$$tan\delta = \frac{\varepsilon''(\omega)}{\varepsilon'(\omega)} \tag{2.7}$$

where C_p, C_0, ε_0, A, d and ω (2πf) is the measured parallel plate capacitance, vacuum capacitance ($\varepsilon_0 A/d$), permittivity of free space (8.85×10^{-12} F/m), cross-sectional area and thickness of dielectric material, angular frequency of the applied electric field respectively; δ=(90-θ) where θ is the phase difference between the applied alternating voltage to the measured current [115].

In this study, the dielectric properties were recorded at different operating temperatures using a high-precision LCR meter across a frequency range (20 Hz to 10 MHz). The instrument functions by using an "auto balancing bridge" circuit to compare the impedance of the unknown sample against known internal standards. To perform the measurement, AC source is employed to analyze the material's response across a broad frequency spectrum. The interaction between voltage and the resulting current is monitored through a high precision analyzer, which measures critical parameters such as the phase angle, capacitance, inductance and complex impedance etc. For the experimental measurements, the specimens are placed between two electrodes to create a parallel-plate capacitor configuration. The raw data obtained from the analyzer can be converted into specific dielectric and conductive values using different analytic correlations.

2.3.8 Universal Tensile Machine (UTM)

To govern the practical viability of the nanogenerator particularly for wearable and flexible electronics, mechanical resilience is the fundamental characteristic. The nanocomposite films must be capable of withstanding continuous and high-strain deformations without undergoing catastrophic structural failure. The Universal Tensile Machine (UTM) is an instrument used to quantify the macroscopic mechanical properties of a material. It is designed to subject materials to

precisely controlled tensile, compressive, or flexural forces. In the context of flexible polymer films, it is primarily utilized to perform uniaxial tensile testing. To conduct a tensile test, a standardized specimen of the polymer film (generally cut into a rectangular shape) is securely anchored between two mechanical gripping jaws. The lower jaw is structurally fixed, while the upper jaw is attached to a motorized, movable crosshead. During the testing, the crosshead moves upward at a constant, pre-defined velocity (strain rate), actively pulling and stretching the polymer film. A highly sensitive load cell integrated into the crosshead continuously measures the instantaneous mechanical force exerted on the specimen. Simultaneously, an extensometer tracks the exact change in the length (ΔL) of the specimen. The machine keeps increasing the tensile load until the structural integrity of the polymer film fails.

The raw data generated by the UTM is a "Force vs. Extension" curve. However, this curve is heavily dependent on the specific dimensions of the tested sample. Therefore, this data is mathematically normalized into a Stress-Strain by the UTM software curve to determine the intrinsic mechanical properties of the sample.

- **Stress (σ):** It is defined as the applied tensile force normalized by the original cross-sectional area of the polymer film. It represents the internal resistance of the material to the applied deformation and can be calculated using equation 2.8.

$$\sigma = \frac{F}{A_0} \tag{2.8}$$

where F is the applied force (Newtons) and A_0 is the initial cross-sectional area (m^2).

- **Strain (ε):** It is the dimensionless measure of the physical deformation, calculated as the ratio of the change in length to the original gauge length of the sample, shown in equation 2.9.

$$\varepsilon = \frac{\Delta L}{L_0} \tag{2.9}$$

where ΔL is the extension and L_0 is the initial length of the sample.

- **Young's Modulus (E):** It is the definitive measure of the material's stiffness. Extracted from the initial, strictly linear portion of the stress-strain curve (the elastic deformation region). It defines the relationship between stress and strain before permanent plastic deformation occurs, governed by Hooke's Law:

$$E = \frac{\sigma}{\varepsilon} \tag{2.10}$$

For the development of hybrid nanogenerators, the data yielded by the UTM is of paramount importance. Pristine PVDF is renowned for its excellent mechanical flexibility. However, the foundational methodology of this research involves the incorporation of rigid inorganic nanofillers to enhance the electroactive β-phase, piezoelectric response and triboelectric surface charge. While these fillers boost the electrical output, excessive loading can lead to nanoparticle agglomeration, which disrupts the polymer chain continuity and leads to the brittleness in the PVDF matrix. The UTM provides the critical validation needed to optimize the filler concentration. By analyzing the ultimate tensile strength (the maximum stress the film can withstand) and the elongation at break (the maximum strain before rupture), the UTM ensures that the prepared nanocomposites achieve an optimal balance i.e, maximizing energy-harvesting capabilities while retaining the vital structural flexibility required for long-term and self-powered wearable applications.

2.3.9 Electrical Measurements for Nanogenerator Performance

To evaluate the power generation capabilities of the fabricated Piezoelectric Nanogenerator (PENG) and Triboelectric Nanogenerator (TENG), a systematic electrical characterization has been employed. To generate stable electrical contact, metallic electrodes were placed onto the surfaces of the PVDF based thin films. The mechanical stimulation required to produce the piezoelectric and triboelectric responses was provided by a dynamic shaker (Micron MEV-0025) and palm tapping. The resulting electrical outputs were captured and analyzed using high precision instruments. The generated output voltage was monitored using a digital storage oscilloscope (Tektronix MDO34), while a Keithley digital multimeter (DMM7510) was employed for accurate current measurements. To assess the practical energy conversion efficiency, silicon (Si) diode-based bridge rectifier circuits were integrated into the setup to measure the rectified DC output voltage and current. Finally, demonstrated the potential of these fabricated devices to generate power for low power electronics, such as LEDs, capacitors etc.

2.3.10 Electrochemical Characterization: Cyclic Voltammetry (CV)

To transition from a transient energy harvester to a Self-Charging device or piezo-supercapacitor, the active materials must demonstrate high charge retention, rapid ion transfer, and long-term electrochemical stability. Cyclic Voltammetry (CV) serves as the premier electroanalytical

technique to investigate these complex interfacial phenomena. It provides a direct macroscopic measurement of the material's capacitive behavior and energy storage mechanisms. Cyclic Voltammetry operates by continuously cycling the electrical potential of a working electrode and measuring the resulting current response. The standard experimental configuration utilizes a controlled three-electrode system immersed in an aqueous or solid-state electrolyte (e.g., KOH or PVA-KOH gel).

- **Working Electrode:** The substrate coated with the synthesized active nanocomposite (e.g., PVDF, Metal Oxide etc.), where the fundamental charge storage or Faradaic redox reactions occur.
- **Reference Electrode:** A stable baseline electrode (commonly Ag/AgCl) that maintains a constant thermodynamic potential. It ensures that the voltage applied to the working electrode is accurately measured.
- **Counter Electrode:** An inert conductor (such as a Platinum wire) that completes the electrical circuit, allowing current to flow without interfering with the reactions at the working electrode.

During a CV sweep as shown in Figure 2.11 (a), a potentiostat applies a linearly varying voltage between the working and reference electrodes. The varying voltage starts from an initial potential, reach up to a defined upper limit, and then reverses back to the starting point as shown in Figure 2.11 (b). The rate at which this voltage changes is defined as the scan rate (ν). The resulting data is plotted as a voltammogram (Current vs. Potential). The precise shape of this CV curve is the primary diagnostic tool used to deduce how a material stores energy. By examining the symmetry of these curves at progressively higher scan rates (e.g., 5 mV/s - 150 mV/s), one can assess the rate capability of the device. Beyond qualitative shape analysis, the CV voltammogram is mathematically integrated to precisely calculate the absolute energy storage capacity of the nanocomposite. The total charge (Q) stored during a sweep is directly proportional to the integrated area under the CV curve. To determine the Specific Capacitance (C_s) or Areal Capacitance (C_A), equation 2.11 has been employed.

$$C_s = \frac{\int I dV}{2m\nu\Delta V} \tag{2.11}$$

Where, ∫IdV represents the integrated area of the cyclic voltammogram loop, m is the active mass of the electrode material, ν is the applied voltage scan rate (dVdt), and ΔV is the operational potential window.

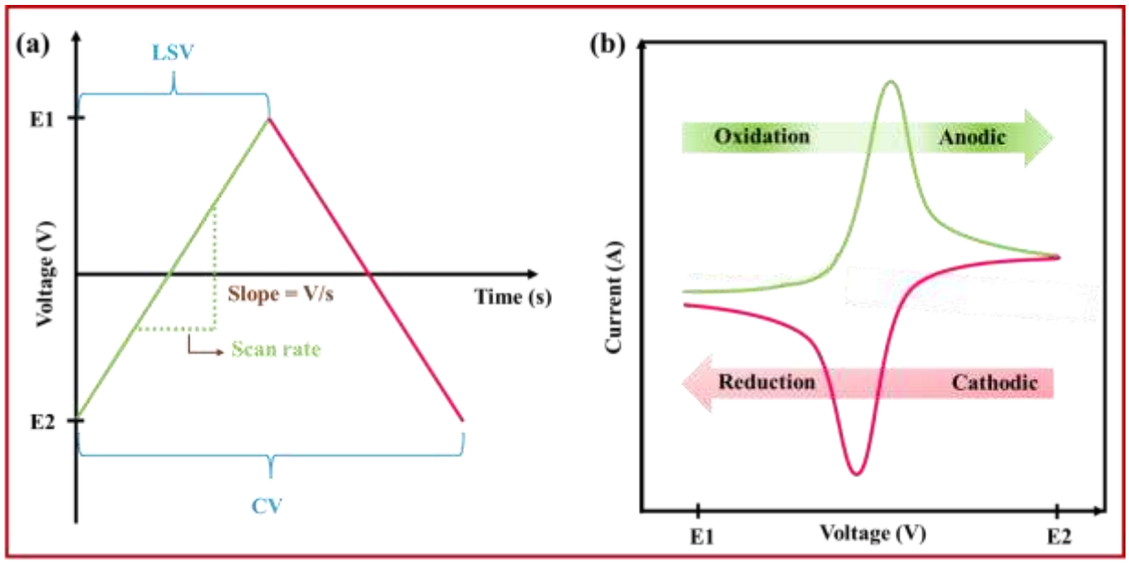

Figure 2.11 Schematic diagram of (a) potential as a function of time and (b) current as a function of voltage for a typical cyclic voltammogram

Once the specific capacitance is empirically established, the overall Energy Density (E) of the self-charging system can be derived using the fundamental capacitive energy equation 2.12.

$$E = \frac{1}{2} C_s (\Delta V)^2 \tag{2.12}$$

Additionally, CV is utilized to validate the operational lifespan of the energy storage device. By subjecting the material to thousands of continuous charge-discharge cycles (at a constant scan rate), the degradation of the active material can be tracked. It analyses the structural and electrochemical durability of the nanocomposite, validating its efficacy as a long-term, self-sustained power source.

CHAPTER 3

Exploration of Structural and Dielectric Properties of Ta_2O_5 at Different Sintering Temperatures

The tantalum pentoxide (Ta_2O_5) nanostructures have been synthesized using hydrothermal method and calcined at different temperatures. X-ray diffraction (XRD) confirms the formation of highly crystalline and orthorhombic phase of the nanostructures calcined at 800-1200 ºC. FTIR and Raman spectra of the synthesized nanostructures were obtained to further confirm the successful synthesis of Ta_2O_5. The energy band gap of the prepared Ta_2O_5 has been calculated ~ 3.8 eV using UV-visible absorbance spectroscopy. Further, Ta_2O_5 has been sintered at different temperatures, and their dielectric characteristics have been investigated in the temperature range of 80 K to 400 K and applied field frequency of 20 Hz to 2 MHz. The experimentally obtained dielectric results indicate that both the dielectric constant (ε) and dielectric loss (D) values increase with increasing operating temperature. At 300 K and 1kHz, the value of ε becomes almost twice i.e. from 10 to 20 on increasing the sintering temperature from 400 ºC to 950 ºC. The enhancement in dielectric constant can be justified by the thermally activated orientational and interfacial polarization associated with the increase in the grain size of the Ta_2O_5 nanostructures at higher sintering temperatures. Furthermore, the frequency dependence of ε indicates the high effect of the distribution of relaxation time in the Ta_2O_5 nanostructures at lower frequencies. Overall, this study provides a better understanding of the structural and dielectric behaviour of Ta_2O_5 nanostructures in correlation with varying sintering temperature. The results suggest that the orthorhombic Ta_2O_5 nanostructures have potential applications as alternative dielectric materials in various electronic and optoelectronic devices.

3.1 Introduction

Nanostructures of tantalum pentoxide (Ta_2O_5) have garnered significant interest among scientific community due to their versatile properties such as good ductility, high refractive index, low defect density, eco-friendliness, and great chemical stability [89,116,117]. These properties make them highly promising for applications related to photocatalytic activities [88,118], sensors [119,120], energy storage [121] and memristive devices [122,123], anti-reflection coatings [124], dielectric [125,126] and optoelectronics devices [127] etc. Among them the dielectric characteristics of nanoscale Ta_2O_5 found major significance towards utility across various domains, including optical systems [127,128], electronic components [125], supercapacitors [92] and lithium-ion batteries [129] etc. Ta_2O_5 exists in multiple phases, according to the method of preparations and growth conditions, their crystallographic phases can be divided into two groups: (a) low temperature (L (600 – 1360 ºC)), (b) high temperature (H (above 1360 ºC)) [130–132]. Ta_2O_5 is a highly polarisable dielectric substance, which makes it popular in the dielectric sector. Also, advantages such as low energy losses, high breakdown strength, high dielectric constant, low leakage current and good thermal stability adds to the nobility of Ta_2O_5 nanostructures [89,117,130].

Therefore, dielectric study of Ta_2O_5 becomes a favourite choice of researchers for above mentioned applications. In this direction most of the dielectric work on this material is focused on nanostructured thin films [133–136]. It has been reported that the dielectric properties of Ta_2O_5 nanostructures can be tuned by varying its (i) crystal structure, (ii) applied frequency of the field, (iii) sintering temperature, (iv) morphology, (v) particle size, and (vi) presence of defects and pores etc [137–140]. P. C. Joshi and M. W. Cole investigated the effect of postdeposition annealing on the dielectric and structural properties of amorphous and crystalline Ta_2O_5 thin films. They showed that the crystalline films have better dielectric results as compared to amorphous films [133]. Likewise, P. Thapliyal et al. studied the structural and dielectric behaviour of Ta_2O_5 - TiO_2 composite thin films with at different annealing temperature. Their results confirm that the dielectric constant enormously depends on annealing temperature. The obtained results were explained on the basis of improved crystallization, reduced stress, reduced oxygen vacancies and bond defects in the film [136,137].

Interestingly a very few research has been carried out which explores the temperature and field frequency dependent dielectric properties of Ta_2O_5 with its different morphologies such as

nanoparticles, nanorods, fibres, nanosheets, and nanoplatelets etc. Such as, W. Miao et al. prepared the thin film of vertically aligned Ta_2O_5 nanorods using thermal deposition method and reported their dielectric constant to be 20 in the frequency range of 1 KHz to 10 MHz [141]. Similarly, R.C. Hoffmann et al. reported the dielectric study of Ta_2O_5 nanoparticles synthesized using microwave processing technique with the dielectric constant of 15 [87]. However, they have not studied the sintering effect on the structural and dielectric properties. Also, the effect of operating temperature on dielectric behaviour has not been investigated. As sintering temperature is also important to study the dielectric behaviour of nanostructures because it helps in increasing packing fraction, promotes grain growth, reduce the oxygen vacancy and defect density in the material. Thus, the effect of sintering temperature on structural and dielectric properties of Ta_2O_5 becomes indispensable.

In the present study we have synthesized highly crystalline orthorhombic phase of Ta_2O_5 nanostructures using hydrothermal method. To articulate the aforementioned limitations, the effect of sintering temperature on dielectric properties of Ta_2O_5 has been investigated, Further, dependency of operating temperature (80 - 400 K) and frequency of applied field (20 Hz - 2MHz) on dielectric behaviour has also been discussed. Additionally, comparative analysis of dielectric behaviour of Ta_2O_5 nanostructures sintered at different temperature were done that is the novelty of this research. Our findings suggests that Ta_2O_5 nanostructures (i) change their crystal structure and grain size with sintering temperature, (ii) the measured dielectric constant increases with operating and sintering temperature, and (iii) the improved dielectric behaviour with sintering temperature has been explained on the basis of interfacial and space charge polarization. The results suggest that Ta_2O_5 nanostructures can be a potential candidate to replace the other dielectric material because of their highly favourable and tunable properties.

3.2 Experimental Section

Tantalum pentachloride ($TaCl_5$ - 99.5%) and Hydrogen peroxide (H_2O_2 - 99%) of high purity were purchased from Thermofisher Scientific. Figure 3.1 shows the schematic diagram of the whole synthesis process. 1.8 gm of $TaCl_5$ powder was dispersed in 40 ml ethanol and H_2O_2 solution and ultrasonicated for 30 min. Subsequently, 20 ml of deionised water was added dropwise, followed by stirring for additional 30 min. The whole solution was transferred to 100 ml Teflon-lined autoclave and heated at 200 ^{0}C for 24 h. After natural cooling of the hydrothermal reactor,

suspension was filtered and washed several times with deionized water using centrifugation process. The resulting precipitate was collected and dried at 80 ^{0}C overnight in a vacuum oven. After that, the collected powder was calcinated at different temperature ranging from 600-1200 ºC. the sample sintered at 800 ºC was further selected for the dielectric analysis. The polyvinylidene fluoride as a proper binder with 10 wt% concentration was added in the 1:10 weight ratio and using the hydraulic press with the pressure of approximately 2 tons (~150 MPa), pellets (13 mm diameter) of the sample were prepared. The process was further followed with a sintering phenomenon by placing the pellets in the furnace at temperatures 400, 700 and 950 ºC for 6 hours.

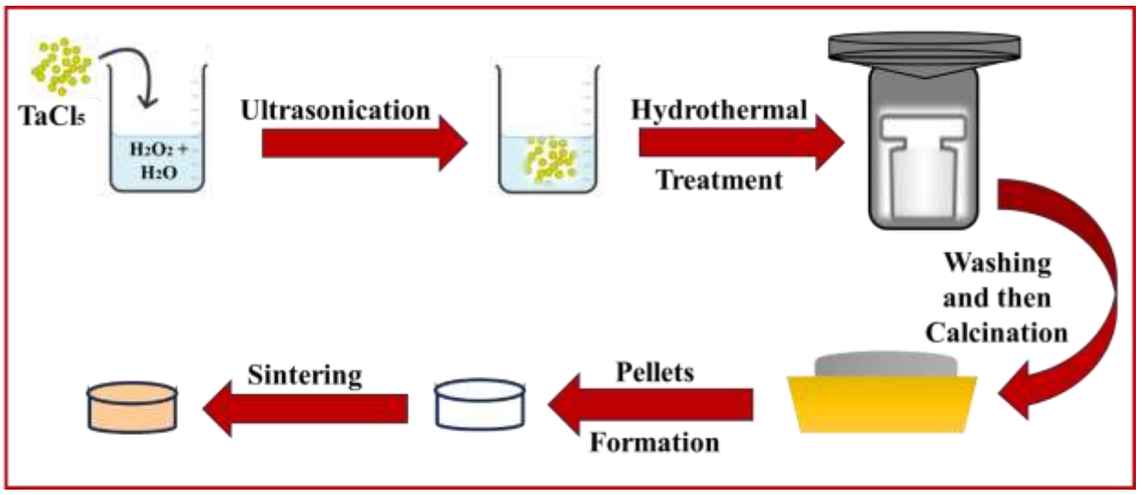

Figure 3.1 Schematic diagram showing the synthesis steps for Ta_2O_5 nanoparticles

The dielectric measurements were based on the capacitance method. The two electrodes were prepared on both sides of the pellet using silver paste and heated at 80 ºC for 1 hour. The frequency and temperature response of the dielectric constant and loss tangent were investigated using an Agilent LCR meter (Model E4980A) and a lakeshore temperature computer (Model 340).

3.3 Results and Discussion

3.3.1 X-ray Diffraction (XRD)

The XRD patterns of the Ta_2O_5 calcinated at different temperatures has been shown in Figure 3.2. The diffraction pattern of sample at room temperature show amorphous nature and after calcination at 600 ºC, Ta_2O_5 shows major peaks of the hexagonal phase (δ) and all the peaks are following JCPDS data (file no.: 00-19-1299) [142]. Further, on calcinating the sample at 800-1200 ºC, the diffraction peaks at 2θ ~ 50.68º start splitting into two peaks. The other peaks do not show any apparent shift or change with respect to 2θ and the full width at half maximum (FWHM) decreases

hence the crystallite size increases. The diffraction peaks for the samples calcinated at 800-1200 ºC at 2θ ~ 22.90, 28.46, 36.84, 46.83, 49.78, 50.75 and 55.66 are corresponds to (001), (1 11 0), (1 11 1), (002), (0 22 0), (2 15 1), and (0 22 1) lattice planes of orthorhombic phase of Ta_2O_5, respectively, and are in good agreement with the standard JCPDS data (file no.: 25-0922) [142]. The two new diffraction peaks appeared at 49.78º and 50.75º due to splitting of the peak at 2θ ~ 50.68º corresponds to lattice planes (0 22 0) and (2 15 1) of orthorhombic phase of Ta_2O_5, respectively. This splitting of the peak indicates the transformation of crystal structure from hexagonal to orthorhombic phase of the Ta_2O_5 nanostructures.

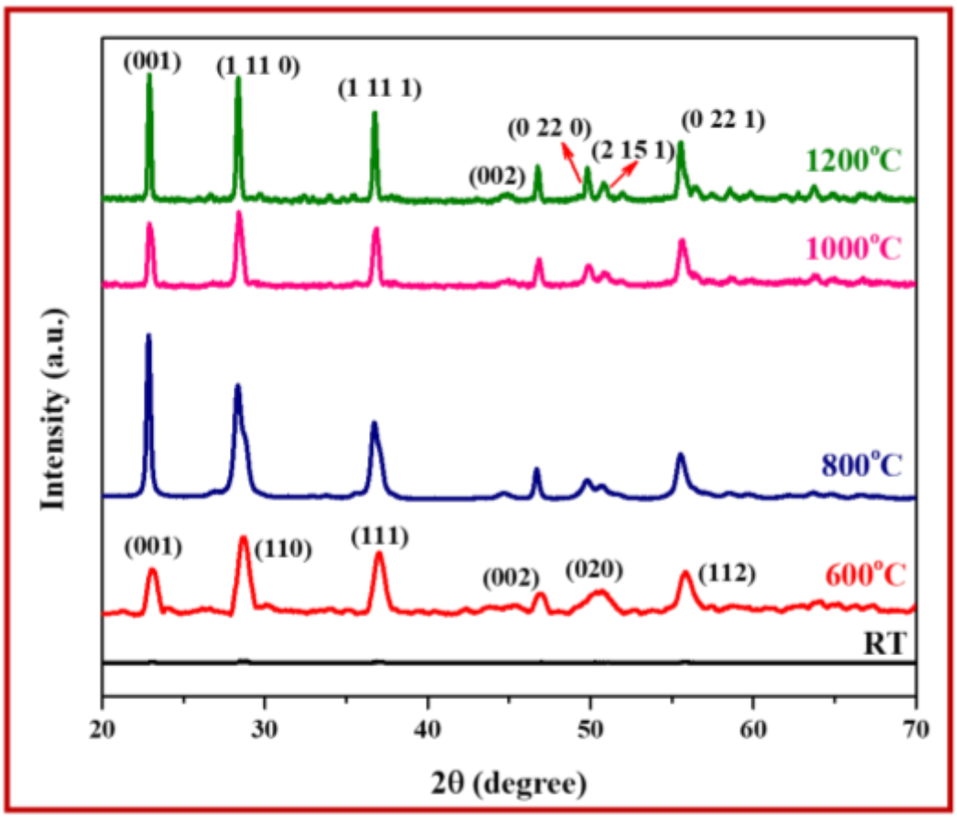

Figure 3.2 XRD pattern of synthesised Ta_2O_5 calcinated at different temperatures

3.3.2 Morphological and Composition Analysis

65

The field emission-scanning and transmission electron microscopic (FE-SEM & TEM) images of the synthesized Ta_2O_5 has been shown in Figure 3.3. It can be observed from the FESEM and High-magnification TEM images that the synthesized sample consists of irregular shape particles. Their average particle size calculated from particle size distribution curve (Figure 3.4 (a)) plotted using ImageJ software is ~ 69 nm. During sintering, particles are expected to rearrange themselves to reduce their total surface energy which also results in larger grain growth [143].

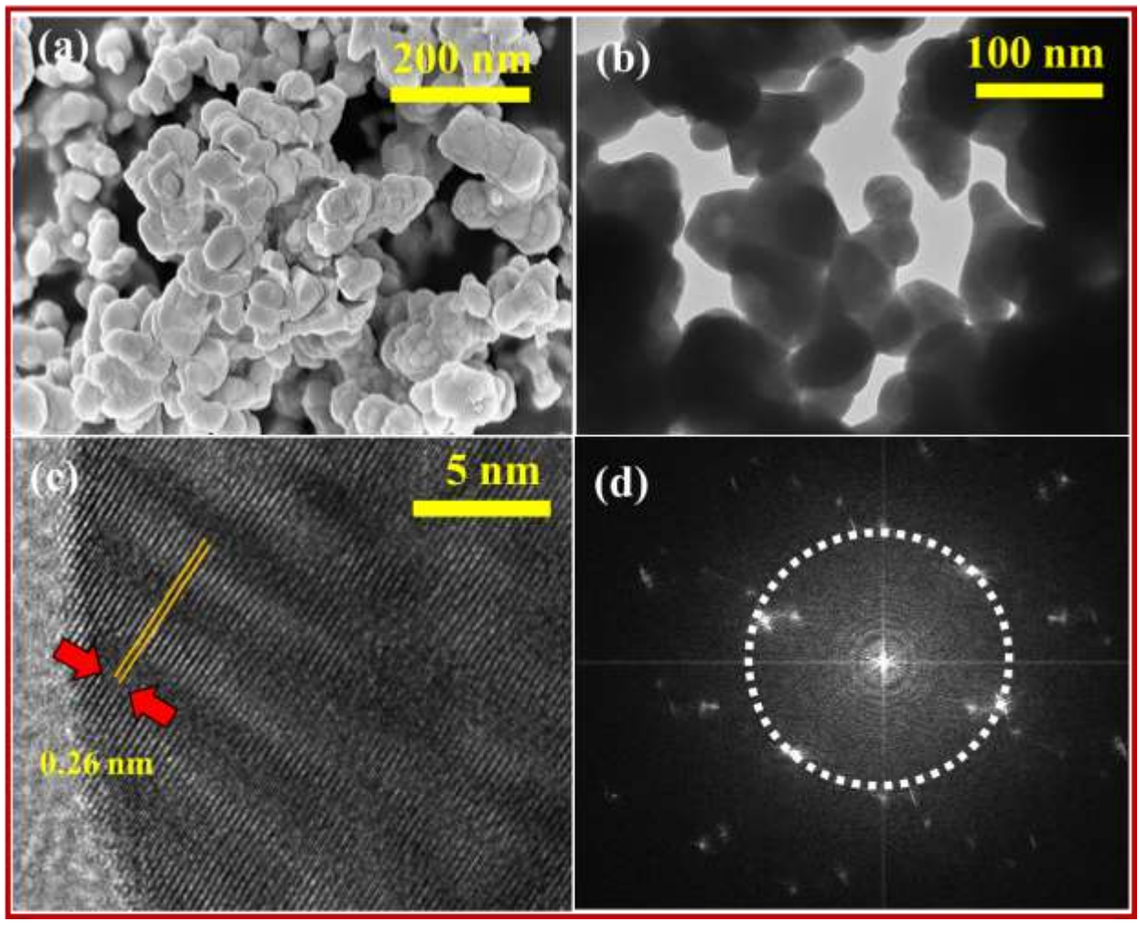

Figure 3.3 (a) FE-SEM image, (b & c) TEM images and (d) SAED pattern of synthesized Ta_2O_5 nanostructures calcinated at 800 °C

The obtained ring pattern in the selected area electron diffraction (SAED) and fringes pattern (Figure 3.3 (c & d)) shows the polycrystalline nature of the sample. The visible parallel lattice fringes in different orientations correspond to different planes. The interplanar distance (d) between two consecutive parallel fringes is ~ 0.26 nm which can be associated with the (1 11 0) lattice planes of orthorhombic phase. The bright points in SAED pattern show the crystalline nature of the sample that is in accordance with the XRD measurements, indicating that the Ta_2O_5 nanostructures are orthorhombic crystals.

Further, the chemical compositional analysis and elemental distribution of the synthesized samples were carried out using the energy dispersive spectroscopic (EDS) technique. The EDS pattern (Figure 3.4 (b)) shows the characteristic peaks of Ta and O components, no other peaks are found which confirms the impurities-free synthesis of Ta_2O_5 nanostructures. The perfect stoichiometry of Ta_2O_5 (O: Ta atomic%) should be 2.5 and the measured O: Ta (atomic%) is more than 2.5. The presence of this excess amount of oxygen on the synthesized sample pellet may be due to the

adsorption of atmospheric oxygen on the pellet's surface as there was no heat treatment before the EDS measurement to remove the adsorbed atmospheric gases.

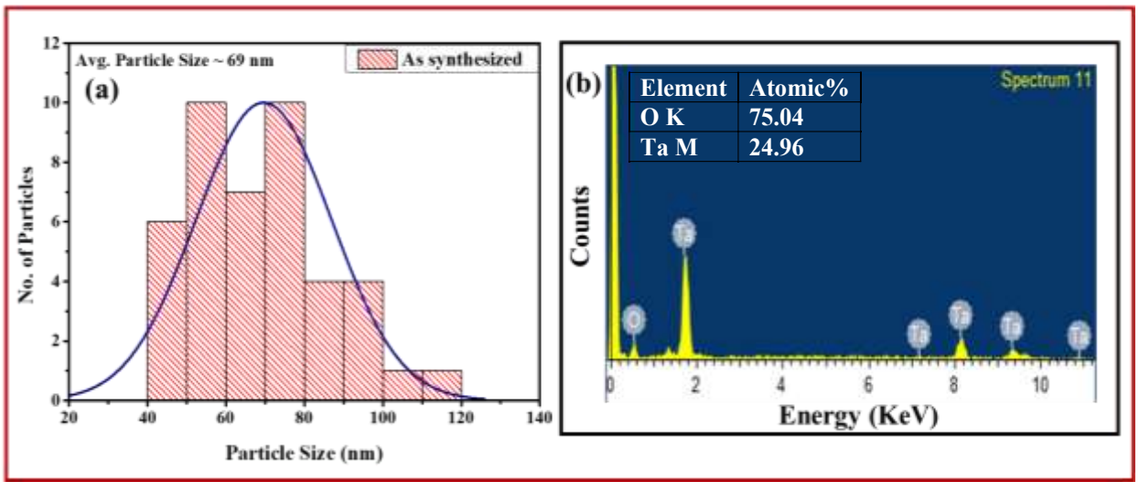

Figure 3.4 (a) Particle distribution histogram calculated from SEM micrograph and (b) EDS pattern of the synthesized Ta_2O_5

3.3.3 UV-Visible Absorption and FT-IR Spectra

UV-visible absorption and FT-IR spectra of the synthesized Ta_2O_5 nanostructure has been shown in Figure 3.5 (a and b). The obtained UV-visible spectra exhibit strong absorption peaks at 220 and 280 nm for all the samples. This can be attributed to the sample's strong light absorption, which is often linked with optical transitions through the energy gap of the different-sized particles. The Tauc plot, a graph between $(\alpha h\nu)^{1/n}$ and photon energy is shown in the inset of Figure 3.5 (a) where α is the absorption coefficient, h is Planck's constant and ν is the frequency of the light and n is Tauc exponent. The optical energy band gap of the sample was obtained using the Tauc plot by extrapolating the linear section of the graph [144]. In our analysis, the best-fitted values correspond to the linear section for n=1/2, indicating that Ta_2O_5 nanostructures have a direct energy band gap of ~ 3.8 eV [145].

To identify the functional groups and bonding between the atoms FT-IR spectra was obtained. Figure 3.5 (b) illustrates the FT-IR spectra of synthesized sample. The stretching vibrations of the Ta-O and Ta-O-Ta bridges are responsible for the energy absorbed by the molecules at the wavenumbers 512 and 828 cm^{-1} respectively [146].

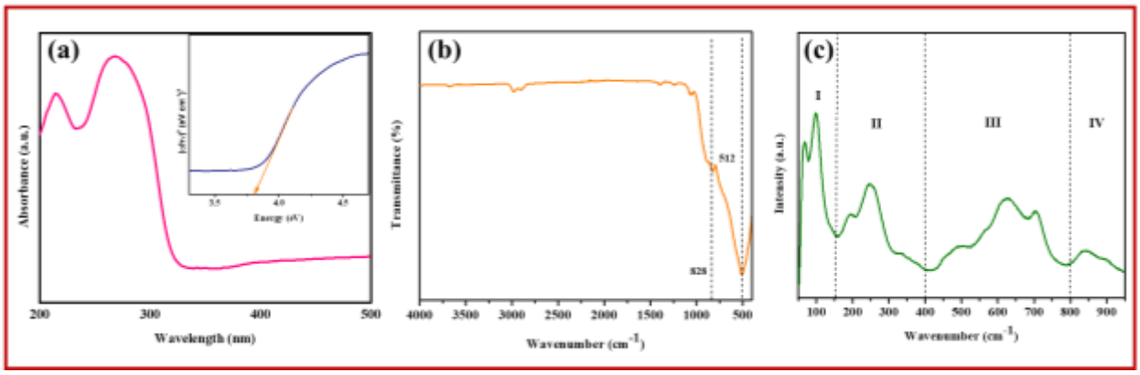

Figure 3.5 (a) UV-Visible Spectra, (b) FTIR, and (c) Raman spectra of synthesized Ta_2O_5 nanoparticles

3.3.4 Raman Spectra

Literature suggests, local arrangement of Ta and O in various crystalline phases of Ta_2O_5 includes TaO_8 hexagonal bipyramid, TaO_7 pentagonal bipyramid and TaO_6 octahedron [147]. These polyhedral can share their edges and corners, resulting in two-coordinated and three-coordinated oxygen structures known as O-2Ta and O-3Ta, respectively [129]. The obtained Raman spectra are divided into four regions according to the different vibrational modes within these polyhedra of Ta_2O_5 as shown in Figure 3.5 (c). In region I (wavenumber, $\bar{\upsilon} < 150$ cm^{-1}), peaks at ~ 68 and 100 cm^{-1} are highly likely to originate from an external vibrational mode that may include interactions between different corners or edge-shared polyhedra. Raman bands in region II ($150 < \bar{\upsilon} < 400$ cm^{-1}) correspond to the deformation mode that includes the internal O-Ta-O bending vibrations in TaO_6 octahedra. The higher energy bands in regions III and IV ($400 < \bar{\upsilon} < 900$ cm^{-1}) are due to internal stretching mode due to triple-coordinated oxygen (O-3Ta) and double-coordinated oxygen (O-2Ta), respectively [147,148].

3.3.5 Dielectric Measurements

A valuable insights and useful information about the relaxation mechanism, electric field distribution and energy dissipation within the material can be obtained from the field frequency and temperature dependent dielectric measurements. The dielectric constant/electric permittivity (ε), and dielectric loss (D) are the two physical measurable properties that can be determined through the dielectric behaviour of a material [115]. Where the ε represents how well the material can store electrical energy when subjected to an external electric field, while D provides insights about energy dissipation developed due to polarization lag developed on application of external

electric field [149]. It has been reported that the dielectric relaxation and electrical conduction both are responsible for the dielectric loss inside a material [150]. Further, both ε and D change with operating temperature, applied field frequency, orientation, pressure, particle size, morphology, molecular and crystal structure of materials [140]. The equation 1 and 2 are used to calculate the values of total dielectric constant and the dielectric loss, respectively. Whereas, ε′ and ε″ are the real and imaginary parts of dielectric constant (equation 2) [115].

$$\varepsilon(\omega) = \frac{C_p}{C_0} = \frac{C_p d}{\varepsilon_0 A} \quad (1)$$

$$D = tan\delta = \frac{\varepsilon''(\omega)}{\varepsilon'(\omega)} \quad (2)$$

where C_p, C_0, ε_0, A, d and ω (2πf) is the measured parallel plate capacitance, vacuum capacitance ($\varepsilon_0 A/d$), permittivity of free space (8.85×10^{-12} F/m), cross-sectional area, thickness of dielectric material, angular frequency of the applied electric field respectively; δ=(90-θ) where θ is the phase difference between the applied alternating voltage to the measured current.

3.3.5.1 Temperature Dependence

The operating temperature influences carrier hopping, whereas the sintering temperature affects grain size and grain boundaries, causing variations in electric permittivity [137,151]. The variations of the ε with the temperature, at different frequencies are represent in Figure 3.6 (a-c). At lower frequency (1KHz), ε of the bulk samples were calculated at room temperature. The obtained ε values are 11.5, 18 and 19.5 for the samples sintered at 400 ºC, 700 ºC and 950 ºC, respectively. The increase in ε values on increasing the sintering temperature may be attributed to the (i) structural transformation/distortion, (ii) increase in particle size, (iii) increase in grain size or (iv) change in material composition [137,138,140]. In our case, elevated sintering temperature promoted grain growth, particle size, reduction in oxygen content and transformation of crystal structure of the nanostructures, among which grain growth majorly contributes to the improvement of the value of ε. As EDS results show decrement in oxygen content with sintering temperature, the decrement in oxygen content is certainly not related to the oxygen vacancies because according to the literature, increase in oxygen vacancies will decrease the dielectric constant [136,137]. The mechanism involved can be understood using the Maxwell-Wagner model and the Koops phenomenological theory [151,152]. A dielectric substance, according to this paradigm, can be imagined of as a larger number of well-conducting grains separated by poorly conducting grain

boundary regions. Under the influence of the externally applied field, charge carriers easily flow across grains and accumulate at grain boundaries.

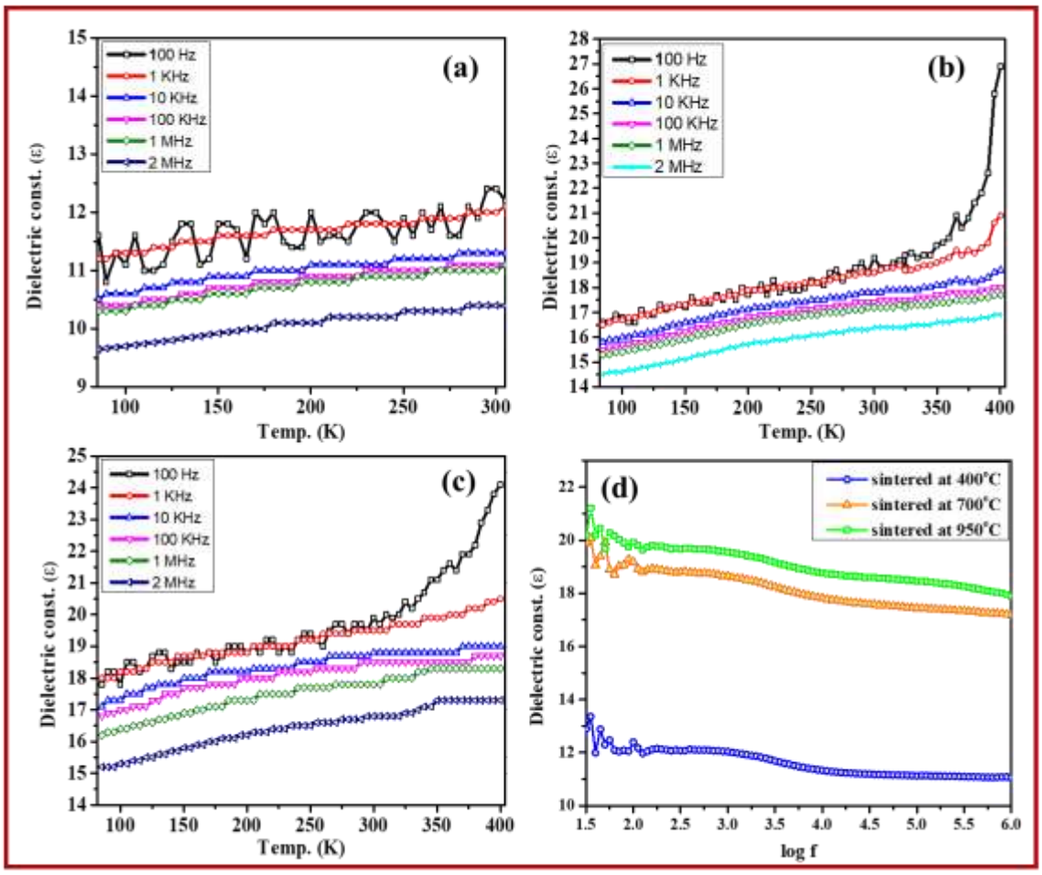

Figure 3.6 Dielectric constant (ε) curves of Ta_2O_5 as a function of operating temperatures at different frequencies for sample sintered at (a) 400 ºC, (b) 700 ºC, (c) 950 ºC and (d) comparative graph of dielectric constant at 300 K

This charge accumulation promotes interfacial polarization, resulting in an increase in permittivity [153]. Also, the orientation charge carriers along with the applied field is easier in larger grains as compared to small ones as demonstrated in Figure 3.7. The easier charge orientation helps towards enhanced permittivity of the sample sintered at 950 ºC.

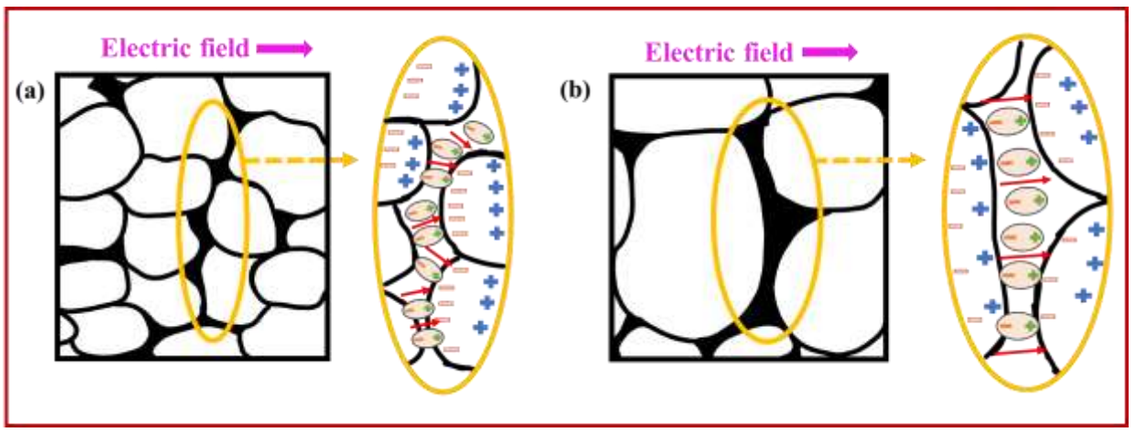

Figure 3.7 Schematic diagram representing the orientation of charge carriers along with the applied field for (a) smaller (sample sintered at 400 ºC) and (b) larger (sample sintered at 950 ºC) grains

Furthermore, the increase in operating temperature enhances the orientation of the charge carriers in direction of the external electric field thus increasing orientational polarization. This orientational polarization, is associated with the thermally induced activation of the charge carriers [150]. The variation of calculated ε with field frequency 300 K is shown in Figure 3.6 (d).

Figure 3.8 depicts the fluctuation of dielectric loss with temperature at various frequencies. The dielectric loss can be mainly influenced by operating temperature and charge carrier mobility [150]. It can be observed from the results that the dielectric loss reduces as the sintering temperature increases. As sintering at high temperature allows atomic or molecular flaws in the nanostructures to realign and relax, that helps in enhancing polarization thus total energy loss owing to dielectric dissipation is reduced, resulting in a lower dissipation factor [154]. On the other hand, it is noted that the dielectric loss may begin to grow along with the operating temperature for all the samples. This increase in the dissipation factor indicates greater energy loss within the material that can be contributed to the mobility of charge carriers and initiation of thermal deterioration at high temperatures. Also, as the operating temperature rises, the thermal agitation of atoms and molecules becomes more noticeable. That enhances their thermal motion which results in additional vibrational and rotational energy losses, resulting in a greater overall dielectric loss [150,151].

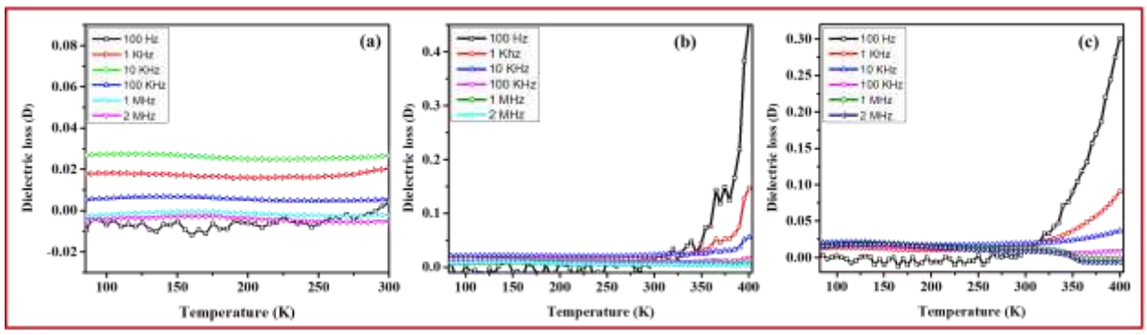

Figure 3.8 Dielectric loss curves of Ta_2O_5 as a function of the operating temperature at several frequencies for sample sintered at (a) 400 ºC, (b) 700 ºC, and (c) 950 ºC

3.3.5.2 Applied Field Frequency Dependence

Figure 3.9 depicts the fluctuation of the dielectric constant as a function of applied field frequency at various operating temperatures. A drop in dielectric constant is observed as frequency rises. This trend is in accordance with the literature [141,152]. At different frequencies, distinct types of polarization such as atomic, ionic, electronic, and interfacial polarization dominate the entire dielectric polarization; dielectric characteristics are strongly reliant on the frequency of the external electric field [154,155]. At lower frequencies, the highly scattered region with higher permittivity values were detected, indicating the dielectric dispersion in the samples.

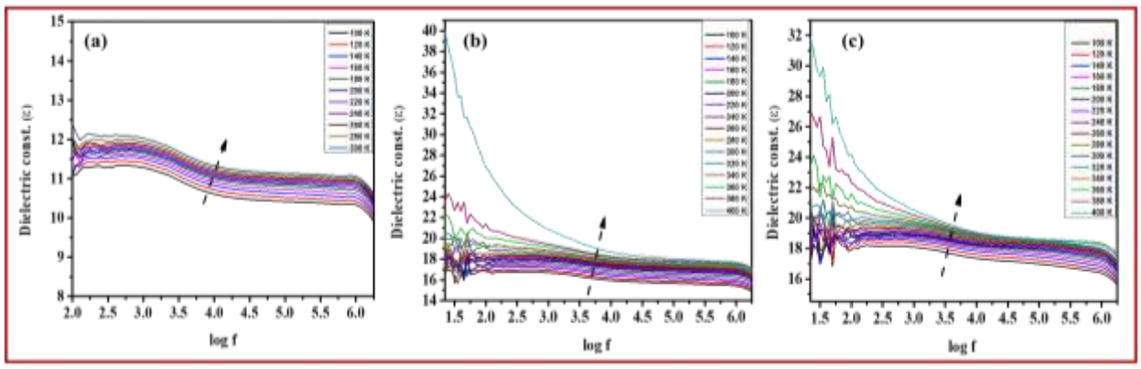

Figure 3.9 Dielectric constant (ε) curves of Ta_2O_5 as a function of frequency at several operating temperatures for (a) as-synthesized sample, (b) sample sintered at 700 ºC, and (c) 950 ºC

The greater dielectric constant at lower frequencies can be explained by the polarization relaxation phenomenon [156]. In this concept, charge carriers follow the applied field at lower frequency values, resulting in enhanced polarization and higher permittivity values. At higher frequencies, however, the carriers do not completely follow the applied field because the time period is

significantly shorter. Thus, the charge carriers could not be able to aligned in the field direction with the applied field frequency. Therefore, the net polarization decreases and consequently, the dielectric constant falls. Moreover, it is observed that at higher frequencies dielectric constant remains relatively steady along with the frequency (1KHz - 1MHz) of applied field. This characteristic is similar to the micro capacitor structure model [149].

Overall, the obtained results suggest that the Ta_2O_5 nanostructures sintered at 950 ^{0}C offers stable and high dielectric constant (ε) and lower dielectric loss (D) with varying operating temperature and applied field frequency.

3.4 Conclusion

In this study, we have delved into the dielectric characteristics of hydrothermally synthesized Ta_2O_5 orthorhombic nanostructures, with a particular focus on elucidating the influence of sintering temperature, applied field frequency (ranging from 20 Hz to 2 MHz) and operating temperature (from 80 K to 400 K). The comprehensive characterizations of the prepared nanostructures were performed to validate their crystal structures, morphological attributes, functional groups, and their dielectric properties. XRD analysis confirms the crystal structure transformation from hexagonal to orthorhombic phase on increasing the calcination temperature. Concurrently, the crystallite size demonstrated an increase corresponding to the elevation of the sintering temperature ranging from 29 nm to 53 nm. Remarkably, Ta_2O_5 nanostructures sintered at 950 ºC exhibited substantial dielectric constant, registering 19 and 25 at 100 Hz for room temperature and 400 K, respectively. This temperature-dependent behaviour highlights their adaptability across diverse operational conditions. The sintering process increased the dielectric constant to ~25 coupled with a reduction in the dielectric losses to < 0.025 within the nanostructures. The observed improvement in the dielectric properties is attributed to the thermally activated charge carriers, enhanced grain size and the effects of the orientational and interfacial polarization. This investigation affirms the potential utility of Ta_2O_5 nanostructures as a dielectric material in electronic devices for the advancement of next generation energy storage devices

CHAPTER 4

8

Optimizing Dielectric and Mechanical Characteristics of Ta_2O_5 Reinforced PVDF Flexible Nanocomposite Films

In this work, flexible nanocomposite thin films of polyvinylidene fluoride (PVDF) polymer matrix reinforced with tantalum pentoxide (Ta_2O_5) nanofillers of different weight ratios were prepared using a facile solution casting technique. The dielectric behaviour of the nanocomposite films as a function of frequency (20 Hz – 10 MHz) and temperature (30-120^{0}C) has been studied through impedance spectroscopy. Typically, the polymeric film containing Ta_2O_5 nanoparticles (NPs) in 1.25 wt% at 1 KHz field frequency possesses a dielectric constant of ~17 and 40 at room temperature and 120^{0}C respectively, which is much higher than that of pure PVDF, along with relatively low (<0.3) dielectric loss. Further, mechanical study of thin films suggests that addition of Ta_2O_5 nanofillers also increases their tensile strength and elasticity. The improved dielectric and mechanical performance enable these nanocomposite thin films to meet the requirements of present demand of the flexible electronic and energy storage industries.

4.1 Introduction

The demand for flexible, lightweight, and high-performance dielectric materials has been growing rapidly, driven by advancements in flexible electronics [72,108,157,158], energy storage devices [159–162], and wearable technologies [163,164]. Polyvinylidene fluoride (PVDF) is a well-known polymer matrix widely used for such applications due to its excellent flexibility, mechanical, and ferroelectric properties. It generally shows α, β and γ-phases, among which the content of β-phase plays a noteworthy role in influencing the piezoelectric, ferroelectric, and dielectric properties due to the molecular chain orientation with Trans configuration [165,166]. Moreover, PVDF is chemically stable and corrosion-resistant against most organic solvents, inorganic acids, and aromatic hydrocarbons [167]. It offers excellent anti-ultraviolet performance in harsh environments, robust weather resistance, and the ability to store and transport highly purified chemicals [55,167]. However, its dielectric performance, especially in terms of dielectric constant and energy dissipation, remains limited, which restricts its potential for high-performance energy storage and flexible electronic devices.

To overcome these limitations, researchers have explored the reinforcement of PVDF with various semiconductors, ceramics, and specifically inorganic metal oxides. Among the variety of inorganic metal oxides such as TiO_2, $BaTiO_3$, ZnO, SnO_2, MgO etc. proved to be an efficient nanofiller towards the improvement in the dielectric behaviour of the PVDF [168–171]. For example, Pornsawan Kum-Onsa et al. have synthesized the PVDF nanocomposite films with different volume fraction of TiO_2 nanorods using a liquid-phase assisted dispersion method. They have reported a high increment in the dielectric constant (~ 65) of the nanocomposite film with 0.5 volume fraction of TiO_2 [168]. Similarly, Abhishek Thakur et al. group enhanced the dielectric properties of PVDF film with the addition of 0.1 wt% SnO_2 nanoparticles [169].

On the other hand, to achieve a high dielectric constant, the filler percolation threshold is readily surpassed, resulting in significant losses and reduced mechanical breakdown strength. Nonetheless, a significant amount of inorganic fillers (exceeding 50 vol%) is necessary to achieve the desired high dielectric properties, which can result in a major decrease in breakdown strength, a rapid increase in loss, and a considerable decline in mechanical properties [170]. Interestingly, no report up to our best knowledge has been published yet which explored the dielectric characteristics of PVDF nanocomposite films reinforced with Ta_2O_5 nanofillers. Although, Ta_2O_5 can be a potential filler due to its excellent dielectric properties, thermal stability, chemical

inertness and greater polarizability [172]. Specifically, Ta_2O_5 has a relatively high dielectric constant (~25) and wide bandgap (~4.4 eV), which may contribute to improved charge storage capacity when incorporated into a polymer matrix such as PVDF [129]. Additionally, Ta_2O_5 has the ability to induce the favourable β-phase crystallization in PVDF which impacts its dielectric properties significantly. These characteristics make it a highly suitable candidate for enhancing the performance of polymer-based nanocomposites used in energy storage applications. In conclusion, the primary motivation for the practical implementation of these composites lies in the simultaneous improvement of mechanical breakdown strength and permittivity.

In our work we have demonstrated the preparation of PVDF nanocomposites reinforced with different weight ratios (significantly low amount) of Ta_2O_5 NPs as fillers, using a simple solution casting technique. Through impedance spectroscopy, the dielectric behavior of the films has also been analysed over a wide frequency (20 Hz–10 MHz) and temperature (30–120°C) range. Notably, the results highlight a substantial enhancement in dielectric permittivity, particularly at 1.25 wt% Ta_2O_5, with a dielectric constant nearly seven times higher than that of pure PVDF. This improvement is attributed to the superior dielectric characteristics of Ta_2O_5, enhanced β-phase crystallization, and interfacial polarization effects. Further, Universal Tensile Machine (UTM) has been used to measure the mechanical strength and elasticity of the nanocomposite thin films. It has been seen that the low amount of Ta_2O_5 has significantly improved the tensile strength of PVDF film upto ~21 MPa, which shows its low filler loading efficiency. These findings underscore the potential of Ta_2O_5 reinforced PVDF nanocomposites for the development of advanced materials tailored for high-performance flexible electronics and energy storage systems.

4.2 Experimental Section

4.2.1 Synthesis of Ta_2O_5 Nanoparticles

1.8 gm of $TaCl_5$ powder was dispersed in 40 ml ethanol and stirred for 30 min. Subsequently, 20 ml of deionised water was added dropwise, followed by continued stirring for additional 30 min. To balance the pH level of the solution, NH_4OH was added dropwise till the pH of the solution reached 9-10. The whole solution was transferred to 100 ml Teflon-lined autoclave and heated at 200 ^{0}C for 24 h. After natural cooling of the hydrothermal reactor, suspension was filtered and washed several times with deionized water using centrifugation process. The resulting precipitate was collected and dried at 80 ^{0}C overnight in a vacuum oven. The schematic diagram of the synthesis process of Ta_2O_5 nanoparticles has been shown in Figure 4.1.

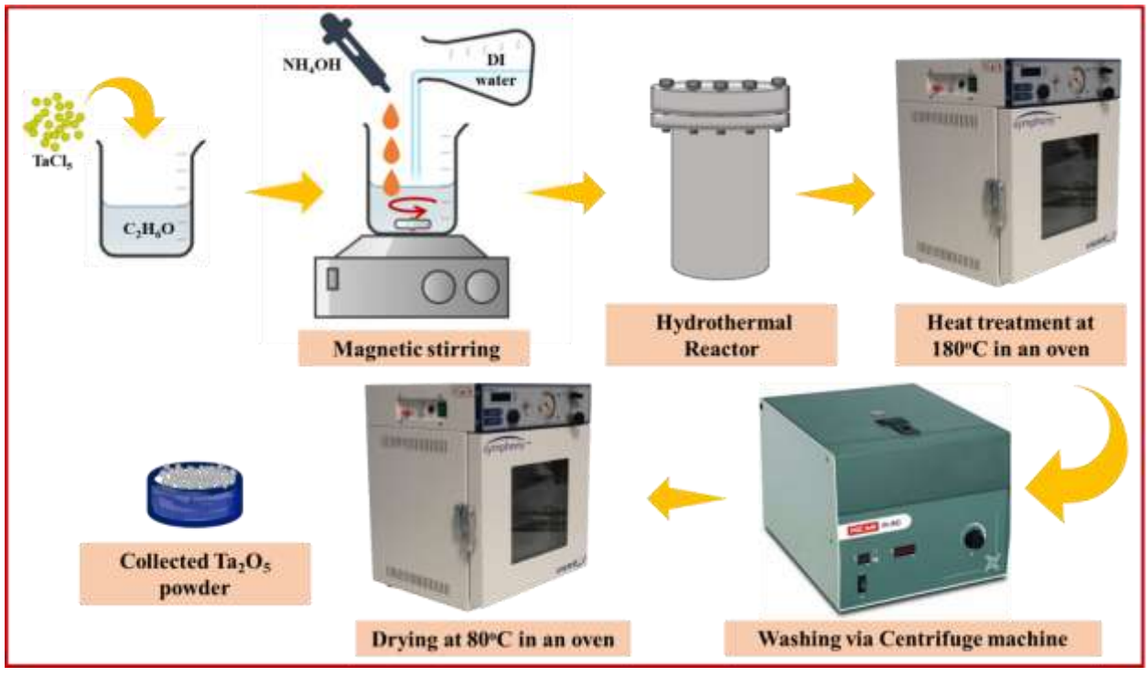

Figure 4.1 The schematic diagram to synthesize Ta_2O_5 nanoparticles via hydrothermal method

4.2.2 Preparation of Nanocomposite Thin Films

The Ta_2O_5@PVDF nanocomposite films with different weight ratios of nanofiller were synthesized using a facile solution casting technique. 1 g of PVDF was dissolved in 15 ml of N, N-dimethylformamide (DMF) and stirred on a magnetic stirrer until it formed a transparent homogeneous solution. The prepared Ta_2O_5 was dissolved in 2-3 ml of DMF according to the desired ratios (0%, 0.625%, 1.25%, 2.5% and 5 wt%) and ultrasonicated for 30 min. Ta_2O_5 solution was then slowly incorporated into the prepared PVDF solution and stirred vigorously for 2 hours to create a uniform gel-like solution with no bubbles. The resultant solutions were transferred to a clean glass petri dish and placed in a vacuum oven for drying. Finally, we obtained flexible Ta_2O_5@PVDF nanocomposite thin films with approx. thickness of 140-150 μm. A schematic diagram for the preparation of nanocomposite thin films is shown in Figure 4.2. The synthesized thin films with different filler concentration (0%, 0.625%, 1.25%, 2.5%, 5%) are named as TaP0 (pure PVDF), TaP1, TaP2, TaP3, TaP4.

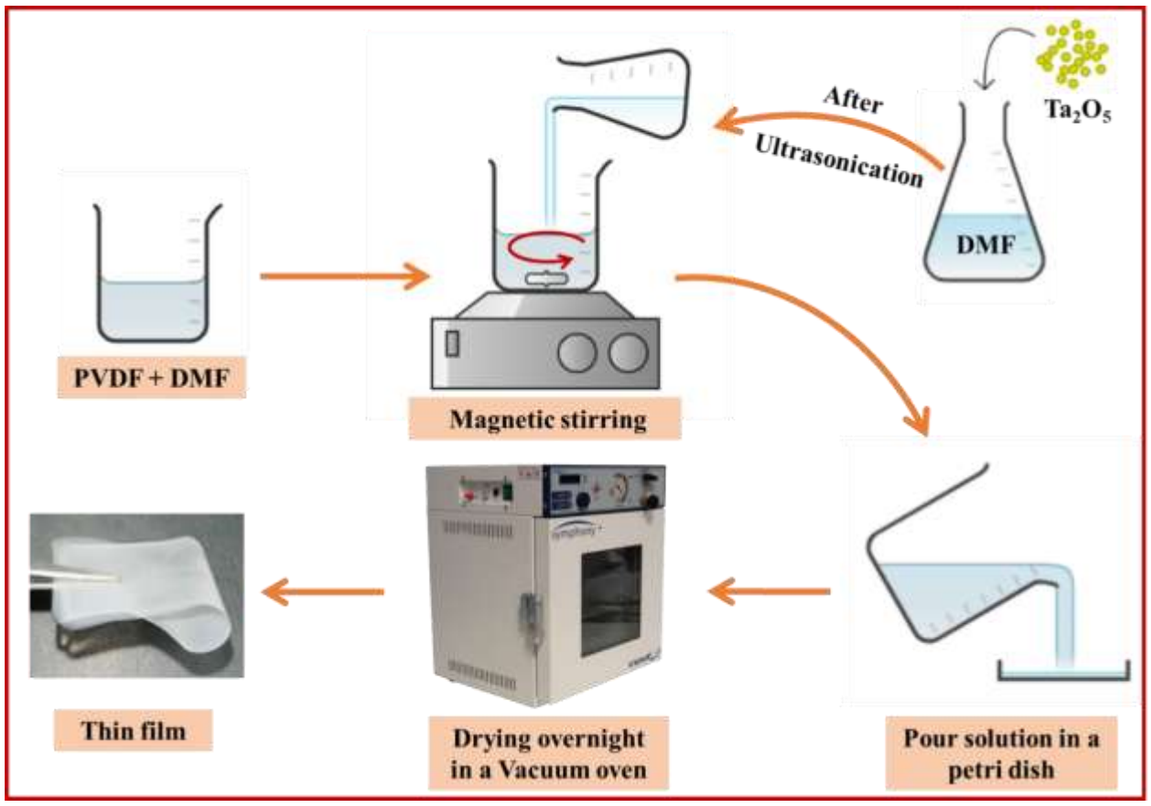

Figure 4.2 Schematic representation for the preparation of the PVDF based nanocomposite thin films

4.2.3 Characterizations

The prepared Ta_2O_5@PVDF nanocomposite thin films were characterized using Bruker D8 Advance X-ray diffractometer using X-ray source of Cu Kα (1.54 Å) to confirm the successful synthesis of the films. WiTec alpha 300 RA used to carry out Raman spectroscopy with a 532 nm laser source to check the molecular bonding between fillers and the PVDF. Transmission electron microscope (TEM) and Field emission scanning electron microscope (FESEM) were used to review the morphology of the nanofillers and synthesised films, respectively.

Further, impedance spectroscopy with in a wide frequency (20 Hz – 10 MHz) and operating temperature (30-120^{0}C) range using a Hioki LCR meter (Model IM3536) and a PID temperature controller (Model 234). And, the mechanical properties of the thin films were measured using a Universal tensile machine (UTM).

4.3 Results and Discussion

4.3.1 X-Ray Diffraction (XRD)

To identify the distinct crystalline phases of PVDF in the nanocomposite thin films, XRD measurements were carried out. The obtained XRD patterns of the pristine PVDF, prepared Ta_2O_5 NPs and Ta_2O_5@PVDF nanocomposites with different weight percentages of Ta_2O_5 are shown in

Figure 4.3, where, the PVDF peaks are indicated by '*', whereas Ta_2O_5 peaks are represented by a filled circle. The diffraction peak of pristine PVDF at 18.3^0 and 20.2^0 corresponds to the non-polar α-phase ((020) plane) and purely β-phase ((110)/ (200) planes), respectively [173–175]. Further, the diffraction peaks of Ta_2O_5 are attributed to its orthorhombic phase and are consistent with the standard JCPDS data (file no.: 25-0922) [89,176,177].

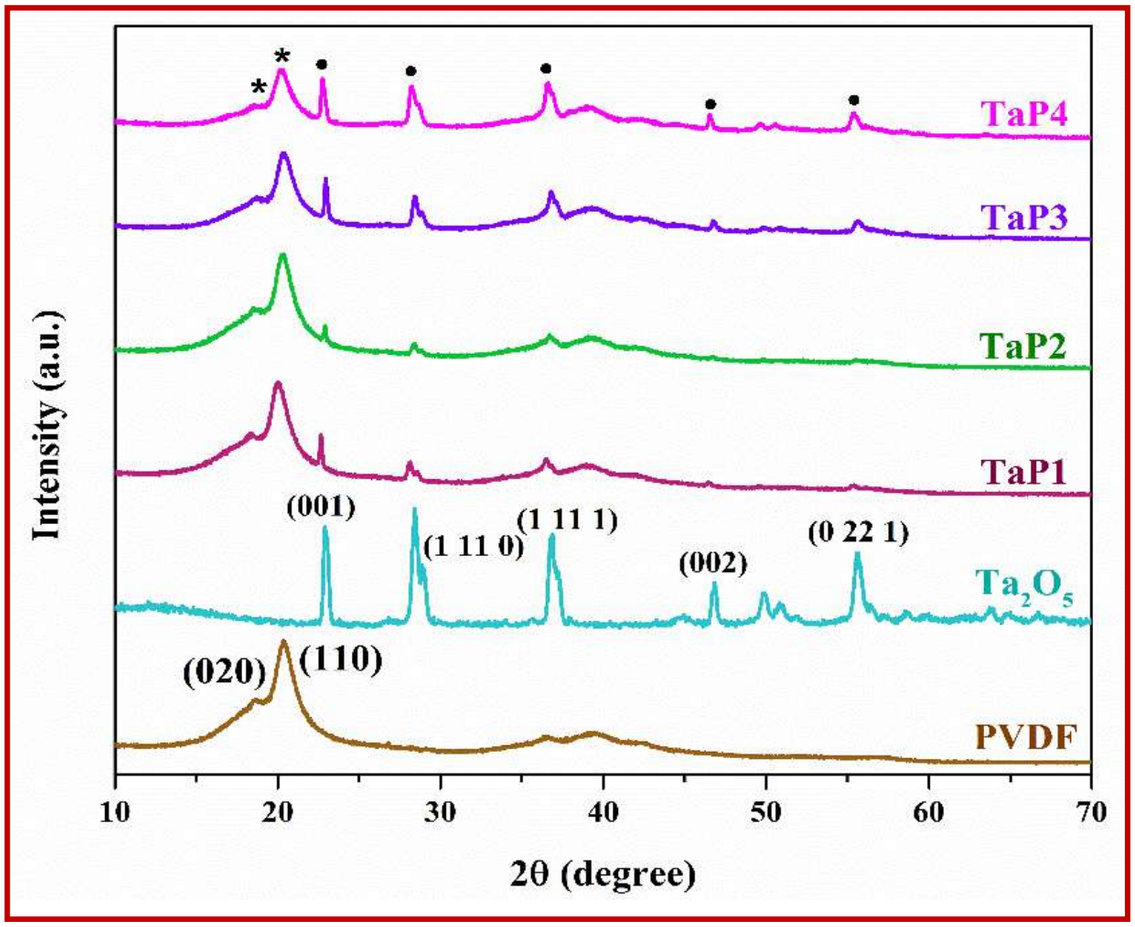

Figure 4.3 X-Ray Diffraction pattern for pristine PVDF, Ta_2O_5 NPs and nanocomposite thin films with different wt% of Ta_2O_5 NPs where * and • represent peaks for PVDF and Ta_2O_5, respectively

It can be observed that the addition of the Ta_2O_5 as a filler in PVDF films has increased the electroactive β-phase significantly. As the intensity of the diffraction peak of the α-phase decreases and the peak corresponding to the β-phase remains relatively stable or becomes more prominent in comparison, along with the increasing concentration of Ta_2O_5 NPs. Furthermore, the intensity of diffraction peaks of Ta_2O_5 increases in the nanocomposite films with a higher percentage of filler. This rise in intensity is certainly due to the crystalline structure of Ta_2O_5 NPs being more dominant than the semi-crystalline structure of PVDF and also due to the higher amount of Ta_2O_5

NPs [168]. Hence, the diffraction patterns of the nanocomposite films show a successful incorporation of Ta_2O_5 in PVDF matrix with enhanced β-phase.

4.3.2 Fourier Transform Infrared Spectroscopy (FTIR)

To further investigate the β-phase of PVDF, Fourier Transform Infrared Spectroscopy were used. The Figure 4.4 shows FTIR transmission spectra of pure PVDF and Ta_2O_5@PVDF nanocomposite thin films. The peaks of α-phase PVDF are well defined at 490, 612, 763, 875 1148 and 1220 cm^{-1} wavenumbers. The transmission bands at 510, 840 and 1280 cm^{-1} are the attributes of β-phase which is responsible for the good dielectric and piezoelectric properties of the thin films. The peaks at 840 and 1280 cm^{-1} corresponds to CH_2 rocking vibrations and CF_2 symmetrical stretching vibrations corresponding to the β-phase in PVDF [168,170,178]. The FTIR spectra of Ta_2O_5@PVDF nanocomposite films clearly displayed the characteristic of coexistence of both α and β-phases of PVDF.

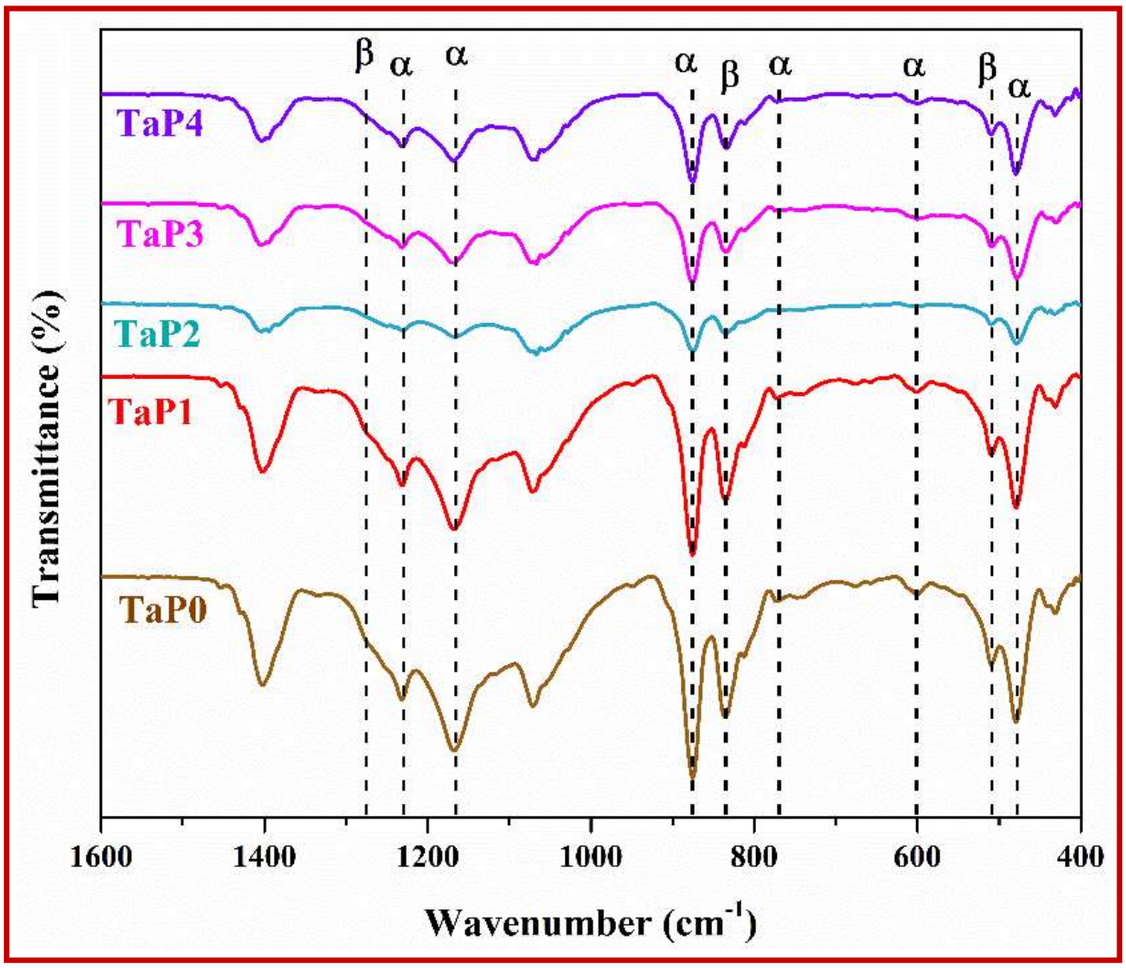

Figure 4.4 FTIR spectra for pristine PVDF and nanocomposite thin films with different wt% of Ta_2O_5 NPs

When PVDF is doped with varying concentrations of Ta_2O_5 NPs, the position of the transmission peaks remains unchanged and intensity of bands decreases along with the increase in the concentration of the filler because of the reducing PVDF, as confirmed by the XRD intensity patterns also [168].

4.3.3 Morphological Study

To study the morphology of nanofiller i.e. Ta_2O_5, Transmission Electron Microscope (TEM) has been used. The TEM image of Ta_2O_5 and its corresponding fringe pattern is shown in Figure 4.5. It can be observed from Figure 4.5(a) that the nanofillers have spherical shaped nanoparticles and the interplanar distance (d) between its two successive parallel fringes is 0.26 nm which is correlated to (1 11 0) lattice plane of Ta_2O_5's orthorhombic phase [129,172].

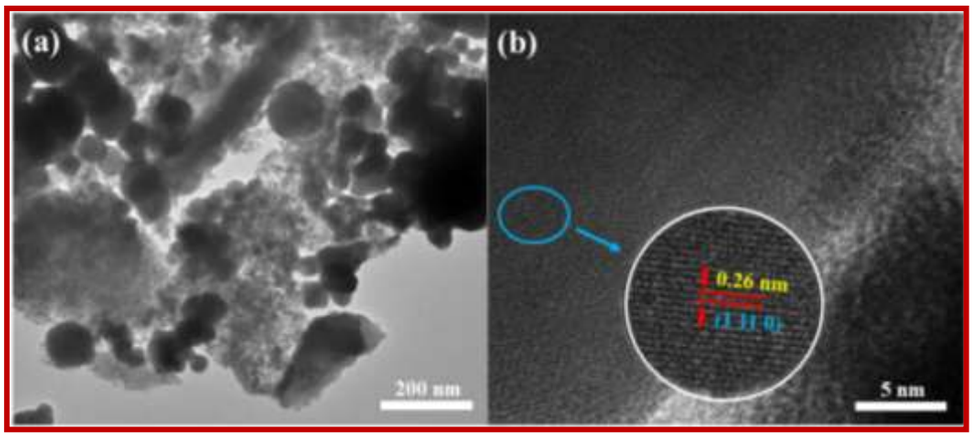

Figure 4.5 (a) TEM image and (b) fringe pattern of Ta_2O_5 NPs

Further, the synthesized thin films have also been examined for their surface morphology by Field-Emission Scanning Electron Microscope (FESEM). The FESEM micrographs are represented in Figure 4.6. The images display presence of randomly distributed spherulites with firm edges along with certain pores in pristine PVDF thin film. As the concentration of nanofillers increases, the number of pores reduces and spherulites' size increases. At an optimized concentration (1.25 wt%) the film demonstrated uniform smooth surface with nearly no pores [170]. The tiny white particles or dots on the spherulite structure in FESEM images of the thin films corresponds to Ta_2O_5 nanofillers integrated into the polymer matrix. Further, it can be observed from the Figure 5(d & e) that on higher filler concentrations (2.5 & 5 wt%) the films consist of spherulites similar to pristine PVDF but with diffused edges. That might be due to aggregation of the Ta_2O_5 NPs at higher concentration (shown with dotted circles) which restrict further incorporation of the nanofiller into polymer matrix thus leading to non-uniform surface [168].

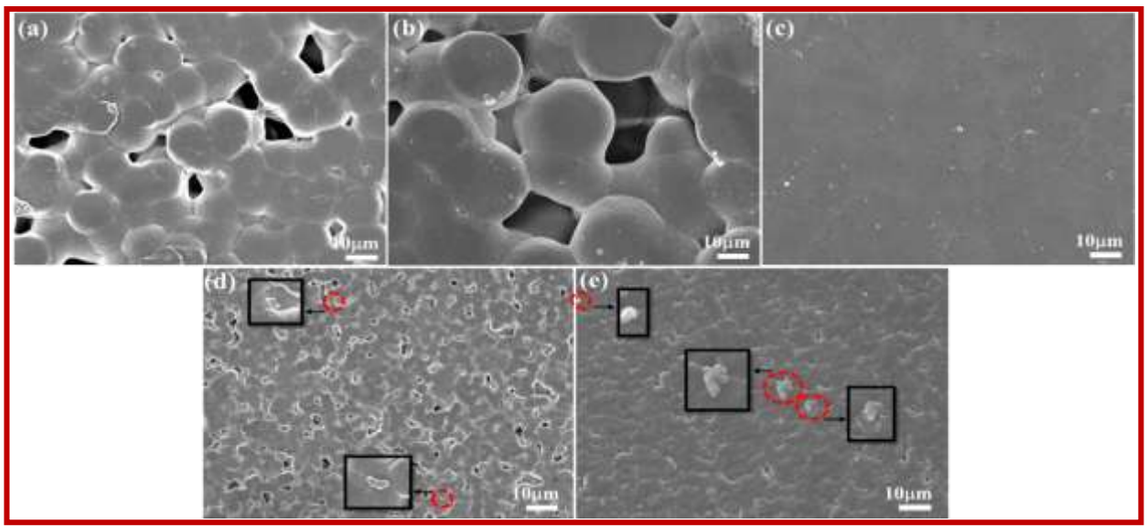

Figure 4.6 FESEM images of the PVDF films with wt% (a) 0%, (b) 0.625%, (c) 1.25%, (d) 2.5% and (e) 5% of Ta_2O_5 NPs

Additionally, Energy Dispersive X-Ray Spectroscopy (EDS) has been used to check the composition of the elements in the Ta_2O_5@PVDF nanocomposite thin films. The EDS graphs, shown in Figure 4.7, represent the weight % of elements: carbon (C), fluorine (F) (correspond to PVDF molecular structure, i.e. $(C_2H_2F_2)_n$) tantalum (Ta) and oxygen (O). Figure 6(a) contain peaks for only C and F that shows purity of the PVDF film. The thin films with nanofillers (Figure 4.7 (b-e)) reveal the trace of Ta and O elements that indicates the successful dispersion of Ta_2O_5 fillers in the polymer matrix. The increment in weight percentage of Ta and O elements along with the increasing concentration of Ta_2O_5 filler is also distinctly visible in the polymer films.

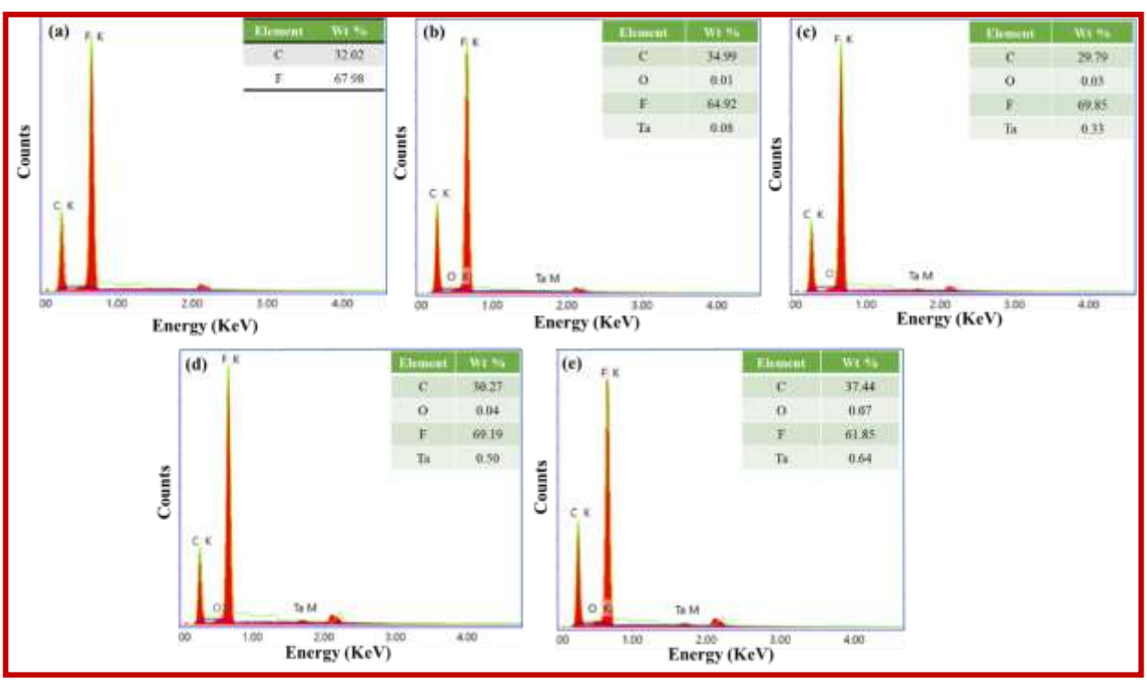

Figure 4.7 EDS graph of the PVDF films with wt% (a) 0%, (b) 0.625%, (c) 1.25%, (d) 2.5% and (e) 5% of Ta_2O_5 NPs

4.3.4 Mechanical Properties of the Prepared Films

In order to study the mechanical properties of the prepared nanocomposite thin films, rectangular-shaped films of dimensions 70 mm x 20 mm were cut. The stress-strain curve and tensile strength of the Ta_2O_5@PVDF nanocomposite thin films with different filler concentration are exhibited in Figure 4.8. Figure 4.8(a) clearly shows that tensile strength of the thin films increases as the concentration of Ta_2O_5 NPs increases upto 1.25 wt% and for beyond concentrations, tensile strength of films decreases but that is still greater than the pure PVDF. The obtained tensile strength is maximum for TaP2 i.e. ~21 MPa and thereafter decreases to ~13 MPa for TaP4. This decrement in the tensile strength can be due to the agglomeration of the nanoparticles in the polymer matrix [159]. Furthermore, the initial region of the stress-strain plots has been used to determine the Young's modulus as a function of nanofiller concentration [179,180]. The Young's modulus of the films increases along with the addition of nanofiller content as seen in the Figure 4.8(b). The enhanced stiffness in the films may be due to the improved interfacial interaction or adhesion between Ta_2O_5 and the PVDF matrix [181]. Ta_2O_5 being a rigid filler, its particles act as stress transfer points under mechanical loading, leading to improved load-bearing capacity [182]. This suggests that tensile elasticity of the prepared thin films is indirectly proportional to the concentration of the Ta_2O_5 NPs in the evaluated range. Additionally, Ta_2O_5 nanofillers reduces the free volume within the polymer matrix, further limiting the mobility of PVDF chains, hence improving the mechanical performance of nanocomposite thin films [179,183,184]. TaP4 (5 wt%) exhibits the highest Young's modulus (~9.3 MPa) which is around 9 times higher than that of the pure PVDF. These results indicate that the Ta_2O_5 NPs reinforcement can improve the mechanical performance of the PVDF polymer efficiently, which is very vital to the flexible electric materials.

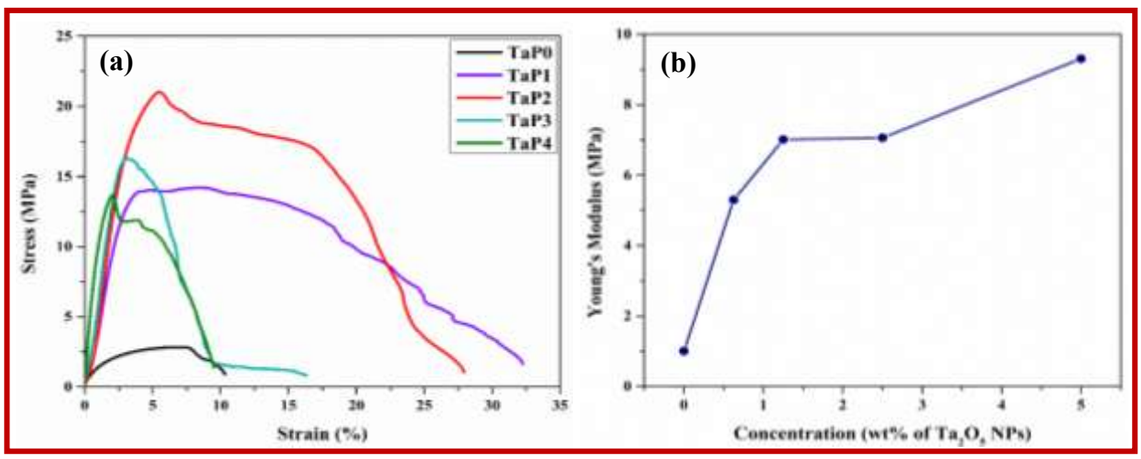

Figure 4.8 (a) Stress-Strain curves and (b) variation in Young's Modulus with Ta_2O_5 NPs concentration for pure PVDF and Ta_2O_5@PVDF nanocomposite thin films

4.3.5 Dielectric Studies of the Films

The dielectric properties of pristine PVDF and Ta_2O_5@PVDF nanocomposite thin films were inspected as a function of operating temperature, applied field frequency and Ta_2O_5 NPs wt% concentration. The equation 1 defines a system's complex dielectric permittivity, with the real ($\varepsilon'(\omega)$) and imaginary ($\varepsilon''(\omega)$) components denoting the dielectric constant and dielectric loss, respectively. The dielectric constant (ε') and dielectric loss (ε'') are of particular significance for understanding the polarization, conduction and relaxation mechanism, dipoles' orientations, charge movements and energy dissipation etc. within the material and they are calculated using equation 2 and 3, respectively [115].

$$\varepsilon^*(\omega) = \varepsilon'(\omega) - i\varepsilon''(\omega) \quad (1)$$

$$\varepsilon'(\omega) = \frac{Cpd}{\varepsilon oA} \quad (2)$$

$$\varepsilon''(\omega) = \varepsilon'(\omega) \tan \delta \quad (3)$$

Where, ω ($2\pi\nu$) is the angular frequency of the applied electric field, C_p is the measured parallel plate capacitance, d is the thickness and A is the cross-section area of the dielectric material, ε_o is permittivity of free space, tan δ is the loss tangent, δ = (90-θ), and θ is the phase difference between the applied alternating voltage to the measured current.

The operating temperature dependence (30-120^{0}C) of the dielectric constant for the pristine PVDF and Ta_2O_5@PVDF nanocomposite thin films at different applied field frequencies ranging from 100 Hz to 10 MHz is shown in Figure 4.9. The curves for every concentration follow the same pattern where dielectric constant of the thin films increases along with the operating temperature. Dielectric behaviour of a material is mainly related to the ability of its molecular dipoles to oscillate in an alternating field. As the temperature rises, thermal oscillations get stronger and dipoles can follow the alternating field more readily [115,172,178]. Therefore, we can say that this increase in ε' with rising operating temperature is certainly due to the thermal agitation, which enhanced the orientational freedom of the polar sites in the PVDF polymeric chains according to the alternating field [185].

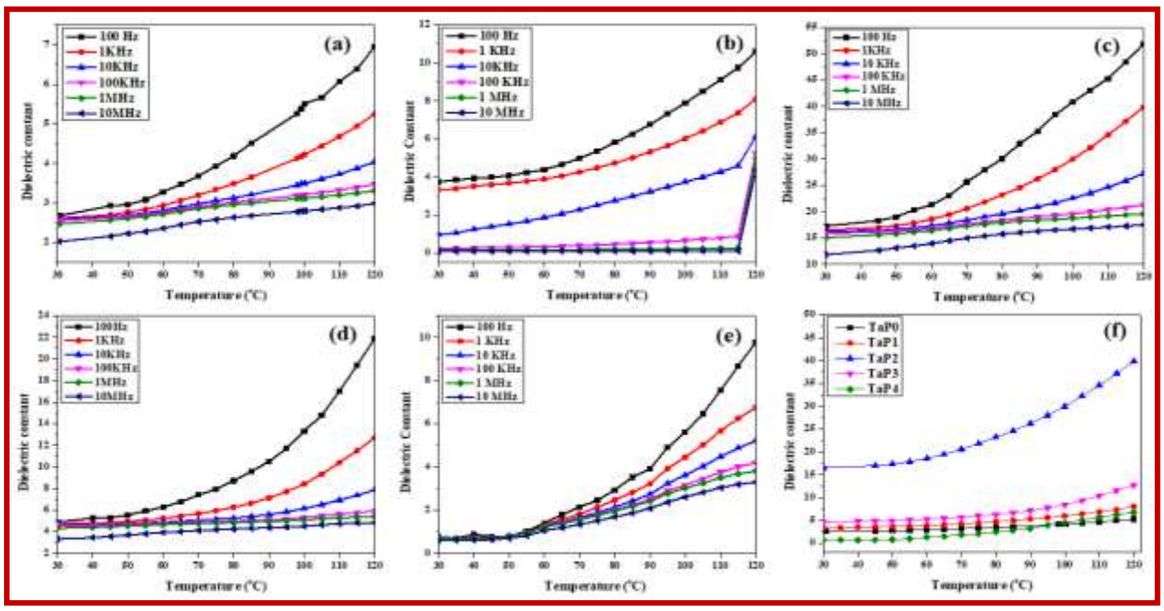

Figure 4.9 Dielectric constant curves w.r.t. temperature at different applied frequencies for the films with wt% (a) 0%, (b) 0.625%, (c) 1.25%, (d) 2.5%, (e) 5% of Ta_2O_5 NPs and (f) comparative graph of dielectric const. vs temperature at 1 KHz for different concentration of thin films

Similarly, dielectric loss is another important dielectric property in energy storage devices that tells us about the energy losses or heat dissipation [172]. It should be as low as possible in an ideal dielectric device. Dielectric loss within Ta_2O_5@PVDF nanocomposite thin films follows the same trend for the changing operating temperature. As the temperature increases from 30^0C to120^0C, loss tangent also increases that is evidently visible in the Figure 4.10. This increase in the dissipation factor signifies a greater amount of energy loss within the material. As discussed above, with rising temperature the dipoles are more readily responsive to the electric field, which results in a steady rise in tan δ indicating the initialization of the thermal deterioration at high temperatures [185].

The calculated ε′ values of pristine PVDF is ~2.6 at room temperature for the applied field frequency of 1 KHz. As the concentration of Ta_2O_5 NPs in the thin films reached to 1.25 wt% the dielectric constant increases to ~16.7 at room temperature and for higher operating temperature (120^0C), ε′ value increases to around 40. This rise in ε′ values is firstly attributed to the addition of Ta_2O_5 fillers in the polymeric matrix of PVDF as Ta_2O_5 has a great polarizability property that leads to an increase in the number of polarizable groups in the nanocomposite thin films [130,172].

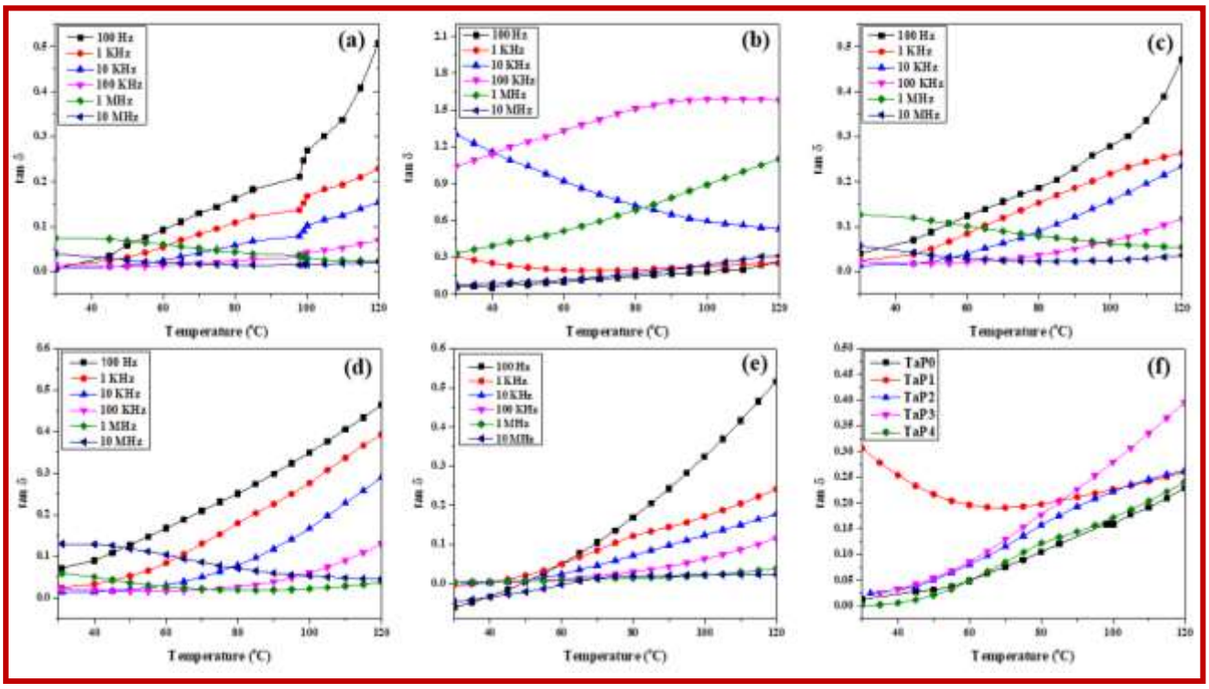

Figure 4.10 Loss tangent (tan δ) as a function of temperature at different applied frequencies for the films with wt% (a) 0%, (b) 0.625%, (c) 1.25%, (d) 2.5%, (e) 5% of Ta_2O_5 and (f) comparative graph of tan δ vs temperature at 1 KHz for different concentration of thin films

Moreover, as the filler concentration in PVDF-based thin films increases, the dispersion behaviour of the ε′ values shows that the interaction between Ta_2O_5 NPs and the polymer chain initially promotes parallel dipolar alignments in the functional groups of polymers repeated units. This phenomenon is known as Maxwell-Wagner Sillars (MWS) effect or interfacial polarization that generally occurs in the heterogeneous system composed of two or more dielectric materials [178,185]. Another phenomenon that widely exists in polymer composites including conducting or semiconducting additives, percolation threshold, is also the reason for the sudden rise in dielectric constant for TaP2 thin film [186,187]. Further, it is observed that for the higher concentrations (2.5 and 5wt%), the dielectric constant started to decrease. As the filler concentration increases, the conductive pathways may begin to form within the polymer matrix. Beyond a certain concentration or percolation threshold, too many filler particles may cluster together, forming larger agglomerates that can hinder the uniformity of the material [188,189]. As SEM images also confirm the agglomeration of the particles for the higher concentration of the

Ta_2O_5 in the PVDF matrix which reduces the number of filler-polymer interfaces that leads to less charge accumulation, hence diminished interfacial polarization. Overall, the optimized concentration of Ta_2O_5 filler boosted the number of polarizable functional groups and conductive pathways along with the amplified interfacial polarization in the PVDF based thin film. On the other hand, higher concentration of the filler elevated the particle agglomeration and weakened the interfacial polarization that degraded the dielectric properties of the thin films. However, the dielectric constant of the Ta_2O_5@PVDF nanocomposite thin films are better than the pure PVDF films even with the higher concentration of fillers.

Besides, it can be seen from Figure 4.10(f) that the loss tangent for the other filler concentrations is higher than that of pure PVDF thin film. The primary cause of the rise in dielectric loss is attributed to the enhancement of charge carriers in the system induced by the fillers. The observed loss tangent for the TaP2 thin film is between 0.024- 0.262 for the operating temperature range 30-120^{0}C at 1KHz frequency of applied electric field. Furthermore, as per the literature, the large leakage current at the percolation threshold is also responsible for the increase in dielectric loss [186,187]. All-inclusively, the tan δ remained in a low range along with a higher dielectric constant for the small amount of filler i.e, 1.25 wt% of Ta_2O_5 in the PVDF based thin films. The calculated ε′ and tan δ values for varying wt% concentrations of Ta_2O_5@PVDF nanocomposite thin films at 30 (RT) and 120^{0}C operating temperature for 1KHz field frequency is represented graphically in Figure 4.11. Additionally, a comparative analysis of the obtained results has been done with the reported data and tabulated in Table 4.1. The dielectric results obtained for TaP2 film show competent performance, along with enhanced mechanical properties at lower filler concentration.

The dependence of the dielectric constant of the pristine PVDF and Ta_2O_5@PVDF nanocomposite thin films on the applied field frequency (20 Hz – 10 MHz) at different operating temperatures are shown in Figure 4.12. The graphs exhibit the inverse relation between the ε′ and field frequency for all the investigated concentrations of the filler. At the low operating temperature, ε′ is almost independent of frequency, whereas for the higher operating temperature, ε′ spectra of the thin films show three different regions (I, II and III) of dispersion, as shown in Figure 4.12(a).

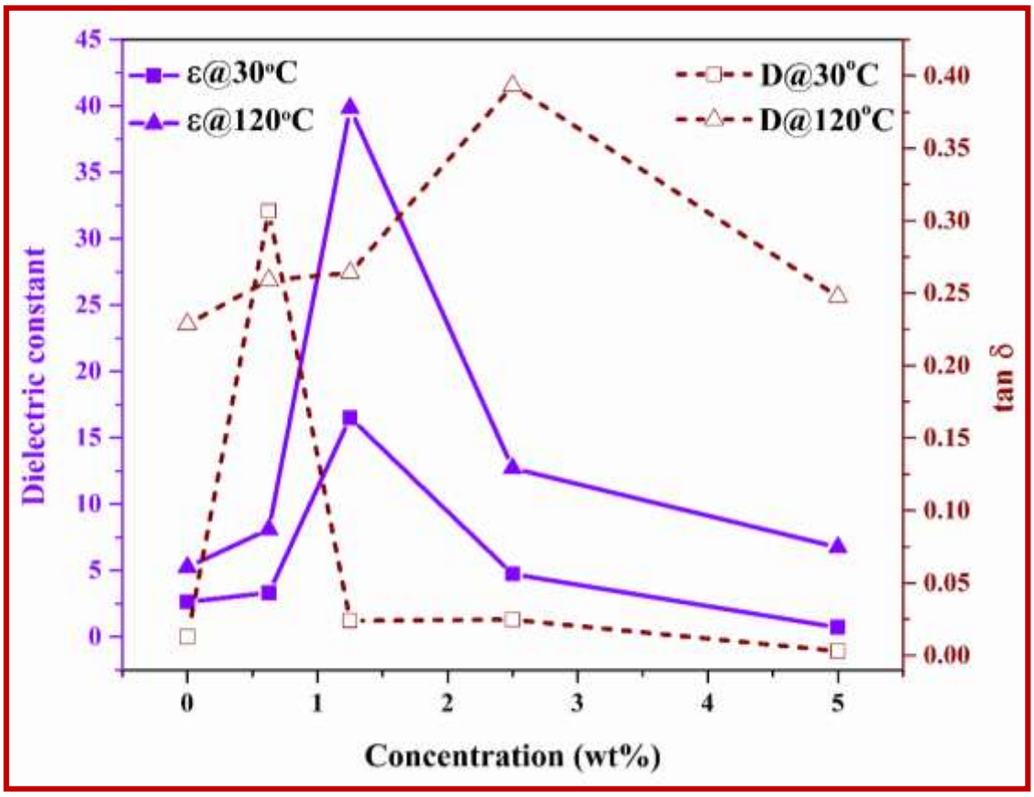

Figure 4.11 Comparative graph of dielectric constant and loss tangent for different filler concentrations at operating temperature 30 & 120°C and 1 KHz frequency of applied electric field

In (I), low frequency region (20 Hz-1 KHz), a high dispersion linear behaviour is observed. The higher values of ε′ in this region is mainly because of the polarization caused by dipoles that have enough time to align themselves with the direction of the applied electric field. This phenomenon is called interfacial polarization or Maxwell Wagner Sillars (MWS) effect [170,185]. MWS is predominantly occurring in thin films due to the free charge build up at the filler-polymer interfaces. Further, the apparent oscillations or irregularities seen in the dielectric constant curves in this region, can be attributed to the polarization instability. In the low-frequency regime, MWS effects are known to cause unstable dielectric response due to the delayed movement of charge carriers at the interfaces between polymer and nanofillers. Such polarization lag may appear as curve irregularities.

The intermediate (II) frequency region (1KHz-10KHz), shows the nonlinear dispersion behaviour that represents a weak polarization relaxation process within the nanocomposite thin films due to gradual vanishing of interfacial polarization. And, the dipole response becomes restricted and the dielectric constant tends to be saturated with a further increase in the frequency as clearly seen in

the (III) high frequency region (10KHz-10MHz) [185,186]. This steady behaviour is caused by the micro-capacitor structure, which states that the distribution of conductive nanofillers (Ta_2O_5) in the PVDF-insulated polymeric material forms numerous micro-capacitors, improving the dielectric characteristics of the whole nanocomposite [174]. Generally, the decrease of dielectric constant with increasing field frequency is because of the incapability of the charge carriers to follow and align in the electric field direction as time period is significantly shorter at higher frequencies [171].

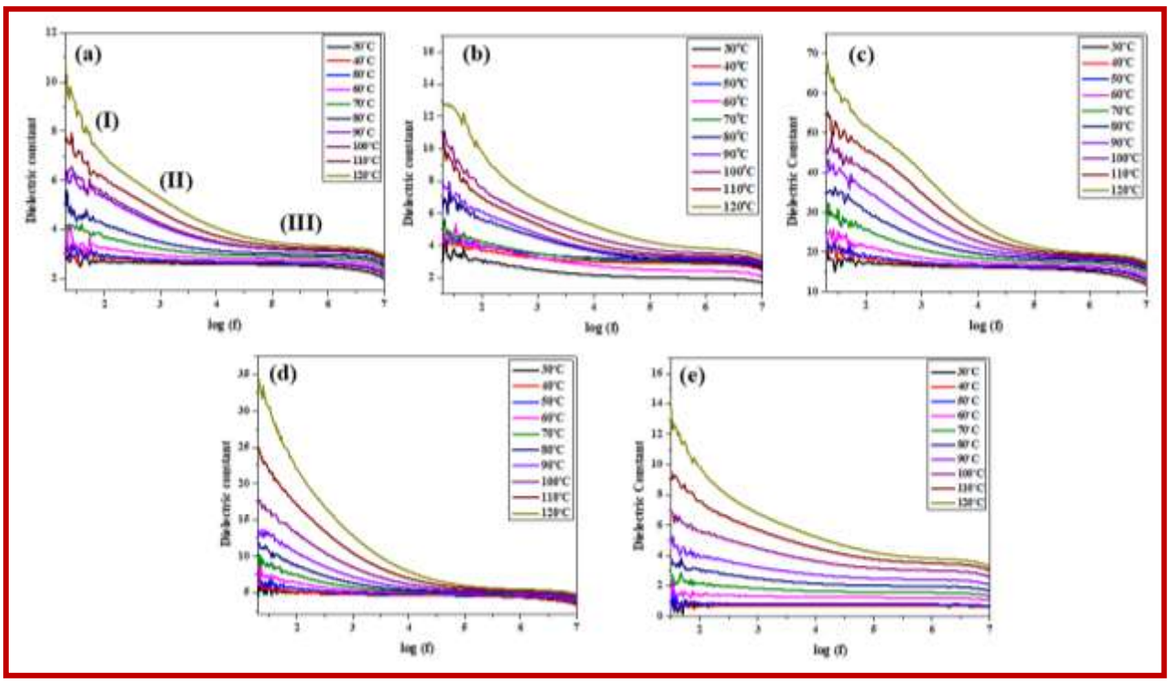

Figure 4.12 Dielectric constant as a function of log of applied frequency at different temperatures for the films with wt% (a) 0%, (b) 0.625%, (c) 1.25%, (d) 2.5% and (e) 5% of Ta_2O_5 NPs

Table 4.1 Comparative data of dielectric constant and loss tangent of different nanofillers in PVDF matrix at room temperature and 1 KHz applied field frequency.

S.No.	Filler	Morphology	Filler (wt%)	Dielectric Constant (ε′)	Loss Tangent (tan δ)	YoP [Ref.]
1.	SnO_2	Nanoparticles	0.05	12	0.6	2023 [169]
2.	MoS_2	Flakes	7	7	-	2023 [173]
3.	Dopamine treated SnO_2	Nanoparticles	1	6	-	2022 [188]
4.	FeO/ZnO	Deformed flower like appearance	1	15	0.1	2021 [175]
5.	Cd doped ZnO & Ca doped ZnO	Nanoparticles	10 & 10	14 & 15	0.75 & 0.9	2020 [170]
6.	$Li_4Ti_5O_{12}$	Nanoparticles	1 vol%	14	0.75	2020 [185]
7.	MgO	Nanoparticles	3	13.5	0.22	2019 [171]
8.	SnO_2	Nanosheets	10	15	0.15	2019 [157]
9.	Ta_2O_5	Nanoparticles	1.25	16.7	0.024	This work
10.	Ta_2O_5	Nanoparticles	1.25	40	0.262	This work at 120^0C

4.4 Conclusion

In the present work, we have prepared Ta_2O_5@PVDF nanocomposite thin films using a solution casting method with different weight % of Ta_2O_5 NPs as nanofillers. The dielectric results evince that the value of ε′ increases along with concentration of filler upto 1.25 wt% (TaP2) in the thin films and for the higher concentrations, ε′ values decreases but still more than that of pure PVDF film. The ε′ of TaP2 was found to be around 7 times higher than that of pure PVDF film because of the addition of Ta_2O_5 nanofillers, magnified orientation and interfacial polarization. Besides, mechanical properties of the films divulge the enhanced tensile strength and upgraded elasticity with the addition of Ta_2O_5 NPs. Overall, the incorporation of nanofillers (1.25 wt%) with optimized low concentrations in the PVDF based thin films helped in retaining a higher degree of crystallinity and increased dielectric constant (~40 at 120^{o}C & 1 KHz), magnified tensile strength (~21 MPa) with low dissipation loss (~0.024) without affecting the molecular chain of PVDF film which is much better than the reported data of other inorganic fillers. As a result, the present study suggests that flexible Ta_2O_5@PVDF nanocomposite thin films can be an efficient material for wearable electronic devices, lithium-polymer batteries etc.

CHAPTER 5

Study of MXene@Ta_2O_5 Heterostructure as Nanofiller in the PVDF Matrix & its Effect on PVDF's Dielectric and Mechanical Properties

Herein, we synthesized a novel MXene@Ta_2O_5 heterostructure through simple hydrothermal method. The synthesized heterostructure was characterized using X-ray diffraction and Photoelectron Spectroscopy for the identification of their crystalline phases and oxidation states, respectively. Further, MXene@Ta_2O_5 were incorporated into PVDF matrix with different concentrations (0, 0.625, 1.25, 2.5 and 5 wt%) as nanofillers to prepare the flexible films via drop casting method. The dielectric behaviour of the prepared nanocomposite films as a function of frequency (20Hz – 10 MHz) and temperature (30-120^{0}C) has been studied through impedance spectroscopy. The PVDF film reinforced with MXene@Ta_2O_5 at the optimal 1.25 wt% concentration possesses a dielectric constant of ~10 at 120^{0}C respectively, which is much higher than that of pure PVDF, along with relatively low (<0.15) dielectric loss. This enhanced dielectric properties is ascribed to the addition of MXene@Ta_2O_5 heterostructure as nanofillers in the PVDF matrix where negatively terminated (–F, –OH, –O) surfaces of MXenes strongly interact with PVDF CH_2 – CF_2 dipoles and multiple interfacial interactions that intensified the net polarization. Further, mechanical study of nanocomposite films suggests that addition of MXene@Ta_2O_5 nanofiller in PVDF maintains the tensile strength (~26.7 MPa) and elasticity with Young's modulus of ~8.6 MPa. The improved dielectric properties along with maintained mechanical integrity enable these nanocomposite thin films to meet the requirements of present demand of the flexible electronic, energy harvesting and storage devices.

5.1 Introduction

The rapid evolution of flexible electronics, advanced energy storage systems, and next-generation wearable technologies has driven a massive demand for lightweight, bendable, and high-performance dielectric materials []. Among the various available materials, polyvinylidene fluoride (PVDF) has emerged as a premier polymer matrix, primarily due to its exceptional mechanical resilience, inherent flexibility, and strong ferroelectric characteristics []. Structurally, PVDF crystallizes into several distinct polymorphs, notably the α, β, and γ-phases. Among which β-phase is the polar phase characterized by its all-trans molecular chain conformation. β-phase is particularly crucial as it dictates the polymer's overall dielectric, piezoelectric, and ferroelectric responses [11,12].

Beyond PVDF's electromechanical advantages, it exhibits outstanding chemical inertness, providing robust resistance against a wide array of corrosive agents including organic solvents, aromatic hydrocarbons, and inorganic acids [13]. Furthermore, it demonstrates remarkable durability against harsh environmental factors such as ultraviolet (UV) radiation and extreme weathering that makes it highly reliable for the storage and transportation of high-purity chemicals [13,14]. Despite these profound advantages, pristine PVDF suffers from inherent electrical drawbacks. It has a relatively low dielectric constant and suboptimal energy dissipation capabilities []. These intrinsic limitations significantly hinder its direct application in high-efficiency energy storage and advanced flexible electronic systems. Hence, necessitating further structural and chemical optimization.

Consequently, a critical strategy employed by the researchers to overcome these performance restrictions has been the incorporation of different nanofillers into the polymer matrix such as ceramic materials with good dielectric properties (ZnO, $BaTiO_3$, SnO_2 etc.) [56,160,190]. However, a large concentration of these materials is required to improve the dielectric properties of the films that leads to agglomeration, brittleness, formation of localised electric field and reduction in the mechanical properties of the PVDF films [73,86,191]. Similarly, the conducting fillers such as CNTs, MXenes, rGO etc. has been also used as nanofillers [191,192]. Even the low amount of these conducting fillers increases the polarization in the nanocomposite films efficiently. But on the other hand, they are tend to form conducting

pathways and produce relatively larger dielectric losses that increases the leakage current and reduces the breakdown strength of the film [73].

Hence, to prepare a flexible material with enhanced polarization and less losses, incorporation of the combination of ceramic and conducting fillers in the polymer matrix is one of the best ways. Like as, H.Q. Wang et al. designed a polymer dielectric nanocomposite with significantly improved energy storage density by using a MoS_2@MXene core-shell heterostructure as a hybrid filler in a PVDF matrix. They reported strong interfacial polarization induced by MXene and MoS_2 layer enhanced the breakdown strength of the film and reduced dielectric loss by hindering direct MXene-MXene contact, which suppressed leakage current [73]. Similarly, Lu Yang et al. constructed PVDF based flexible force sensor with MXene@MnO_2 heterostructure reinforcement. They demonstrated that the synergistic effect of microarrays patterning and MXene@MnO_2 nano-reinforcements boosted the piezo-activity of PVDF efficiently. They also reported MXene@MnO_2 incorporation strengthened the Young's modulus of the PVDF film upto 2.6 GPa [86].

In this context, the strategic combination of highly functional nanofillers within the PVDF matrix offers a clear pathway towards developing highly efficient flexible films. The reinforcement of these nanofillers in the PVDF matrix serve a dual purpose, (i) they enhance the overall dielectric permittivity (ε′), hence polarization in the matrix and (ii) induce the more polarized charge accumulation on the interfaces that promote the formation and stability of the desirable polar β-phase in PVDF [160,190,193].

19 Recently, MXenes, a family of two-dimensional (2D) transitional metal carbides, nitrides, and carbonitrides have emerged as excellent candidates due to their high electrical conductivity, robust electron-accepting nature, and large surface area making them ideal for charge density and interfacial polarization effects [96,191,194]. However, their tendency to restack and the inherent complexity of their surface chemistry can sometimes limit their effectiveness [73,96]. On the other hand, Ta_2O_5 is also a potential filler due to its high dielectric constant, thermal stability and greater polarizability [138,172]. Additionally, Ta_2O_5 has the ability to induce the favourable β-phase crystallization as it increases the polarisable groups in PVDF significantly [195].

Therefore, in this work, we report the synthesis and characterization of a novel MXene@Ta_2O_5 heterostructure using a simple hydrothermal method. We then fabricated flexible MXene@Ta_2O_5/PVDF nanocomposite films with varying concentrations of the synthesised

MXene@Ta_2O_5 nanofillers. Further, dielectric and mechanical properties of the prepared nanocomposite films have been studied via impedance spectroscopy and universal tensile machine, respectively. The optimal concentration was determined to be 1.25 wt% at which the prepared nanocomposite film exhibited the highest dielectric constant while maintaining the mechanical flexibility. Our collective findings establish the MXene@Ta_2O_5 reinforced PVDF film is the highly promising and scalable material for developing flexible films towards high-performance flexible electronics and energy storage systems.

5.2 Experimental Section

MAX phase of Titanium Aluminium Carbide (Ti_3AlC_2) was purchased from Sigma-Aldrich with purity ≥90%. Tantalum pentachloride ($TaCl_5$ - 99.5%) and polyvinylidene fluoride (PVDF) of high purity were purchased from Thermofisher Scientific and $NaBF_4$ from CDH. All the reagents were used without any further purification.

5.2.1 Preparation of Ta_2O_5 Nanoparticles

1.8 gm of $TaCl_5$ powder was dispersed in 40 ml ethanol and stirred for 30 min. Subsequently, 20 ml of deionised water was added dropwise, followed by continued stirring for additional 30 min. To balance the pH level of the solution, NH_4OH was added dropwise till the pH of the solution reached 9-10. The whole solution was transferred to 100 ml Teflon-lined autoclave and heated at 200 ^{0}C for 24 h. After natural cooling of the hydrothermal reactor, suspension was filtered and washed several times with deionized water using centrifugation process. The resulting precipitate was collected and dried at 80 ^{0}C overnight in a vacuum oven. The schematic diagram of the synthesis process of Ta_2O_5 nanoparticles has been shown in Figure 5.1 (a) and the chemical reactions involved in the process has been represented by equations 5.1 - 5.4.

$$TaCl_5 + 5C_2H_5OH \rightarrow Ta(OC_2H_5)_5 + 5HCl \quad (5.1)$$

$$Ta(OC_2H_5)_5 + H_2O \rightarrow Ta(OH)_5 + 5C_2H_5OH \quad (5.2)$$

$$HCl + NH_4OH \rightarrow NH_4Cl + H_2O \quad (5.3)$$

$$2Ta(OH)_5 \rightarrow Ta_2O_5 + 5H_2O \quad (5.4)$$

5.2.2 Hydrothermal Preparation of MXenes

To prepare the MXene, 3 gm of $NaBF_4$ was dissolved in 20 ml of 37 wt% HCl and then 1 gm of Ti_3AlC_2 was added and stirred to mix uniformly. The whole suspension was transferred to 100 ml Teflon-lined autoclave and treated to 180 ^{0}C for 16 h. After the natural cooling of hydrothermal reactor, suspension was filtered and washed several times with deionized water using centrifugation process. The resulting precipitate was collected and dried at 80 ^{0}C overnight in a vacuum oven. Figure 5.1 (b) represents the synthesis process of MXene nanosheets in schematic form. To understand the chemical bonding better, the chemical reaction involved in the synthesis process of MXene has been represented by equations 5.5 - 5.8 [77].

$$NaBF_4 + HCl + 3H_2O \rightarrow NaCl + H_3BO_3 + 4HF \quad (5.5)$$

$$Ti_3AlC_2 + 3HF \rightarrow Ti_3C_2 + AlF_3 + 1.5H_2 \quad (5.6)$$

$$Ti_3C_2 + 2H_2O \rightarrow Ti_3C_2(OH)_2 + H_2 \quad (5.7)$$

$$Ti_3C_2 + 2HF \rightarrow Ti_3C_2F_2 + H_2 \quad (5.8)$$

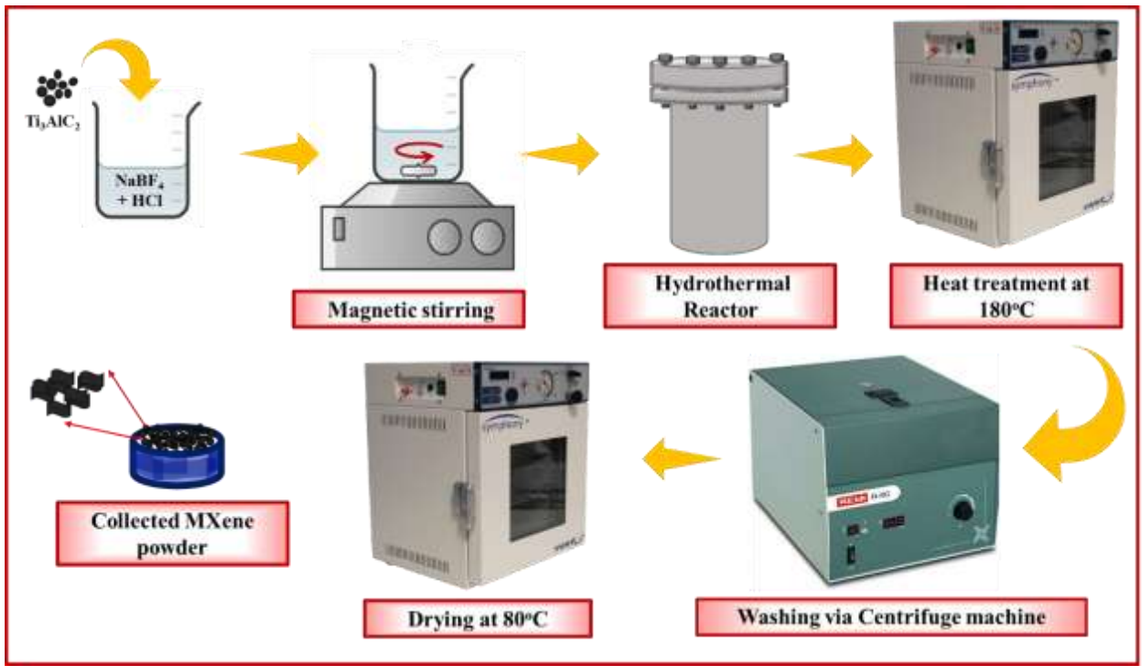

Figure 5.1 (a) The schematic diagram to synthesize Ta_2O_5 nanoparticles using hydrothermal method

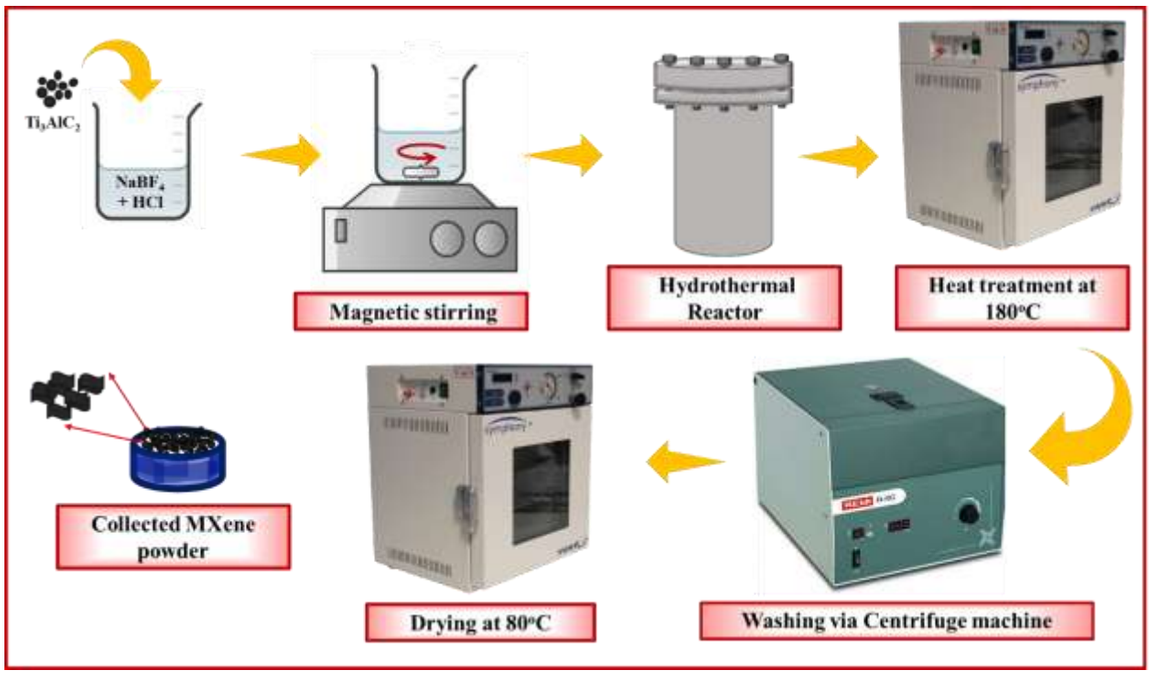

Figure 5.1 (b) The schematic representation for the synthesis of MXene nanosheets via hydrothermal method

5.2.3 Preparation of MXene@Ta_2O_5 Heterostructure

0.52 gm of the prepared Ta_2O_5 along with 0.13 gm MXene were mixed in 20 ml deionized water. The solution was mixed uniformly using a bath ultrasonicator for several hours. After that the product was washed with deionized water and ethanol multiple times. The collected precipitate was dried in a vacuum oven at 80 ^{0}C for 12 h. The preparation of MXene@Ta_2O_5 heterostructure has been provided in Figure 5.1 (c).

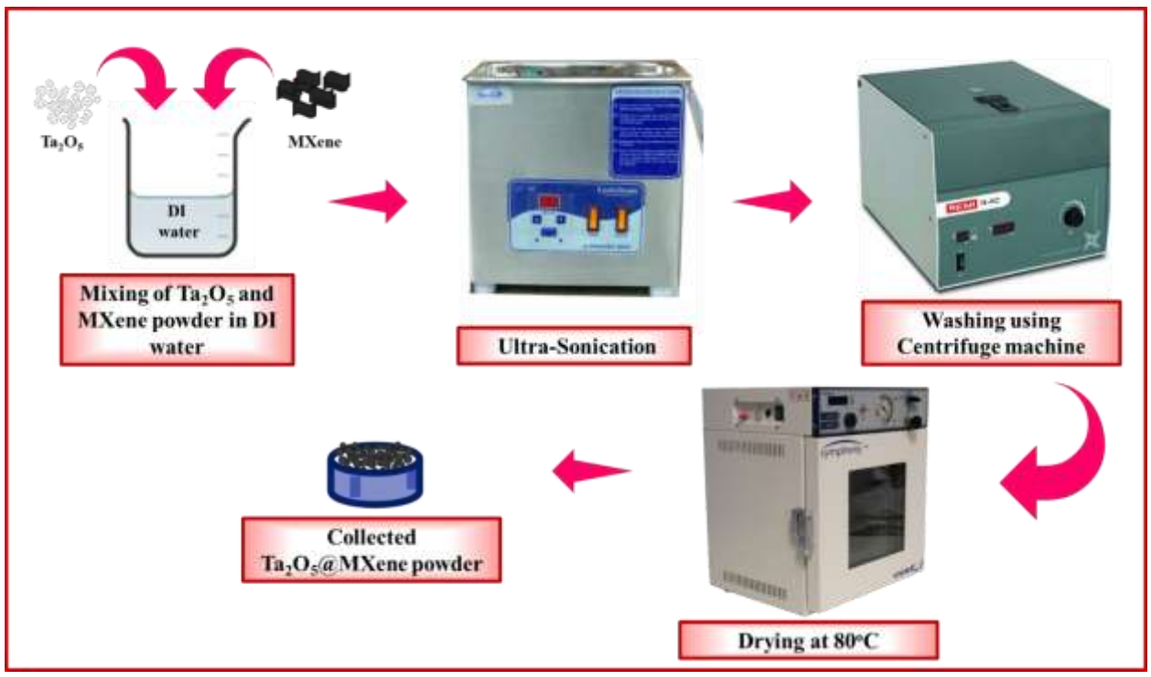

Figure 5.1 (c) The schematic representation for the preparation of MXene@Ta_2O_5 heterostructure

5.2.3 Preparation of Nanocomposite Thin Films

PVDF based flexible nanocomposite film with various concentration of MXene@Ta_2O_5 nanofiller (0 wt%, 0.625 wt%, 1.25 wt%, 2.5 wt% and 5 wt%) were prepared using easy and highly efficient drop casting method. A PVDF mixture was prepared by adding 1 gm PVDF into 10 ml DMF, followed by the magnetic stirring for 2 h. Then a desired amount of nanofiller was dispersed into 3 ml DMF and ultrasonicated for 1 h. Further, this solution was added into the already prepared PVDF mixture and stirred for another 3 h.

The mixture was casted on the clean glass plate using a micro pipette and dried in an oven at 80 ^{0}C for 2 h. The glass plates were collected after the natural cooling of the oven and extracted the required films from the glass plates using deionised water. The thickness of the synthesised films were around 80-120 μm that were further used for different characterizations, dielectric measurements and fabrication of nanogenerators. The schematic representation of the thin film casting has been shown in Figure 5.1 (d). The synthesized pristine PVDF film and nanocomposite films with 0.625, 1.25, 2.5 and 5 wt% nanofiller concentrations were named as pristine PVDF, PTM0.6, PTM1.2, PTM2.5, and PTM5, respectively.

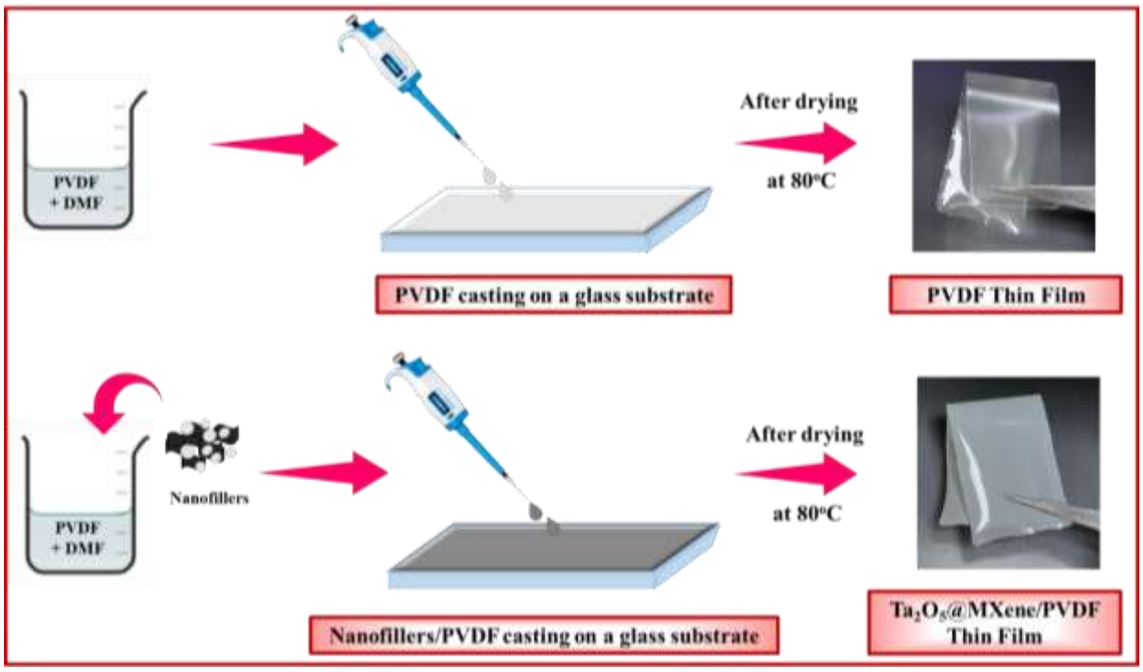

Figure 5.1 (d) The schematic diagram for the preparation of flexible nanocomposite films via drop casting method

5.3 Results and Discussion

5.3.1 Characterization of the Nanofillers

Figure 5.2 (a) contains the XRD pattern of the MAX phase (Ti_3AlC_2) and the prepared MXene. It can be observed from Figure 5.2 (a), the diffraction peak at around 38.8^0 ((104) plane) corresponding to aluminium layer of Ti_3AlC_2 disappeared after the hydrothermal process which indicates successful etching of Al. Additionally, the shift from 9.5^0 to 6.8^0 in 2θ position associated to (002) plane of Ti_3AlC_2 has been observed indicating that the interlayer spacing of Ti_3C_2 MXene has been increased after acid etching [96,196].

For the morphological observation of MXene nanosheets formation, field emission scanning electron microscopic (FESEM) images has also been shown in Figure 5.3. As shown in Figure 5.3 (a-c), the precursor Ti_3AlC_2 MAX phase shows a massive solid structure, which has turned into distinct layered structure with individual sheets stacked upon one another after the hydrothermal treatment (Figure 5.3 (d-f)). The transformation from a solid structure to sheets indicates the destruction of Ti-Al bonds between the layers due to etching reaction that can also be confirmed from XRD pattern of MXene.

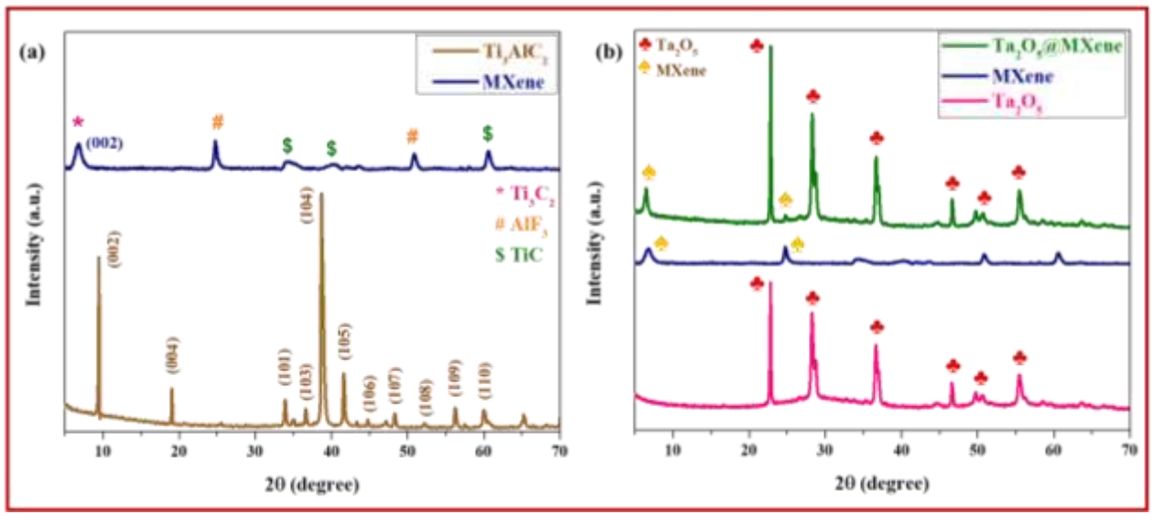

Figure 5.2 XRD pattern of (a) MAX phase and synthesized MXene, (b) Ta_2O_5 NPs, MXene nanosheets and MXene@Ta_2O_5 heterostructure

Further, the XRD patterns of prepared Ta_2O_5 NPs, Ti_3C_2 MXene and MXene@Ta_2O_5 heterostructure has been plotted and represented in Figure 5.2 (b). For Ta_2O_5, the diffraction peaks at 2θ ~ 22.90º, 28.46º, 36.84º, 46.83º, 49.78º, 50.75º and 55.66º are assigned to (001), (1 11 0), (1 11 1), (002), (0 22 0), (2 15 1), and (0 22 1) crystallographic planes, respectively. That confirms the orthorhombic phase of Ta_2O_5 (JCPDS no.: 25-0922) [172]. Further, in the diffraction pattern of MXene@Ta_2O_5 heterostructure, diffraction peaks corresponding to MXene and Ta_2O_5 are clearly visible. The characteristic peak of MXene associated to (002) plane further shifted from 2θ ~ 6.8^0 to 6.45^0 in the XRD pattern of MXene@Ta_2O_5. This shift suggests an increase in interlayer spacing (d) approximately from 12.99Aº to 13.69Aº that may be due to lattice expansion induced by Ta_2O_5 growth on the surface of MXene nanosheets [73,197].

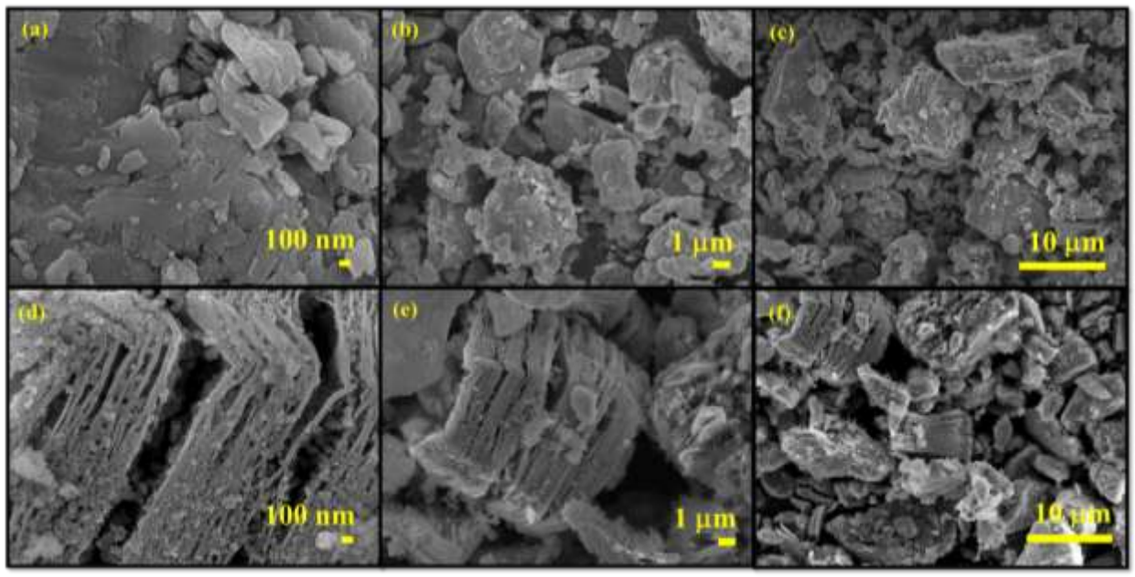

Figure 5.3 FESEM images of (a-c) Max phase (Ti_3AlC_2) and (d-f) MXene ($Ti_3C_2T_x$) nanosheets

In order to investigate the oxidation states of elements by determining the corresponding binding energies, XPS spectra of MXene@Ta_2O_5 heterostructure has been presented in Figure 5.4 (a-e). The wide XPS spectrum of MXene@Ta_2O_5 has shown in Figure 5.4 (a) where all the expected photopeaks are present. The graph illustrates that the nanofiller mainly contains four elements (Ti, Ta, O and C) in the full spectrum with no further contamination. The high-resolution spectra of Ta 4f region, O 1s, Ti 2p and C 1s has also been displayed in Figure 5.4 (b-e), where the dotted line represents the as recorded data and peaks corresponds to different energy levels has been deconvoluted using XPS peakfit software.

Figure 5.4 (b), demonstrated Ti 2p spectrum that has been deconvoluted mainly into 4 peaks corresponding to Ti-C $2p_{3/2}$, Ti-O $2p_{3/2}$, Ti-C $2p_{1/2}$, Ti-O $2p_{1/2}$ located at 455.67, 458.99, 461.64 and 463.56 eV, respectively. The appearance of Ti-O can be either due to slight oxidation of the MXene nanosheet's surface or unstability of –F terminal groups on MXene that can be easily replaced by –OH groups [73,198]. According to the XRD results of MXene@Ta_2O_5, there is no sign of bulk oxidation of TiO_2 phase that indicates the appearance of Ti–O in the Ti 2p spectrum is mainly due to the replacement of –F groups with –OH. The high resolution XPS spectrum of C 1s has shown in Figure 5.4 (c), where deconvoluted carbon components at 281.69, 282.73, 285.74 eV are assigned to C – C, C – O and C = O bonds, respectively. Furthermore, the observed peaks in Figure 5.4 (d) at around 24.91 eV and 23.05 eV corresponds to Ta $4f_{5/2}$ and Ta$4f_{7/2}$, respectively.

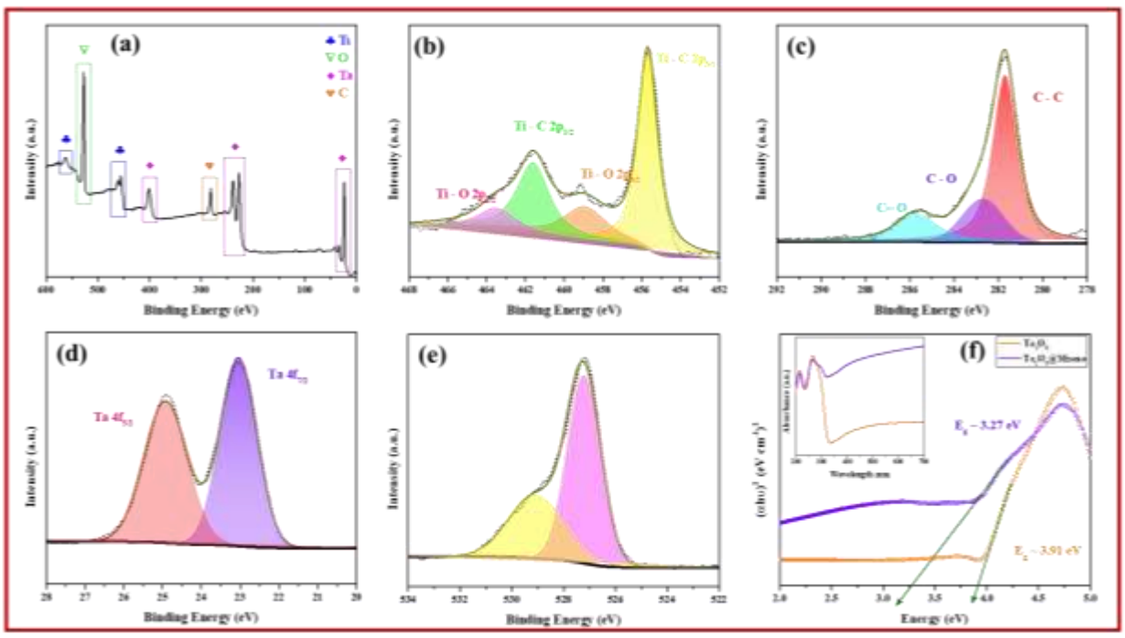

Figure 5.4 XPS Spectra of MXene@Ta_2O_5 (a) Survey scan, (b) Ti 2p, (c) C 1s, (d) Ta 4f, (e) O 1s, and (f) Tauc plot (inset: UV-Visible absorbance spectra of Ta_2O_5 and MXene@Ta_2O_5

The Ta 4f peak appears as a doublet due to the spin-orbit splitting with a value of ~1.8 eV, retaining the characteristic Ta^{5+} doublet positions. As compared to the pure Ta_2O_5 (Ta $4f_{5/2}$ ~29 eV & $Ta4f_{7/2}$ ~27 eV), there is a shift of 4 eV towards lower binding energy in the doublet peaks of Ta 4f core shell [123,199]. This shift is attributed to interfacial charge transfer and electronic coupling between Ta_2O_5 and MXene, confirming heterostructure formation [200,201]. The Figure 5.4 (e) represents O 1s spectra with the main peak at 527.25 eV referred to lattice oxygen bonded as Ta – O in Ta_2O_5 and the peak at 529.11 eV is usually attributed to the oxygen vacancies or defects [202]. The generated oxygen deficiency is consistent with the simultaneous appearance of lower binding energy Ta 4f components, supporting interfacial charge transfer in the MXene@Ta_2O_5 heterostructure. Overall, XPS analysis confirms the successful formation of MXene@Ta_2O_5 heterostructure with good interfacial electronic interaction.

To further support the formation of heterostructure, UV-visible spectroscopy has been used. The obtained UV-visible absorbance spectra of Ta_2O_5 and MXene@Ta_2O_5 has been represented in the inset of Figure 5.4 (f) that exhibit a strong absorption band at 264 nm [145]. Additionally, Tauc plot, a graph between $(\alpha h\nu)^{1/n}$ and photon energy has been shown in Figure 3(f), where α is the absorption coefficient, h is Planck's constant and ν is the frequency of the light and n is Tauc exponent. The optical energy band gap of the samples has been measured by extrapolating the

linear section of the Tauc plot [144]. In our analysis, the best-fitted values correspond to the linear section for n=1/2, indicating that Ta_2O_5 NPs have a direct energy band gap of ~3.91eV that has reduced to ~3.27eV for the MXene@Ta_2O_5 heterostructure. This reduced optical band gap further indicates the synergistic interaction of Ta_2O_5 and MXene within the heterostructure.

5.3.2 Structural and Morphological Study of MXene@Ta_2O_5/PVDF Nanocomposite Films

In order to authenticate the distinct phases and to verify the influence of MXene@Ta_2O_5 filler on the crystallization and phases of PVDF matrix, XRD results of prepared films were examined. Figure 5.5 (a) shows the XRD patterns of the pristine PVDF and MXene@Ta_2O_5/PVDF nanocomposite films with different filler concentration. The diffraction pattern of pure PVDF shows a crystallization peak related to the β-phase and a minor peak corresponding to α-phase at $2\theta \sim 20.25^0$ and 18.65^0, respectively [174,175]. There is no significant change in these diffraction peak positions in the nanocomposite films as compared to pure PVDF. However, a variation in the intensities of α and β-phase has been observed [203]. The intensity of peak corresponding to β-phase has been noticed to increase relatively till PTM1.2 and reduces beyond that concentration. Also, the diffraction peaks related to Ta_2O_5 at 22.90°, 28.46°, 36.84° started appearing after PTM1.2. It can be due to the major presence (80%) of Ta_2O_5 in nanofiller.

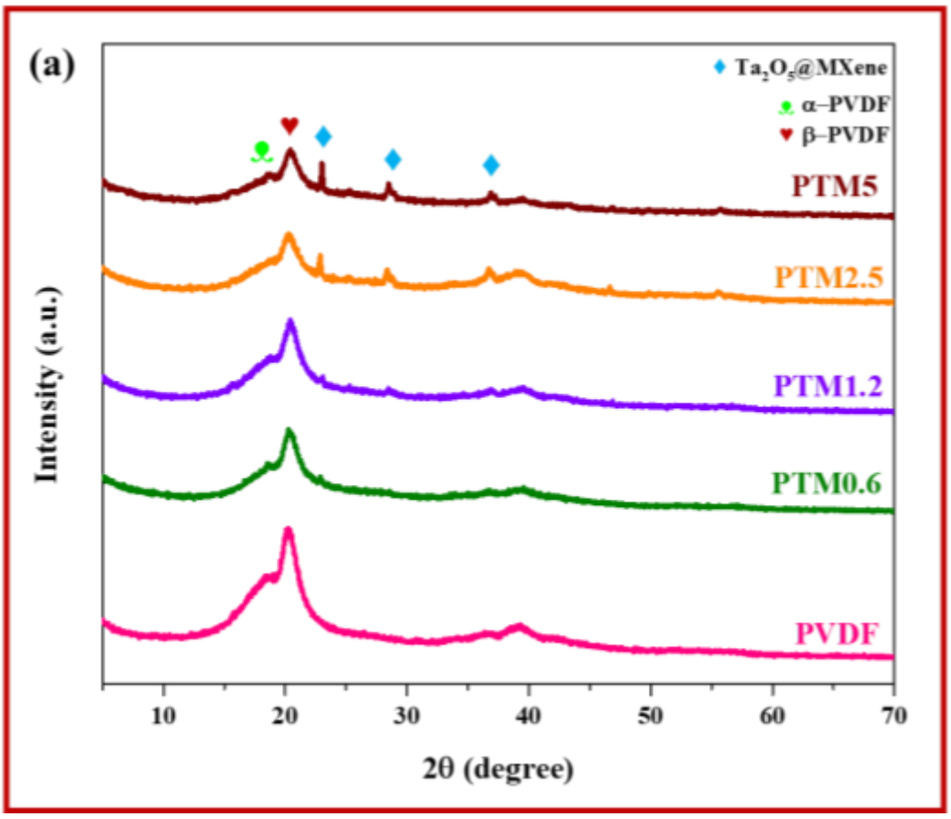

Figure 5.5 (a) XRD pattern of Pristine PVDF and nanocomposite films

Moreover, the XRD patterns of nanocomposite films, suggest that the addition of the nanofiller did not greatly affect the crystallization form of the PVDF. To confirm this, crystallinity percentage (X_{ct}) of the nanocomposite thin film has been calculated using equation 5.9, where A_c and A_a are the area under the crystalline and amorphous regions [73].

$$X_{ct} = \frac{\Sigma A_c}{\Sigma A_c + \Sigma A_a} \times 100 \tag{5.9}$$

The deconvoluted curves of the XRD pattern has been shown in Figure 5.5 (b-f). The calculated X_{ct} for the films are not much distinct from the pure PVDF that shows no significant change in crystallinity on addition of nanofillers in the PVDF matrix.

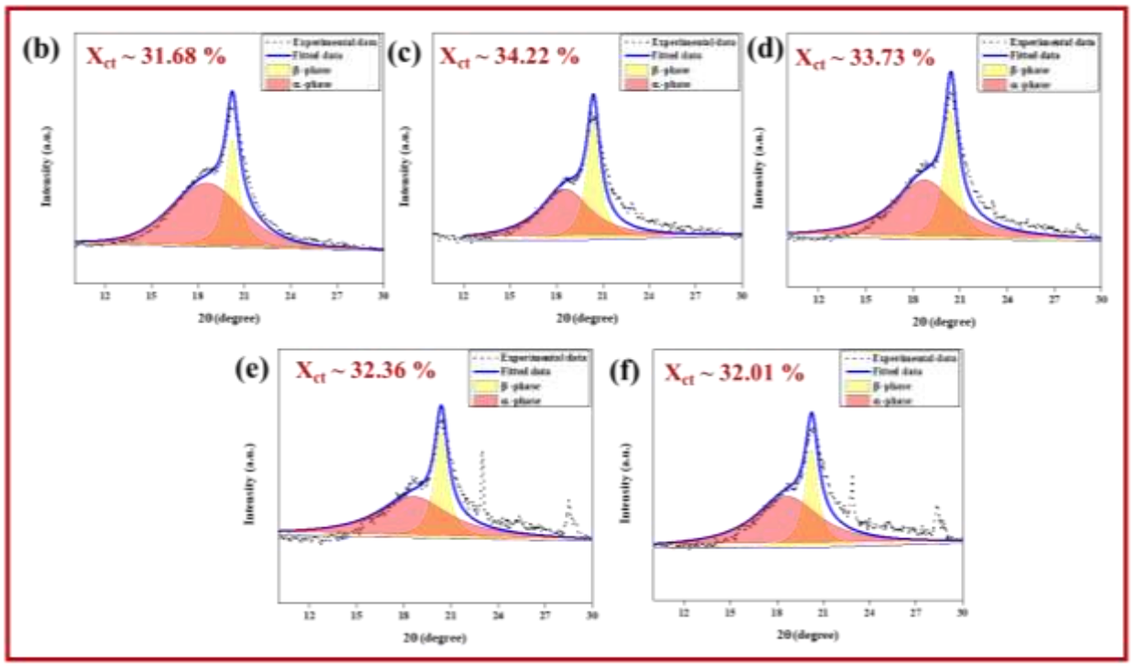

Figure 5.5 (b) deconvoluted curves of XRD pattern for (b) pure PVDF, (c) PTM0.6, (d) PTM1.2, (e) PTM2.5, (f) PTM5 films

Figure 5.6 (a-e) displays the SEM images of the prepared PVDF nanocomposite films. Figure 5(a) shows that pristine PVDF film have randomly distributed spherulite structure along with certain pores. On the addition of nanofillers, reduction in pores has been observed and the films developed a smooth surface [204]. SEM images of PTM0.6 and PTM1.2 film are relatively even as compared to other films. Surface of the PTM2.5 and PTM5 appears to be rough because of the more nanofiller dispersion. These visible white spots in SEM images refer to MXene@Ta_2O_5 distributed over the PVDF matrix. The higher concentration of nanofillers can also cause agglomeration that restricts the further incorporation of the nanofillers in the polymer matrix [168,195].

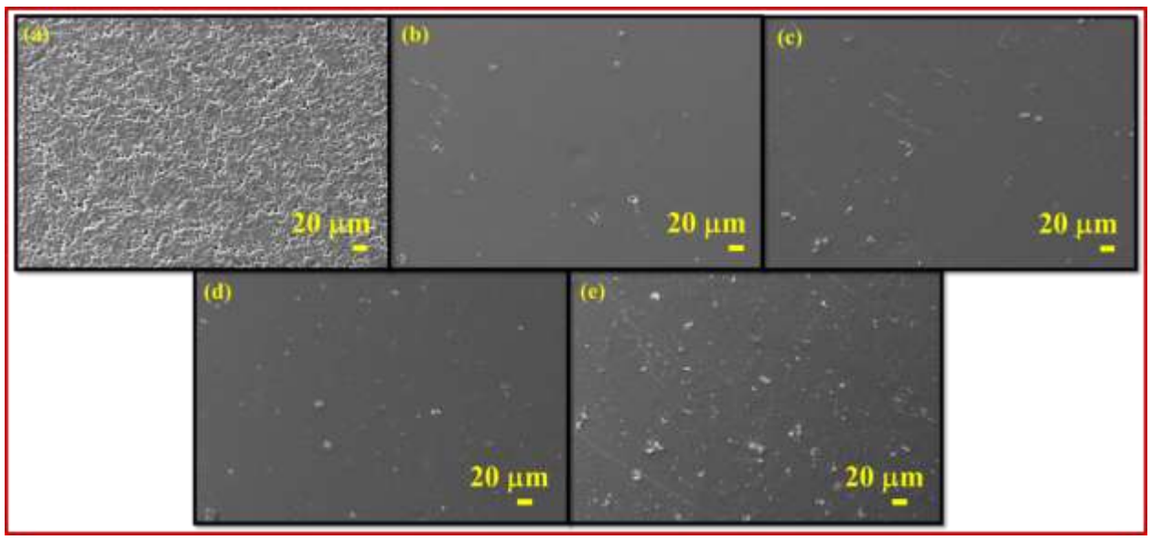

Figure 5.6 FESEM images of (a) pure PVDF, (b) PTM0.6, (c) PTM1.2, (d) PTM2.5, (e) PTM5 nanocomposite films

Further, for the quantitative analysis of β-phase in the MXene@Ta_2O_5/PVDF nanocomposite films FTIR absorption spectra were obtained and shown in Figure 5.7 (a). Prominent absorption peaks observed at around 840, 1230 and 1400 cm^{-1} refer to β-phase, whereas peaks at around 602, 762, 808 cm^{-1} are related to the α-phase of PVDF [178]. The β-phase of PVDF depends on the alignment of dipoles associated with the -CH_2-CF_2- repeating units within PVDF that efficiently contributes to its net polarization and piezoelectric performance. Hence, FTIR absorption spectra were used to calculate the β-phase percentage of PVDF based nanocomposite films. The relative β-phase content was obtained using Lambert-Beer law with the help of equation 5.10 [14].

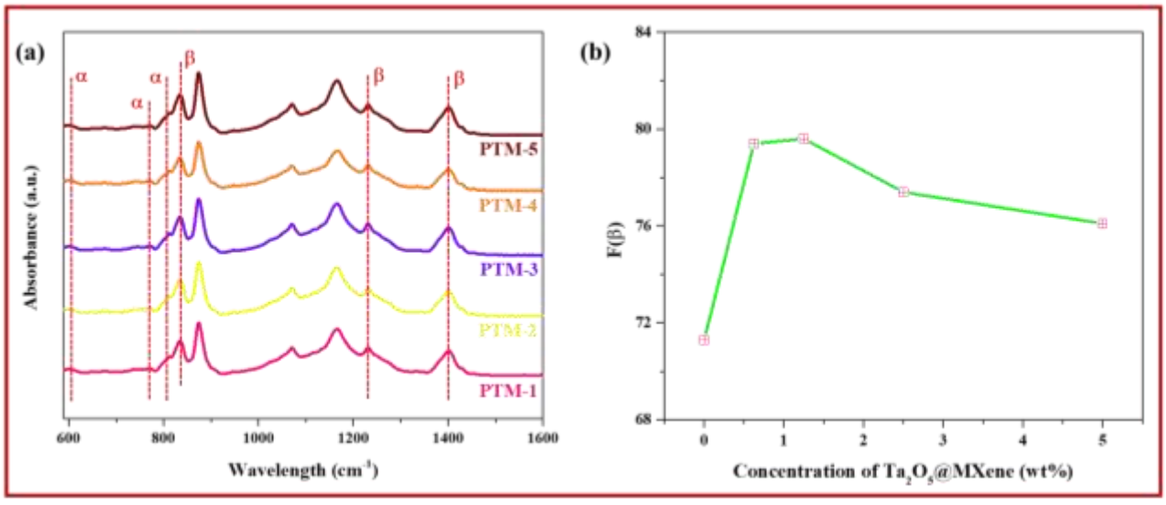

Figure 5.7 (a) FTIR spectra of of pristine PVDF and MXene@Ta_2O_5/PVDF nanocomposite films and (b) graph of β-phase content w.r.t. nanofiller concentration in the nanocomposite films

$$F(\beta) = \frac{A_\beta}{\left(\frac{K_\beta}{K_\alpha}\right)A_\alpha + A_\beta} * 100\% \quad (5.10)$$

where, F(β) gives the content of β-phase in the respective nanocomposite thin film, K_β = 7.7 x 10^4 cm^2/mol and K_α = 6.1 x 10^4 cm^2/mol are the absorption coefficient at 840 cm^{-1} and 762 cm^{-1}, respectively. Absorption at 762 cm^{-1} is denoted by A_α and for 840 cm^{-1} is denoted as A_β. The calculated β-phase content is ~71% for pristine PVDF film. The optimal addition of nanofillers (1.25 wt%) in PVDF matrix, has increased the β-phase of PVDF by 13%. This enhancement suggests that in the optimised PTM1.2 film, the net amount of polarization has increased due to the filler-polymer interfacial interaction [193]. Moreover, for the films with larger nanofiller concentration (PTM2.5 and PTM5), β-phase amount started to decrease. This can be possibly due to the generation of conducting paths formed by MXene at higher concentration of filler [205]. The agglomeration of MXene@Ta_2O_5 suggested by the SEM micrographs can be another reason for the decreased β-phase for films with higher filler concentration. The calculated percentage of β-phase present in the different nanocomposite films has been shown in Figure 5.7 (b).

5.3.3 Impedance Study of Nanocomposite Films

Besides, to investigate the dielectric behaviour of the the pristine PVDF and MXene@Ta_2O_5/PVDF nanocomposite films, impedance spectroscopy has been used. The dielectric properties of the films were inspected as a function of operating temperature (room temperature to 120 ºC) and applied field frequency (20 Hz to 10 MHz). The dielectric constant (ε′) and the loss tangent (tan δ) are calculated using the equation 5.11 and 5.12, respectively [195].

$$\varepsilon'(\omega) = \frac{C_p d}{\varepsilon_o A} \quad (5.11)$$

$$tan\delta = \frac{\varepsilon''(\omega)}{\varepsilon'(\omega)} \quad (5.12)$$

Where, ε′ and ε″ are the real and imaginary part of permittivity, ω is the angular frequency of applied electric field, C_p is the measured parallel plate capacitance, d and A are the thickness and cross-sectional area of the synthesised film, ε_o is the permittivity of free space, δ = (90-θ) and θ is the phase difference between the applied voltage and current.

Figure 5.8 (a-e) illustrates the temperature dependence (30 to 120 ºC) of ε′ for the nanocomposite films across various field frequencies. All nanocomposite films consistently show that ε′ rises with increasing temperature. This increase is primarily attributed to thermal agitation, which enhances the orientational freedom of the polar sites in the PVDF chains, allowing them to align more readily with the alternating electric field [115,178]. Further, Figure 5.9 (a-e) depicts the associated loss tangent (tan δ) as a function of temperature, and a similar increasing trend has been observed. This escalating energy dissipation factor signifies the initialization of thermal deterioration at elevated temperature, where the increased dipole mobility results in greater energy loss [185]. The introduction of the MXene@Ta_2O_5 in PVDF matrix at an optimal concentration (1.25 wt%) improves its ε′ value as compared to the pristine PVDF. The optimized PTM1.2 film also maintains low tan δ (0.015 at 30 ºC and 0.161 at 120 ºC) at 1 KHz.

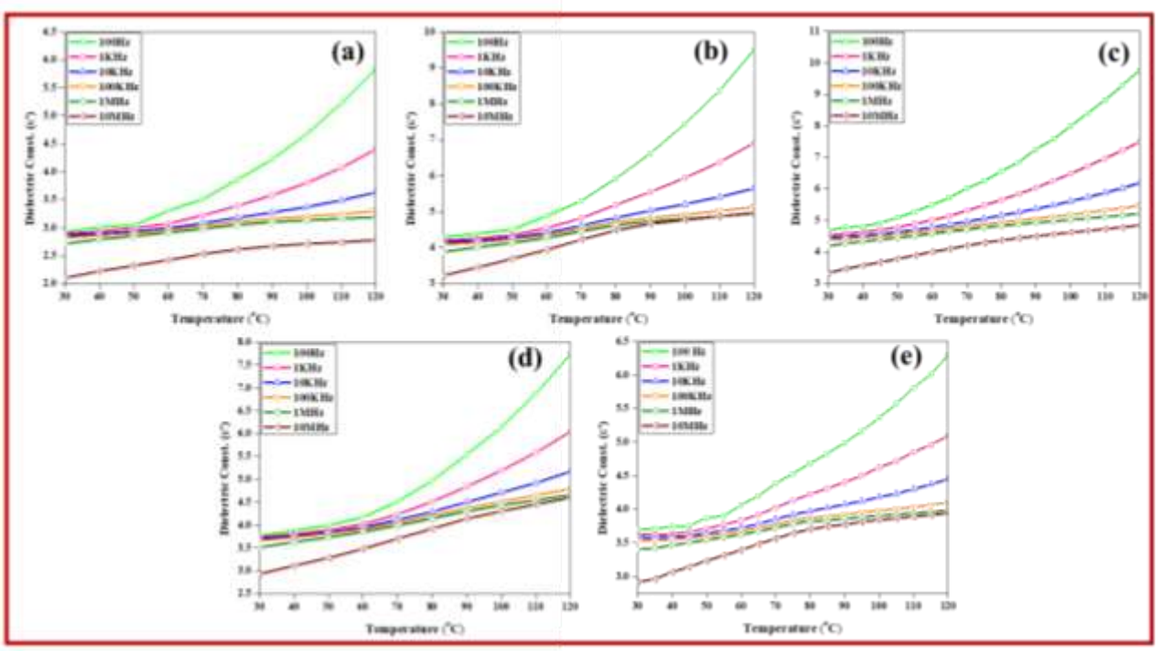

Figure 5.8 Dielectric constant curves w.r.t. temp. at different applied freq. for the films (a) PVDF, (b) PTM0.6, (c) PTM1.2, (d) PTM2.5, and (e) PTM5

This enhancement in dielectric properties of PTM1.2 has initially linked to the high polarizability of the MXene@Ta_2O_5 component, governed by the Maxwell-Wagner-Sillar (MWS) effect due to charge build-up at the filler-polymer interfaces [206]. In the nanocomposite films, MXene sheets worked as conducting plates that multiplied the microcapacitor structures with in the

nanocomposite film. The surface terminations of MXene also interacts with the PVDF chains that results in amplified dipole alignments, thus enhanced β-phase [22,207]. However, MXene being conductive can form conductive pathways that increases the leakage and decreases the breakdown strength of the films. By forming the heterostructure of MXene and Ta_2O_5 solved this problem. Ta_2O_5 effectively isolates the MXene sheets, suppressing leakage and maintaining low tan δ. The synergistic multiple-interface polarization (Ta_2O_5-PVDF, MXene-PVDF, Ta_2O_5-MXene) enables the nanocomposite to outperform the overall dielectric stability. However, for higher concentrations, ε′ begins to decrease. This degradation may be due to excessive agglomeration of nanofillers or generation of conductive pathway which diminishes the MWS effect. PTM1.2 film successfully balances high ε′ with minimized energy loss, which is essential for energy applications.

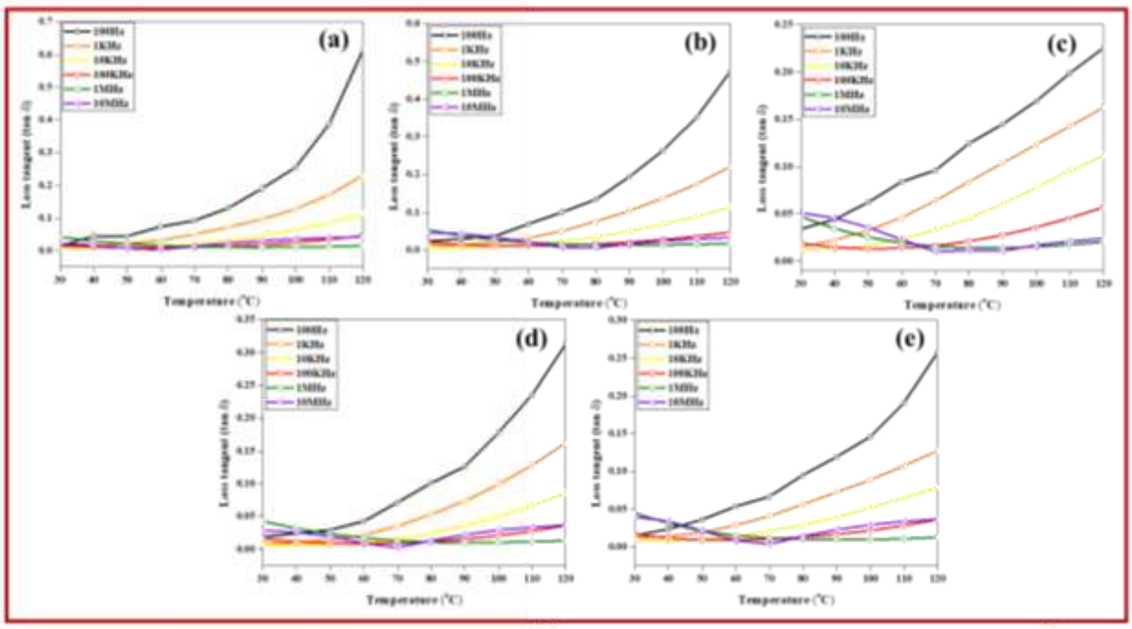

Figure 5.9 Loss tangent curves w.r.t. temp. at different applied freq. for the films (a) PVDF, (b) PTM0.6, (c) PTM1.2, (d) PTM2.5, and (e) PTM5

Moreover, Figure 5.10 (a-e) illustrates the inverse relationship between the dielectric constant (ε′) and the applied field frequency (ν). At high temperatures (>60 ºC), a frequency dependence is clearly visible, while ε′ remains nearly constant at low operating temperatures. In the low-frequency region, high ε′ values and prominent dispersion are observed, primarily driven by the enhanced interfacial polarization [186,195]. As frequency increases through the intermediate region, the charge carriers struggle to follow the rapid field oscillations, causing the interfacial

polarization to diminish. Consequently, in the high-frequency region, ε′ tends toward saturation, as the time period becomes too short for the charge carriers to align, confirming the limitations of the polarization mechanism at high oscillation rates [185].

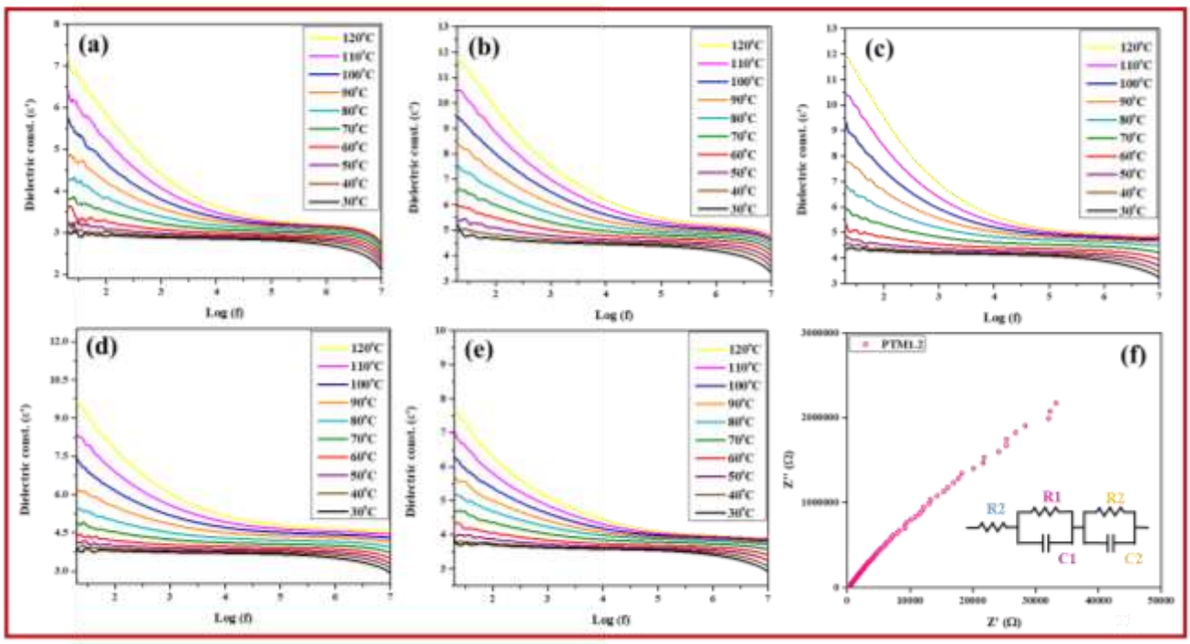

Figure 5.10 Dielectric constant vs applied frequency at different operating temp. for the films (a) PVDF, (b) PTM0.6, (c) PTM1.2, (d) PTM2.5, (e) PTM5 and (f) Nyquist plot for PTM1.2 film at RT

For the optimized PTM1.2 nanocomposite film, Figure 5.10 (f) represents the Nyquist plot providing a crucial insight into film's electrical characteristics [206]. The graph exhibits a single, continuous sloping line across the measured frequency range, which is indicative of a dominant capacitive behaviour and high insulating properties [208]. The impedance data has been fitted using an equivalent circuit shown along with the graph. The total conductivity of PTM1.2 is ~ 4.4 x 10^{-11} Scm^{-1} that has been calculated using equation 5.13.

$$\sigma = \frac{d}{R \times A} \tag{5.13}$$

Where, d is the thickness and A is the cross-sectional area of the film and R is the total resistance of the film [209]. The resulting low conductivity value confirms the insulating nature of the PVDF based nanocomposite film which is essential for minimizing leakage current in energy harvesting devices.

5.3.4 Mechanical Properties of Nanocomposite Films

Further, to study the mechanical properties of the MXene@Ta_2O_5/PVDF nanocomposite films, rectangular films (70 mm x 20 mm) has been cut. The stress-strain curves of the prepared films have been plotted in Figure 5.11 (a). The obtained tensile strength of the pristine PVDF, PTM0.6, PTM1.2, PTM2.5 and PTM5 films are ~ 32.5, 22.6, 26.7, 21.3 and 16.6 MPa, respectively. After the pristine PVDF, PTM1.2 film have the highest tensile strength that shows its load bearing capacity. Furthermore, the initial region of the stress-strain curves has been used to calculate the Young's modulus of the films that has been shown in Figure 5.11 (b) w.r.t. different nanofiller concentrations [159]. The Young's modulus for the pure PVDF film is ~8.34 MPa and for PTM1.2 film it has increased to ~8.62 MPa. After the 1.25 wt% concentration of the nanofillers, Young's modulus reduces to 7.24 MPa for PTM5 film. The enhanced elasticity of the PTM1.2 film may be due to the improved adhesion between the MXene@Ta_2O_5 and PVDF chains [181], hence reduced free volume in the PVDF matrix that limited the mobility of PVDF chains [183]. The nanofillers acted as the stress transfer points under mechanical force that leads to improved its stress bearing capacity [182]. These results suggest that reinforcement of MXene@Ta_2O_5 in PVDF improves the mechanical performance of the films which is advantageous for the flexible electronic devices.

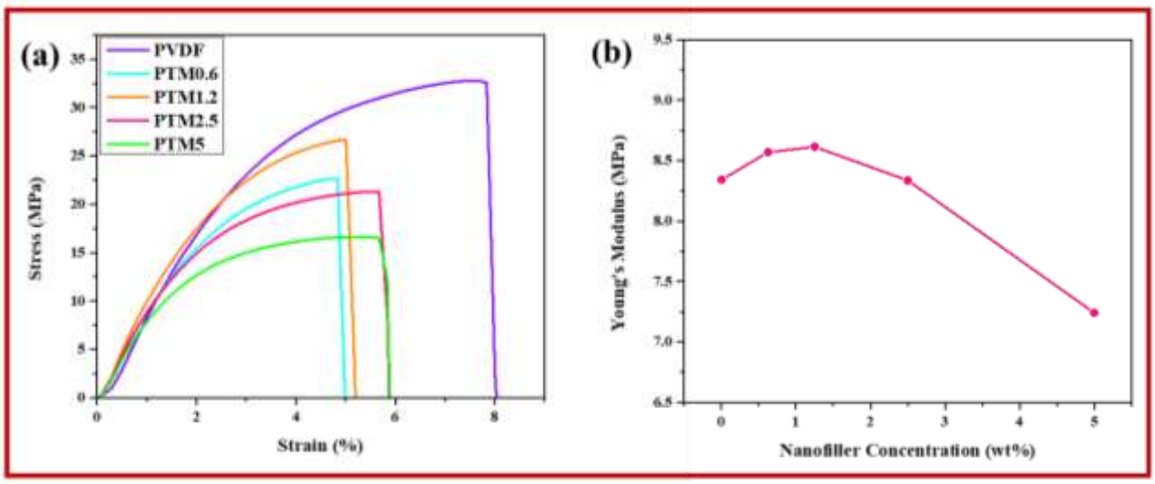

Figure 5.11 (a) Stress-Strain curves and (b) variation in Young's Modulus with MXene@Ta_2O_5 concentration for pure PVDF and nanocomposite films

5.4 Conclusion

In this work, we have successfully developed synthesized MXene@Ta_2O_5 heterostructure via hydrothermal method. The structural characterization of the synthesised nanofiller using XRD confirmed the presence of all the required diffractions peaks corresponds to Ta_2O_5 and MXene. XPS confirmed the chemical stability of the prepared sample and indicated a shift in binding energy of MXene@Ta_2O_5 as compared to Ta_2O_5. Moreover UV-visible spectra show Ta_2O_5 NPs have a direct energy band gap of ~3.91eV that has reduced to ~3.27eV for the MXene@Ta_2O_5 heterostructure. This reduced optical band gap further indicates the synergistic interaction of Ta_2O_5 and MXene within the heterostructure. Further, we have prepared PVDF nanocomposite thin films reinforced with MXene@Ta_2O_5 at different weight % using a solution casting method. The fabricated flexible MXene@Ta_2O_5/PVDF nanocomposite films were systematically optimized for their dielectric properties via impedance spectroscopy. The impedance study confirmed the substantial improvement in the nanocomposite's dielectric constant that enhanced the net polarization of the PTM1.2 film. At an optimal nanofiller concentration of 1.25 wt%, the resulting film has a dielectric constant of ~. Additionally, MXene@Ta_2O_5 maintained the tensile strength of the nanocomposite film that demonstrates its mechanical resilience. Collectively, MXene@Ta_2O_5/PVDF nanocomposite is stable, flexible and scalable material solution for the next generation of flexible and self-powered systems.

CHAPTER 6

Applications of the Synthesized Flexible Nanocomposite Films for Mechanical Energy Harvesting and Storage Devices

Herein, the prepared Ta_2O_5@PVDF and MXene@Ta_2O_5/PVDF flexible films at different wt% concentration were used to fabricate the piezoelectric nanogenerators (PENG) for harvesting biomechanical energy efficiently. At the optimal 1.25 wt% concentration of Ta_2O_5 and MXene@Ta_2O_5, the fabricated PENG generated the maximum output voltage i.e, around 56 V and 75 V, respectively. The maximum voltage produced by MXene@Ta_2O_5/PVDF based PENG is around 2.5 times higher than the pristine PVDF. The enhanced piezoelectric performance of the nanocomposite films is ascribed to various reasons that has been described in this chapter. The film that generated the best output has been used to fabricate triboelectric nanogenerator (TENG) with varying dimensions. TENG based on MXene@Ta_2O_5/PVDF achieved almost fivefold voltage output as compared to the pristine PVDF. Additionally, the power output for the PENG and TENG at different load resistance along with the overall voltage stability over 500 cycles of mechanical stimulus has been examined. The real time applications of the nanogenerators have also been demonstrated for the practical uses. Moreover, MXene@Ta_2O_5/PVDF has been tested for its supercapacitor capabilities towards self-charging piezo-supercapacitor. It showed good areal capacitance of ~159 mF/g at scan rate of 5mV/s. Collectively, the Ta_2O_5@MXene/PVDF nanocomposite represents a stable and scalable material solution for the next generation of flexible and self-powered systems such as self-monitoring and decision-making.

6.1 Introduction

The escalating global energy demand, coupled with the rapid proliferation of portable electronic devices, wireless sensor networks, and wearable technologies has necessitated the development of sustainable and self-powered energy solutions [190,210]. Conventional power sources, such as chemical batteries, encounter intrinsic impediments regarding lifespan, weight, size and environmental toxicity that makes the development of alternative energy transducers necessary [210,211]. Among the various ambient energy sources, the abundant mechanical energy present in human motion, environmental vibrations, machine operations etc. can be effectively converted into usable electrical energy through nanogenerators [212]. For harvesting mechanical energy, numerous principles have been established over the years based on diverse mechanisms, such as piezoelectric [33,213], electromagnetic [214,215], and triboelectric [216,217].

From the diverse array of energy harvesting technologies, flexible piezoelectric nanogenerators (PENG) have garnered significant attention due to their wide range of potential uses. Their advantageous characteristics include simple architecture, high power density, scalability, and ability to operate under low-frequency mechanical stimuli [22,218,219]. PENG function based on the fundamental piezoelectric effect, wherein applied mechanical stress induces polarization and the generation of an electric potential in certain materials. Concurrently, TENG leverage the combination of triboelectrification and electrostatic induction to convert mechanical movements into electrical energy.

Parallel to PENGs, triboelectric nanogenerators (TENG) have emerged as a highly robust and complementary technology for broad-scale energy harvesting. TENGs leverage the synergistic combination of contact electrification (triboelectrification) and electrostatic induction to convert ubiquitous mechanical movements, such as tapping, sliding, or structural vibration etc. into electrical energy [217,220]. Due to their broad material availability, exceptionally high voltage outputs, and sensitivity to macroscopic mechanical motions, TENGs represent a highly scalable approach to self-powered systems.

Despite the efficient power outputs of both PENG and TENG, a fundamental operational challenge remains. The generated electrical output is inherently intermittent and pulsed, fluctuating directly with the external mechanical stimuli. To provide a stable, continuous supply required to drive modern electronics, this irregular energy must be captured and regulated. Consequently,

integrating these nanogenerators with high-performance energy storage units, such as supercapacitors, is a critical requirement. Developing multifunctional materials capable of both mechanical energy harvesting and rapid electrochemical energy storage paves the way for monolithic, self-charging piezo-supercapacitors, effectively resolving the intermittency issue and ensuring uninterrupted device operation [45,221].

In this context, the strategic combination of highly functional nanofillers within the PVDF matrix offers a clear pathway towards developing advanced multifunctional energy systems. The reinforcement of these nanofillers in the PVDF matrix serve a dual purpose, (i) they enhance the overall dielectric permittivity (ε′), thereby amplifying polarization in the matrix and (ii) induce the more polarized charge accumulation on the interfaces that promote the formation and stability of the desirable polar β-phase in PVDF, hence significantly boosting the output of the nanogenerators [160,190,193].

Therefore, in this work, we fabricated Ta_2O_5/PVDF and Ta_2O_5@MXene/PVDF nanocomposite based flexible piezoelectric nanogenerator (PENG). The optimal concentration was determined to be 1.25 wt% at which the fabricated PENG exhibited the highest voltage of ~ 75V for Ta_2O_5@MXene/PVDF that is 2.5 times higher than that generated by the pristine PVDF device (30 V). Further, the Ta_2O_5@MXene/PVDF-based TENG device has been fabrication with varying dimensions. Moreover, the real time applications of the nanogenerators have also been demonstrated for the practical use. Furthermore, MXene@Ta_2O_5/PVDF has also been tested for its supercapacitor capabilities towards self-charging piezo-supercapacitor.

6.2 Piezoelectric Nanogenerator (PENG)

6.2.1 Device Fabrication Process

For PENG, the nanocomposite film has been sandwiched between two flexible aluminium (Al) electrodes and then encapsulated using Kapton tape for mechanical durability and insulation. Copper (Cu) wire attachments are used to collect signals. Then, periodical mechanical stress (tapping) has been applied on the device and measurements such as open-circuit voltage, power output etc. has been collected. A schematic diagram and digital picture of the fabricated PENG have been demonstrated in Figure 6.1 (a).

6.2.2 Mechanism involved in PENG

The internal dipoles of a piezoelectric film are randomly oriented at rest. When a mechanical force is applied to the piezoelectric film, those internal dipoles become aligned by the stress. This stress-induced dipole alignment creates opposite charges to accumulate on the top and bottom electrodes attached to the film, producing a measurable voltage across them. As the pressure is released the film relaxes and the dipoles loss their alignment leads to charge dissipation. This produces an opposite polarity signal during the release state. The total voltage returns to zero once the film fully recovers or get back to the rest state. A block diagram of the mechanism involved in PENG has been represented in Figure 6.1(b). Repeating this compress-release cycle generates an alternating electrical output that can be harvested. This alternating voltage output can be converted further into a unidirectional voltage suitable for practical energy-harvesting applications using a rectifier circuit.

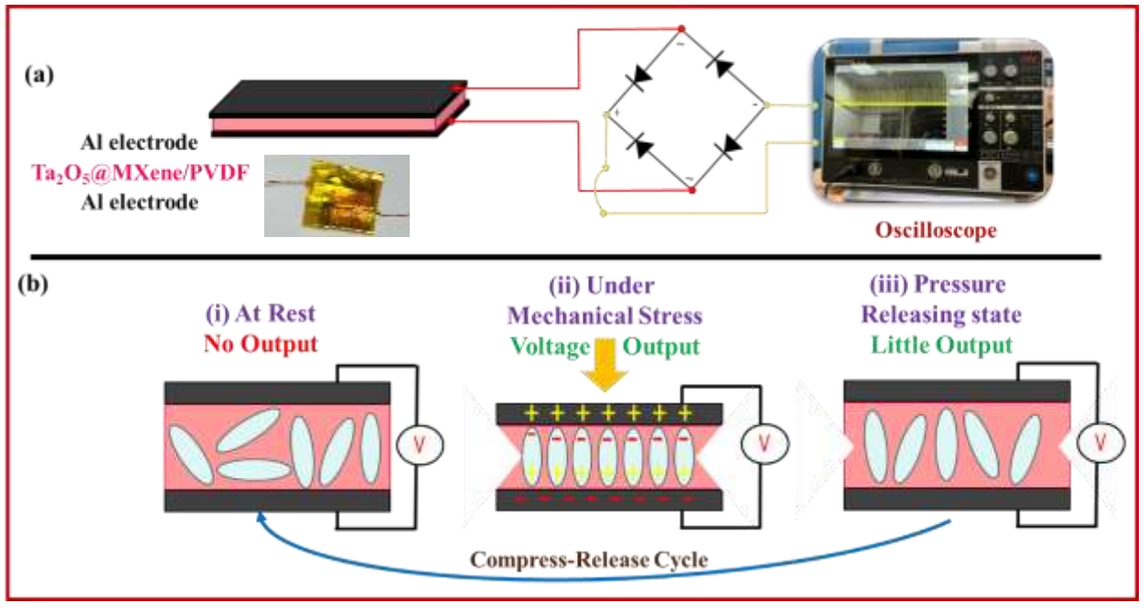

Figure 6.1 The schematic diagram of (a) fabrication and measurement and (b) mechanism involved in piezoelectric nanogenerator (PENG)

6.2.3 Output Performance of Piezoelectric nanogenerator (PENG)

6.2.3.1 Ta_2O_5@PVDF based PENG

To study the piezoelectric properties of the Ta_2O_5@PVDF nanocomposite films, PENG based on prepared nanocomposite films () and with dimensions 2x2 cm^2 has been fabricated. The prepared nanocomposite films with 0.625, 1.25 and 2.5 wt% of Ta_2O_5 has been named as TaP1, TaP2 and

TaP3, respectively. The fabricated nanogenerators put under continuous mechanical stress using palm-induced tapping. The Figure 6.2 (a-d) shows the rectified voltage output for the PENGs devices based on Ta_2O_5@PVDF nanocomposite films. The obtained voltage for the pristine PVDF based device is ~ 28 V and for TaP1, TaP2 and TaP3 based PENG devices are 42 V, 56 V and 22 V, respectively. It has been observed that the TaP2 based nanogenerator have the highest generated voltage that is around twice of pristine PVDF device. This enhanced piezoelectric performance is related to the improved dielectric constant [191,222]. The dielectric behaviour of a material is highly dependent on the number of polarised dipoles in the material. The improved dielectric behaviour suggests the presence of elevated polar β-phase content i.e, more dipole alignment along the -CH_2-CF_2- chains of PVDF [219,223].

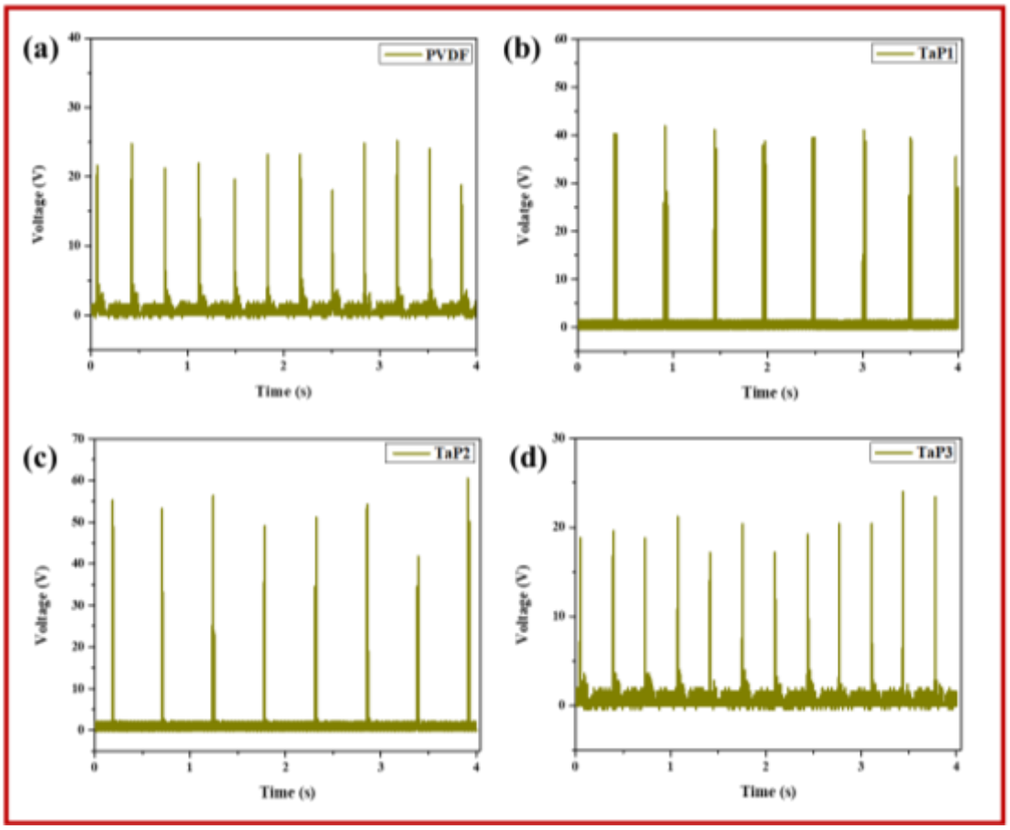

Figure 6.2 Generated voltage output vs time waveforms for (a) PVDF, (b) TaP1, (c) TaP2 and (d) TaP3 based PENG nanogenerators

In addition to the above measurements, the influence of load resistance on the output voltage, current and power management capabilities of the TaP2 based PENG device was evaluated. The output voltage was recorded across a series of load resistance and the result has been plotted in Figure 6.3 (a). Additionally, power density (P) has been calculated using equation 6.1, where V is the generated voltage output across the load resistance (R_L) and A is the cross-section area of the device [210].

$$P = \frac{V^2}{R_L \times A} \tag{6.1}$$

$$I = \sqrt{\frac{P \times A}{R_L}} \tag{6.2}$$

The calculated power density with respect to load resistances has been illustrated in Figure 6.3 (b). The maximum power observed for the nanogenerator is ~0.100 mW/cm^2 (100 μW/cm^2) at an optimal load resistance of 1 MΩ. Moreover, the output current has been calculated using equation 6.2 illustrated in Figure 6.3 (a). As the load resistance increases, the output current decreases due to the finite internal resistance of the device, which limits charge transfer under higher electrical impedance. Further, to ensure the stability and durability of the fabricated piezoelectric nanogenerator, 2000 cycles of mechanical stimulus were given to the TaP2 based nanogenerator. The resulting voltage output shows no serious degradation that has been exhibited in Figure 6.3 (c).

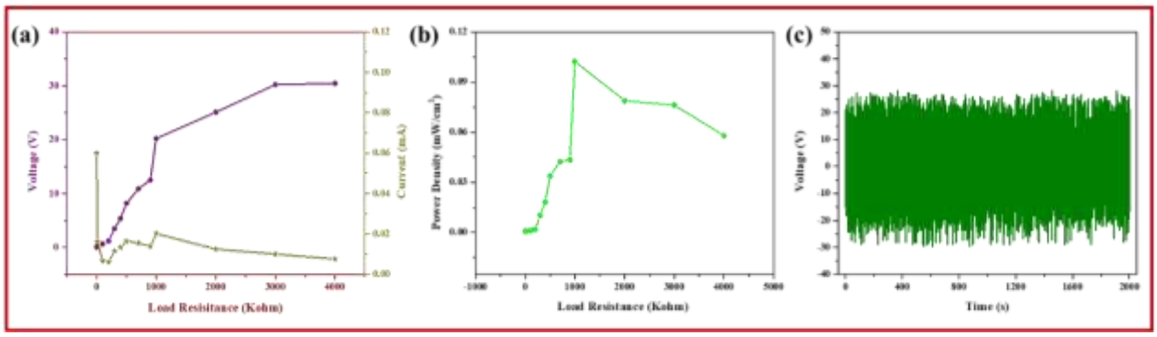

Figure 6.3 (a) Voltage output across different load resistance, (b) power density w.r.t. different load resistance and (c) stability curve of TaP2 based PENG

To check the practical viability of the fabricated TaP2 based PENG device in real world application, circuit has been constructed on a breadboard to demonstrate energy harvesting capability. The mechanical input applied to the PENG successfully actuate more than 15 commercially available LEDs. The live images of the lighted LEDs and has been displayed in Figure 6.4 (b). Furthermore, to quantify the energy storage capacity of the TaP2 based PENG, various capacitors has been charged using harvested mechanical energy. The voltage across the 1, 2.2, 4.7 and 10 μF capacitors have reached upto 625, 600, 570 and 525 mV within 50s, respectively

demonstrating the device's ability to efficiently charge small energy storage units. The graph of generated voltage output across the capacitors has been shown in Figure 6.4 (a).

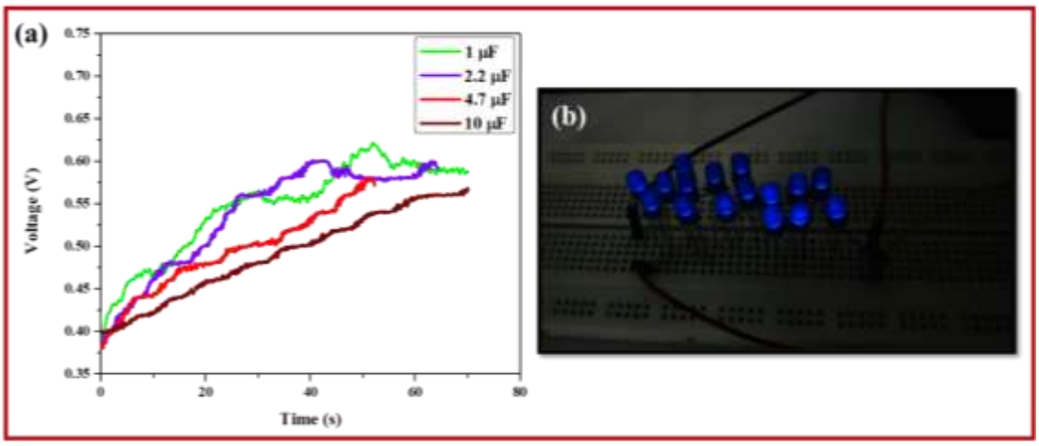

Figure 6.4 (a) Voltage output curve across capacitor 1, 2.2, 4.7 and 10 μF (b) LEDs glowing on applying mechanical force on TaP2 based PENG

6.2.3.1 MXene@Ta_2O_5/PVDF based PENG

The prepared nanocomposite films with 0.625, 1.25 and 2.5 wt% of MXene@Ta_2O_5 has been named as PTM0.6, PTM1.2, PTM2.5 and PTM5, respectively. To study the piezoelectric properties of the Ta_2O_5@MXene/PVDF based PENG has been fabricated with 2x2 cm^2 dimensions. The fabricated nanogenerators put under continuous mechanical stress using palm-induced tapping. The Figure 6.5(a-e) shows the rectified voltage output for the PENGs devices based on nanocomposite films. The obtained voltage for the pristine PVDF based device is ~ 30.4V and for PTM0.6, PTM1.2, PTM2.5, PTM5 based PENG devices are 58.6V, 77.6V, 42.5V and 25.3V, respectively. It has been observed that the PTM1.2 based nanogenerator have the highest voltage output that is around 2.5 times of pristine PVDF device. This enhanced piezoelectric performance is related to the improved β-phase [191,222]. The β-phase content is highly dependent on the extent of dipole alignment along the -CH_2-CF_2- chains of PVDF. When PVDF achieves the all trans (TTTT) conformation, the individual dipole moments add constructively that results in strongly polarized and piezoelectrically active material leading to an elevated β-phase of PVDF [219,223]. The impedance spectroscopy also verifies the enhanced polarization for PTM1.2 film. Further, for PTM2.5 and PTM5, output voltage decreases that can be attributed to the reduced β-phase content as evidenced by FTIR. The reduction in β-phase implies that -CH_2-CF_2- units are less aligned with

each other. A comparative bar graph of the generated voltages for different MXene@Ta_2O_5/PVDF based PENG has also been presented in Figure 6.5 (f).

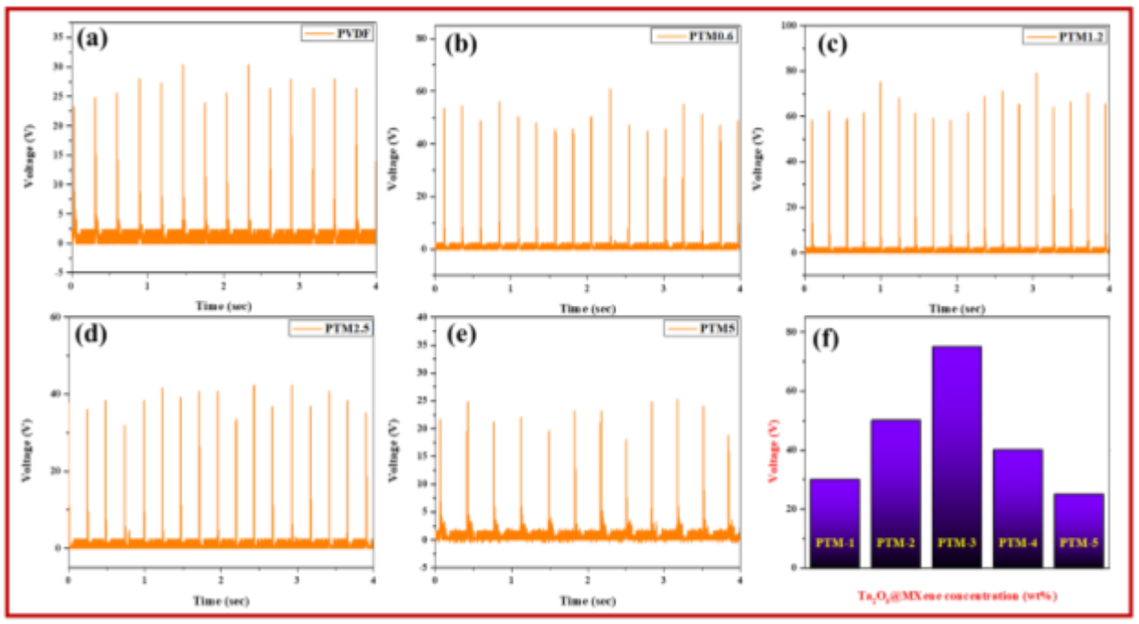

Figure 6.5 Generated voltage output vs time waveforms for (a) PVDF, (b) PTM0.6, (c) PTM1.2, (d) PTM2.5, (e) PTM5 and (f) comparative voltage for different films

Thereafter, Figure 6.6 (a-d) illustrates the unrectified and rectified voltage outputs generated by PTM1.2 device. The unrectified signal captures the intrinsic alternating nature of the piezoelectric response, whereas the rectified waveform confirms the effective conversion of the raw output using rectification circuit into a unidirectional voltage suitable for practical energy-harvesting applications. Moreover, the zoomed version of the waveforms in Figure 6.6 (c & d) clearly displays the primary piezoelectric spike associated to the pressing state or applied force. This large peak is followed by low-amplitude oscillations correlated to the release state, mechanical relaxation and damping factor.

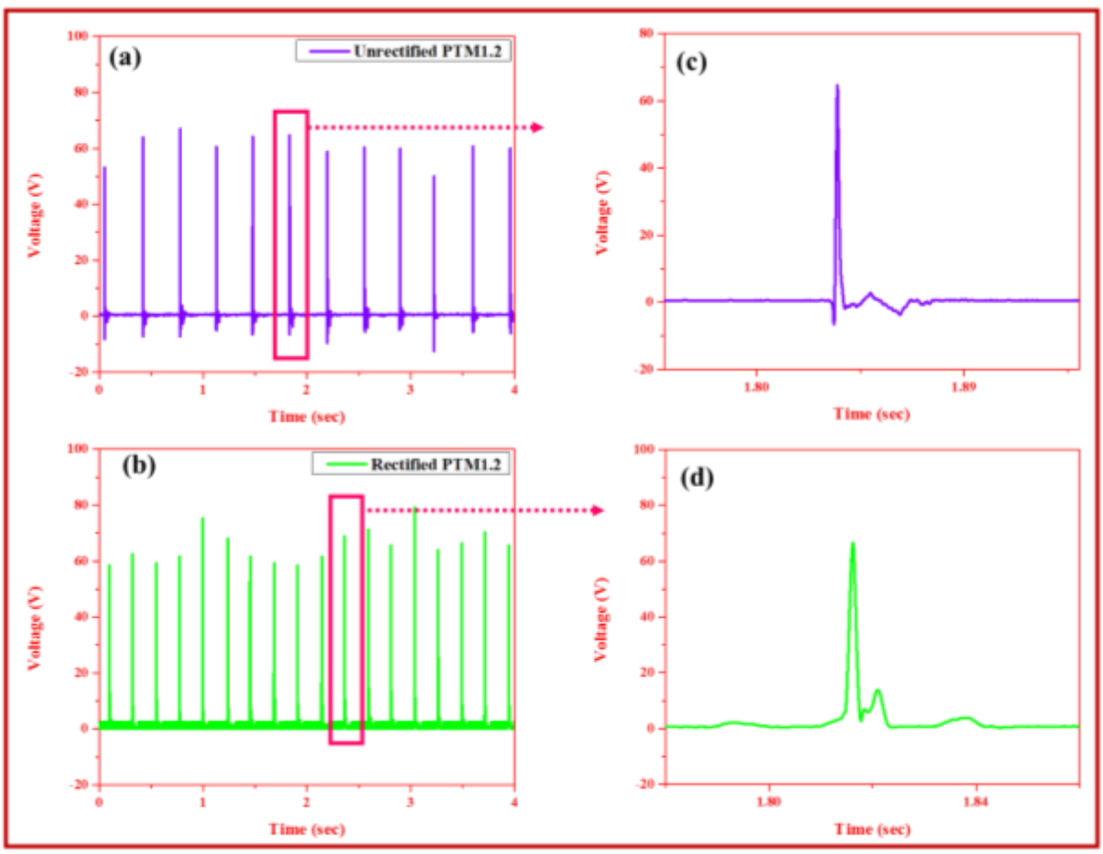

Figure 6.6 Generated voltage (a) unrectified/raw output, (b) rectified voltage output and single waveform for (c) unrectified and (d) rectified voltage data of PTM1.2 based PENG

In addition to the above measurements, the influence of load resistance on the output voltage, current and power management capabilities of the PTM1.2 based PENG device was evaluated. The output voltage was recorded across a series of load resistance and the result has been plotted in Figure 6.7 (a). Additionally, power density (P) has been calculated using equation 6.1, where V is the generated voltage output across the load resistance (R_L) and A is the cross-section area of the device [210].

The calculated power density with respect to load resistances has been illustrated in Figure 6.7 (b). The maximum power observed for the nanogenerator is ~0.125 mW/cm^2 (125 μW/cm^2) at an optimal load resistance of 1 MΩ. Moreover, the output current has been calculated using equation 6.2 illustrated in Figure 6.7 (a). As the load resistance increases, the output current decreases due to the finite internal resistance of the device, which limits charge transfer under higher electrical impedance. Further, to ensure the stability and durability of the fabricated PTM1.2 based piezoelectric nanogenerator, 500 cycles of mechanical stimulus were given to the nanogenerators and been illustrated Figure 6. 7 (c) without any serious degradation.

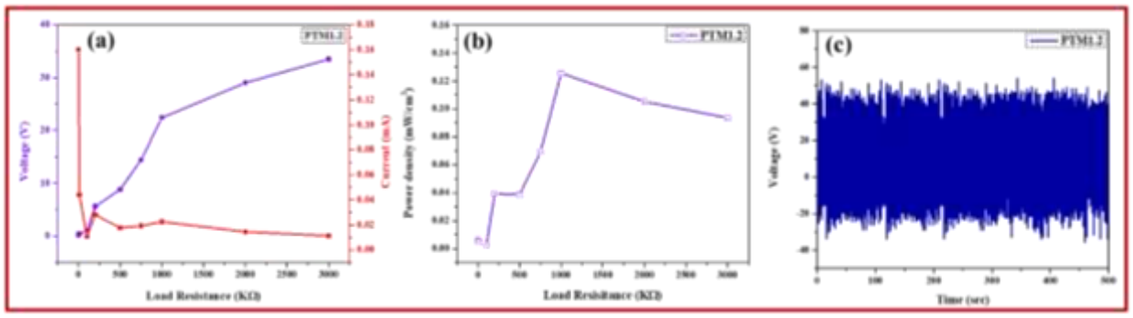

Figure 6.7 (a) Voltage output across different load resistance, (b) power density w.r.t. different load resistance and (c) stability curve of PTM1.2 based PENG

To check the practical viability of the fabricated PTM1.2 based PENG device in real world application, circuit has been constructed on a breadboard to demonstrate energy harvesting capability. The mechanical input applied to the PENG successfully actuate 11 commercially available LEDs. The live images of the lighted LEDs and has been displayed in Figure 6.8 (a & b). Furthermore, to quantify the energy storage capacity of the PTM1.2 based PENG, various capacitors (2.2 μF) has been charged using harvested mechanical energy. The voltage across the 1, 4.7 and 10 μF capacitors have reached upto 700, 590 and 400 mV within 80s, demonstrating the device's ability to efficiently charge mini energy storage units. The graph of generated voltage output across the capacitors has been shown in Figure 6.8 (c).

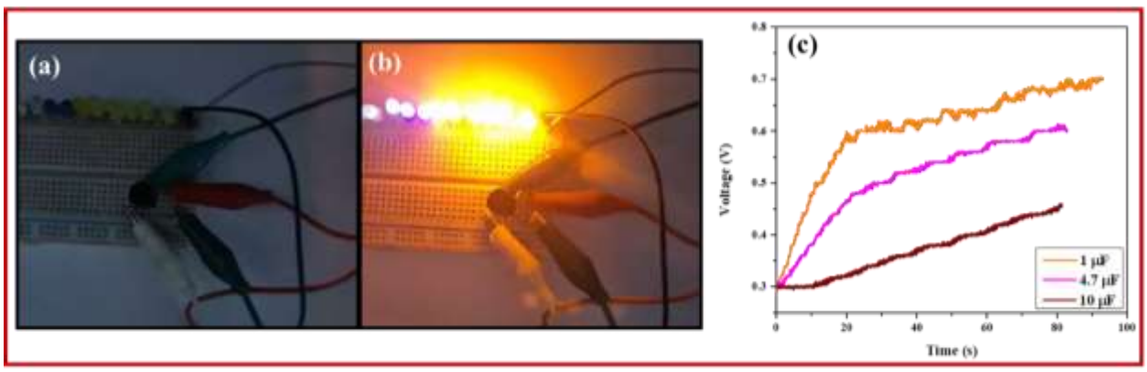

Figure 6.8 (a) Digital image of breadboard circuit for LEDs without mechanical force, (b) LEDs glowing on applying mechanical force, (c) Voltage output curve across capacitor 1, 4.7 and 10 μF

6.3 Triboelectric Nanogenerator (TENG)

6.3.1 Device Fabrication Process

To fabricate the TENG device, a contact-separation mode architecture has been employed, utilizing two triboelectric layers. A PVDF-based nanocomposite film served as one of the active triboelectric layers due to its strong electron-donating tendency and inherent dielectric properties. Indium tin oxide coated Polyethylene terephthalate (ITO-PET) film has been used as the counterpart triboelectric layer. Each triboelectric layer will be backed by a conductive electrode (Al foil). The two layers will be mounted face-to-face with a controlled air gap in between, enabling efficient contact and separation during operation. Cu wires have been attached to each electrode facilitating external electrical connection for output measurement. Upon mechanical impact or stress on fabricated device, open-circuit voltage and power output has been measured. A schematic diagram of fabrication process has been shown in Figure 6.9 (a).

6.3.2 Mechanism involved in TENG

The Vertical Contact-Separation mode has been selected as the primary mode configuration for the research presented in this thesis. The step-by-step cycle of Vertical Contact-Separation mode has been described and shown in Figure 6.9 (b). In the initial state (prior to mechanical stimulation), the surfaces are neutral, and no potential difference exists (Figure (i)). A dynamic shaker or palm tapping is used to compresses the layers. The overlapping electron clouds cause electrons to migrate from the ITO-PET layer to the MXene@Ta_2O_5/PVDF layer (Figure (ii)). As the mechanical force is released and the layers separate, a strong dipole moment is established. Because the polymer matrices are highly insulating, the charges cannot easily neutralize across the air gap. Instead, an electrical potential difference is induced across the corresponding metal electrodes, driving free electrons through the external circuit to balance the potential (Figure (iii)). Once maximum separation is reached, electrostatic equilibrium is achieved, and current ceases (Figure (iv)). Upon re-compression, the spatial gap closes, the induced potential diminishes, and electrons flow back through the external circuit in the opposite direction, generating an alternating current (AC) signal (Figure (v)) [173].

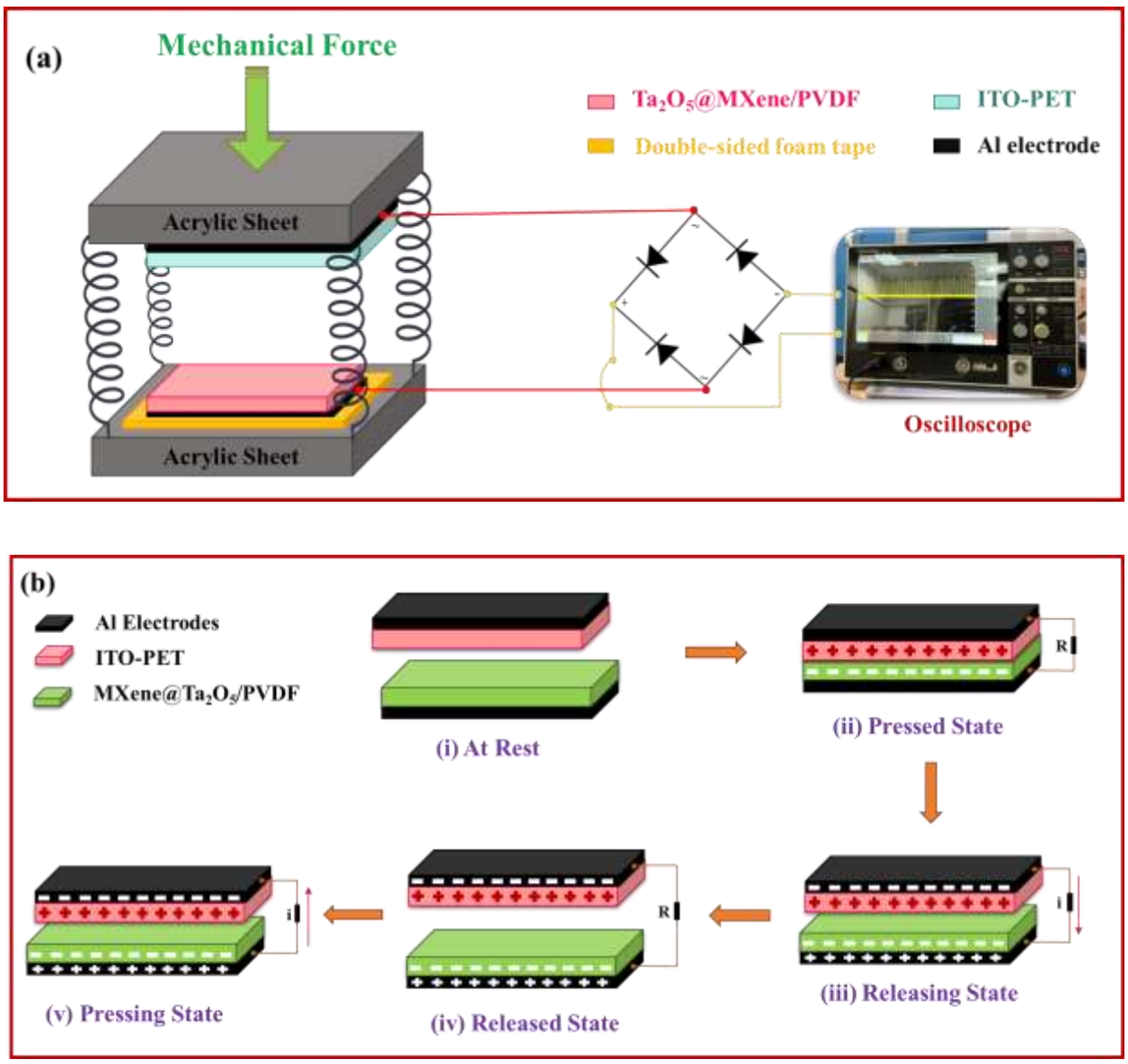

Figure 6.9 The schematic diagram of (a) fabrication and measurement and (b) mechanism involved in triboelectric nanogenerator (TENG)

6.3.3 Output Performance of Triboelectric nanogenerator (TENG)

Further, the nanocomposite film with the highest output voltage i.e, 1.25 wt% has been chosen to fabricate a TENG with the same dimensions (2x2 cm^2 (T2)). Figure 6.10 (a) depicts the voltage outputs for the TENG device. It has been observed that that voltage output of TENG enhanced ~2 times as compared to PENG device prepared with 1.25 wt% nanocomposite film.

Furthermore, triboelectric nanogenerators were prepared with two more different dimensions of film that are 3 x 3 cm^2 (T3) and 4 x 4 cm^2 (T4) to observe the variation in voltage influenced by the contact surface area. Figure 6.10 represents the voltage outputs for the three TENG devices with different surface areas. The output voltage of the TENG devices increases with the surface area of the films. The highest generated voltage has been observed for the T4 i.e, around 300 V.

This triboelectric output of T4 has improved because of the increased cross-sectional area of the film which resulted in the generation of more charges and a higher voltage output.

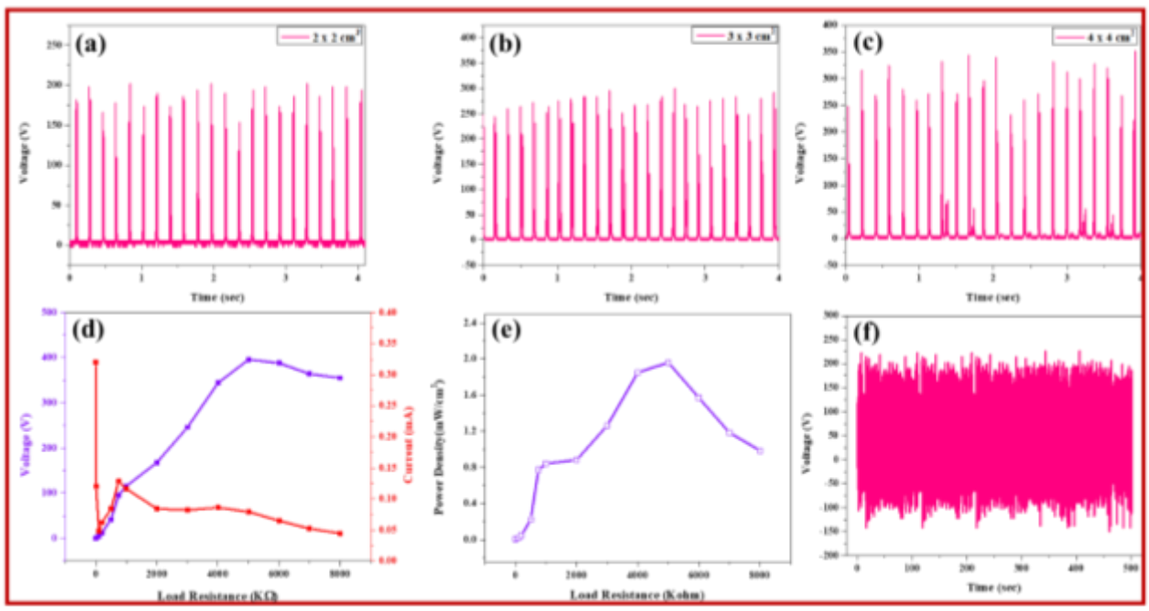

Figure 6.10 (a) Voltage generated by fabricated PTM1.2 based TENG with dimensions (a) 2 x 2 cm^2, (b) 3 x 3 cm^2, (c) 4 x 4 cm^2, (d) voltage output and (e) power density across different load resistance and (f) stability curve for 4 x 4 cm^2 PTM1.2 based TENG

In addition to the above measurements, the effect of load resistance variation on the output voltage and power density was also analyzed for the fabricated TENG (1.25 wt% nanocomposite film with 4x4 cm^2) device and the output has been represented in Figure 6.10 (d & e). The maximum power observed for the triboelectric output is ~2 mW/cm^2 (200 μW/cm^2) at a load resistance of 5 MΩ, respectively. Further, to ensure the stability and durability of the fabricated triboelectric nanogenerator, 500 cycles of mechanical stimulus were given to the nanogenerators and illustrated in Figure 6.10 (f).

6.4 Self-Charging Peizo-Supercapacitor (SCPC)

6.4.1 Electrodes preparation for SCPC

For working electrode, a slurry of the desired material i.e, MXene@Ta_2O_5 has been prepared. 10 mg of PVDF has been dissolved in 0.5 ml N-Methyl-2-pyrrolidone (NMP) and stirred on a magnetic stirrer till the solution becomes transparent. Then 90 mg of the MXene@Ta_2O_5 has been added to that solution followed with the continuous stirring to mix the slurry uniformly [46]. After the slurry preparation, slurry has been coated on a glassy carbon electrode (GCE) through drop

casting method and dried for several hours. The GCE coated with MXene@Ta_2O_5 utilized as a working electrode in the three-electrode system. The digital image of the setup used for the measurements has been shown in Figure.

6.4.2 Electrochemical Analysis

The electrochemical performance of the SCPC was evaluated using Bio-Logic SAS (VMP-3 model) electrochemical work-station with three electrode system including working, reference and counter electrode. The working electrode has been prepared using MXene@Ta_2O_5, a platinum wire acted as the counter electrode and Ag/AgCl was used as the reference electrode. This three-electrode system with 3 M KOH solution for electrolyte, was utilized to perform electrochemical measurements to evaluate the charge storage capability of the material for its potential application in self-charging supercapacitor systems. The cyclic voltammetry (CV) of MXene@Ta_2O_5 has been measured within an operation potential range of -1.5 V to +1.5 V at 5 mV/s scan rate and presented in Figure 6.11 (a). The obtained CV curve exhibited a non-rectangular and asymmetric shape with a prominent oxidation peak around +1.3V and a comparatively weak reduction peak near -0.6 V. The anodic peak current (I_{pa}) and cathodic current (I_{pc}) were observed to be ~ 0.517 mA and -0.0237 mA, respectively. The large difference between oxidation and reduction peak currents indicates partially irreversible electrochemical behaviour and polarization effects within the electrode system.

Further, the enclosed area under the CV curve represents the electrochemical charge storage capability of the electrode. The calculated area is ~ 0.16917 mAV. The stored charge (Q) was estimated using equation 6.3.

$$Q = \frac{1}{\nu} \int IdV \tag{6.3}$$

Where ν is the scan rate. The stored charge was calculated to be ~ 33.8 mC. The relatively large integrated area confirms enhanced electrochemical activity and significant charge accumulation capability of the SCPC [47]. The areal capacitance of the electrode was further estimated using equation 6.4.

$$C_a = \frac{\int I\, dV}{A\ \nu \Delta V} \tag{6.4}$$

Where A is the cross-sectional area of the working electrode. The calculated maximum areal capacitance was ~ 159 mF/cm^2 indicating effective charge storage behaviour over the small

geometrical area of GC electrode. This indicates that the MXene@Ta_2O_5 is a promising material for supercapacitor electrodes.

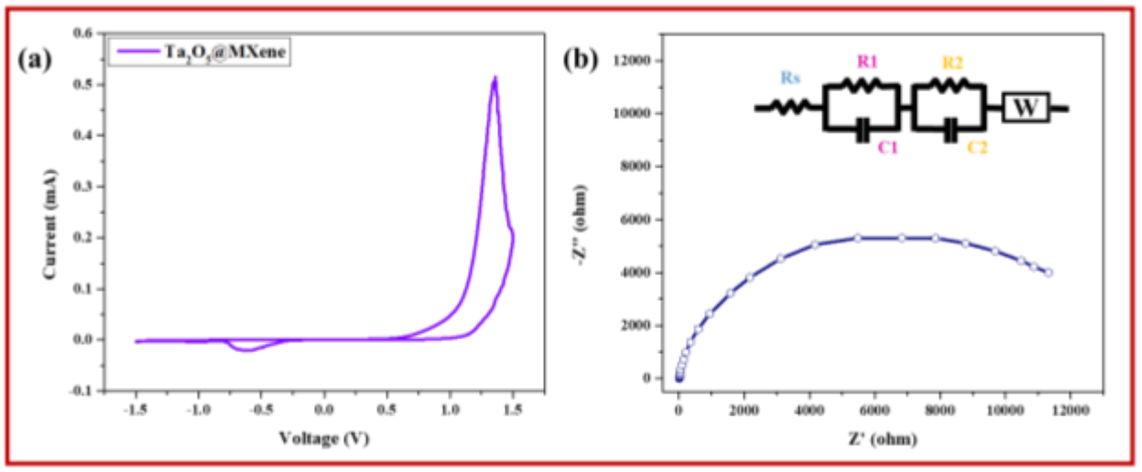

Figure 6.11 (a) CV curves at 5 mV/s and (b) EIS curve for MXene@Ta_2O_5 using three-electrode system

Electrochemical impedance spectroscopy (EIS) analysis was further carried out to evaluate the charge transport characteristics and interfacial resistance of the fabricated electrode. The Nyquist plot shown in Figure 6.11 (b) consists of a semicircular region in the high-frequency domain followed by a slanted line in the low-frequency region. The intercept at the real axis corresponds to the solution resistance (Rs), while the diameter of the semicircle represents the charge transfer resistance (R_{ct}). The low-frequency inclined line indicates ion diffusion behavior and capacitive characteristics of the electrode.

A relatively smaller R_{ct} value indicates efficient interfacial charge transfer and improved electrical conductivity due to the presence of highly conductive MXene nanosheets. The observed impedance behavior confirms that the MXene@Ta_2O_5/PVDF nanocomposite possesses favorable electrochemical kinetics and ion transport pathways, which are essential for high-performance energy storage applications.

The combined CV and EIS results confirm that the fabricated MXene@Ta_2O_5/PVDF nanocomposite exhibits promising electrochemical energy storage characteristics along with previously demonstrated piezoelectric and triboelectric energy harvesting performance. Therefore, the developed multifunctional nanocomposite material shows strong potential for future integration into self-charging piezo-supercapacitor systems capable of simultaneous mechanical

energy harvesting and electrochemical energy storage for next-generation wearable and portable electronic devices.

Conclusion

In summary, we have successfully fabricated the flexible piezoelectric and triboelectric energy harvesting nanogenerator. At an optimal nanofiller concentration of 1.25 wt%, the resulting Ta_2O_5@PVDF and MXene@Ta_2O_5/PVDF based PENGs exhibited a remarkable piezo performance enhancement, generating a voltage output of ~ 56V and 75 V that was twice and 2.5 times higher than that of the pristine PVDF based device, respectively. Further, MXene@Ta_2O_5/PVDF nanocomposite films has been used to fabricate TENG devices. Concurrently, the MXene@Ta_2O_5/PVDF based TENG demonstrated a nearly twofold increase in voltage output as compared to the PENG. Mechanistic investigations in the previous chapters using impedance spectroscopy confirmed the substantial improvement in the nanocomposite's overall dielectric properties, while FTIR unequivocally verified the intensified formation and stabilization of the highly polar β-phase of PVDF, directly correlating these material improvements to the amplified electrical output.

Furthermore, the scalability of the TENG was demonstrated by systematically analyzing the effect of increasing device dimensions confirming that the voltage output scales linearly with the available cross-sectional area. Further, the measured power output i.e, ~33 μW/cm^2, 125 μW/cm^2 and ~200 μW/cm^2 for Ta_2O_5@PVDF, MXene@Ta_2O_5/PVDF based PENGs and MXene@Ta_2O_5/PVDF based TENG, respectively, across varying load resistances. Additionally, prepared nanogenerators have also demonstrated good results in practical applications confirm the devices' capability to efficiently drive low-power wearable electronics. Moreover, MXene@Ta_2O_5/PVDF has also been tested for its supercapacitor capabilities towards self-charging piezo-supercapacitor. It showed good areal capacitance of ~159 mF/g that suggest good energy storage potential. Collectively, prepared flexible nanogenerators are stable and scalable material solution for the next generation flexible and self-powered systems

CHAPTER 7

Conclusion, Future Scope & Social Impact

This chapter summarizes the key research outcomes based on the data obtained from preceding chapters of the thesis. Further, it outlines the future directions of the work, culminating in a discussion of the potential social and industrial impact of the research findings.

7.1 Conclusion

The rapid proliferation of wireless sensor networks, portable electronics, and the Internet of Things (IoT) has imposed severe limitations on traditional, battery-dependent power systems. To address the resulting energy constraints and environmental concerns, this thesis systematically investigated the design, synthesis, and optimization of flexible mechanical energy harvesting nanogenerators. By engineering advanced polymer nanocomposites through reinforcement of selective nanofillers in optimized concentration and self-sustained energy-harvesting devices, this research successfully established scalable pathways for converting ubiquitous ambient mechanical energy into reliable electrical power. The major conclusions drawn from the comprehensive experimental investigations are summarized as follows:

Tantalum pentoxide (Ta_2O_5) nanostructures were successfully synthesized via a hydrothermal process. Ta_2O_5 exhibited highly stable orthogonal phase in the calcination temperature range of 800-1200 ^{0}C. Further, at sintering temperature of 950 °C, Ta_2O_5 fundamentally enhanced its dielectric performance. The resulting nanostructures exhibit a substantially increased dielectric constant (40) and exceptionally low dielectric loss (< 0.025), driven by improved grain growth, thermally activated carriers, and enhanced interfacial polarization.

The synthesized has been further used as nanofillers in the PVDF matrix. The incorporating of Ta_2O_5 into PVDF matrix at optimized concentration of 1.25 wt% successfully yields flexible nanocomposite films with superior dielectric and mechanical properties. Driven by magnified interfacial polarization and retained polymer crystallinity. The optimal film exhibited a seven-fold increase in dielectric constant alongside significantly enhanced tensile strength (~21 MPa) and remarkably reduced the dissipation loss.

A novel 2D MXene was further used to prepared a heterostructure with Ta_2O_5. The synthesized MXene@Ta_2O_5 was further reinforced homogeneously into PVDF matrix. Systematic characterizations revealed that the incorporated nanofillers significantly enhance the dielectric constant of the nanocomposite by fundamentally intensifying interfacial polarization. Consequently, this amplified polarization successfully promotes the nucleation of the highly polar electroactive β-phase while maintaining mechanical integrity.

The prepared nanocomposite films were utilized to prepare PENG devices. the resulting Ta_2O_5@PVDF and MXene@Ta_2O_5/PVDF based PENGs exhibited a remarkable piezo performance enhancement, generating a voltage output of ~ 56V and 75 V that was twice and 2.5 times higher than that of the pristine PVDF based device, respectively. Further, MXene@Ta_2O_5/PVDF nanocomposite films has been used to fabricate TENG devices. Concurrently, the MXene@Ta_2O_5/PVDF based TENG demonstrated a nearly twofold increase in voltage output as compared to the PENG. The versatility and scalability of the technology were further validated through real time applications, with both device architectures generating substantial power densities capable of efficiently driving low-power wearable electronics.

Further, the optimized nanogenerators were integrated with supercapacitors to overcome the inherently intermittent power output generated from mechanical stimuli. Expanding beyond continuous energy generation, the heterostructure also exhibited strong energy storage potential for self-charging piezo-supercapacitors, evidenced by a robust areal capacitance of ~159 mF/g.
The successful formulation of a self-charging piezo-supercapacitor can effectively buffer fluctuating voltages, providing a stable, regulated output. These findings establish the MXene@Ta_2O_5/PVDF nanocomposite as a highly stable, flexible, and scalable material paradigm for next-generation autonomous self-powered systems.

7.2 Future Aspects and Scope of Work

The fundamental material strategies and device architectures established in this thesis lay a robust foundation for next-generation flexible electronics. This research opens several promising avenues for continued exploration:

- **Advanced Material Engineering and Morphological Optimization**

  The synthesized combination of nanofillers and the developed nanogenerators in this work provides a versatile blueprint for further nanofiller engineering. Future research can explore a broader spectrum of 0D/2D heterostructures by testing novel combinations of MXene with different nanofillers with good dielectric properties. Additionally, exploring different crystallographic phases or varied structural morphologies of Ta_2O_5 (such as nanorods, nanowires, nanofibers or mesoporous spheres) could yield entirely new insights

into interfacial polarization and β-phase nucleation. Beyond chemical composition, advanced physical surface engineering such as utilizing targeted ion irradiation to precisely tune the surface roughness and electron affinity of the polymer films, presents a massive scope for maximizing the triboelectric and piezoelectric output of the nanocomposites. Future work could also integrate machine learning algorithms to predict the optimal weight percentages, best nanofiller morphologies, and triboelectric material pairings, significantly reducing trial-and-error laboratory optimization.

- **Industrial Upscaling**
- While the current flexible nanogenerators demonstrate exceptional efficiency at the laboratory scale, a critical next step is transitioning these devices toward industrial manufacturing. Future research must focus on scaling up the fabrication process (ex., utilizing continuous roll-to-roll printing techniques) to make commercial deployment viable. After large scale production, there is immense scope for integrating these nanogenerators into everyday microelectronics and smart wearables where instantaneous power is required. By embedding these flexible energy harvesters into smartwatches, biometric clothing, or intelligent shoe soles, they can reliably scavenge biomechanical energy to provide continuous, battery-free power for remote IoT sensors and real-time healthcare monitoring systems.
- **Advancement in Integrated Self-Charging Peizo-Supercapacitors (SCPCs)**

  A highly ambitious and promising path for this research is the evolution from isolated energy generation to fully integrated energy storage. The synthesized Ta_2O_5@MXene/PVDF nanocomposites exhibit good dielectric properties and great energy capacitance, providing strong evidence for their potential as energy storage units. Future research should heavily focus on engineering single Self-Charging Piezo-Supercapacitors (SCPCs) that utilize these specific nanocomposites to simultaneously harvest ambient mechanical energy and store it electrochemically within the same flexible device. Significantly advancing the charge retention capabilities of these materials for long-term power storage will bridge the ultimate gap in creating truly autonomous, self-powered microelectronic ecosystems.

Advanced AI-Driven Material Optimization: The parameter space for nanocomposite engineering is vast. Future work could integrate machine learning algorithms to predict the optimal weight

percentages, filler geometries, and triboelectric material pairings, significantly reducing trial-and-error laboratory optimization.

7.3 Social and Environmental Impact

The technological advancements presented in this thesis extend far beyond fundamental laboratory research. The development of high performance, flexible nanogenerators carries profound implications for environmental sustainability and socioeconomic evolution of smart societies. The broader impacts of this research are outlined below:

- **Environmental Sustainability and E- waste Control:**

  Traditionally, portable electronics relies heavily on conventional chemical batteries which contain hazardous heavy metals (such as lithium, lead etc.) and toxic electrolytes that leach into soil and groundwater. The disposal of these batteries annually has created a global electronic waste crisis. The nanogenerators developed in this work utilize an eco-friendly approach and lead-free material selection (PVDF, Ta_2O_5, and MXene). Furthermore, by successfully harvesting wasted mechanical energy and converting it into a renewable electrical power source, these devices offer a zero-emission technology. By replacing the batteries with the mechanical energy harvesters, technologies developed in this thesis directly contributes to a drastic reduction in toxic e-waste and environmental degradation caused by heavy-metal mining.

- **Improving Living Standards and Revolutionizing Healthcare:**

  Society's dependency on small and portable devices, such as smartwatches, fitness trackers, and continuous health-monitoring systems is increasing day by day. However, physical burden associated with constantly recharging batteries have become significant limitations. The flexible nanogenerators engineered in this thesis have the potential to render these small-scale electronics entirely self-powered. By harvesting the ubiquitous biomechanical energy of human motion (ex., walking, hand movement, or heartbeat vibrations), these devices can ensure uninterrupted, autonomous operation of wearable electronics. This no recharging capability drastically improves the standard of living by integrating technology seamlessly into daily life. Where it can also offer life-saving reliability for critical medical implants and continuous patient monitoring.

- **Accessibility of Technology in Remote Areas:**

  A significant social barrier in developing the nation is the lack of reliable electrical grid infrastructure in rural or remote geographic regions. As the proposed nanogenerators operate entirely independently of centralized power grids, they possess immense potential to democratize technology. They can provide localized power for essential low-power devices, such as agricultural soil sensors, remote weather indicators, and point-of-care medical diagnostic tools ensuring that off-grid communities in rural or remote areas are not left behind in the digital and healthcare revolutions.

- **Alignment with Government of India Strategic Missions:**

  The outcomes of this research align strongly with several ongoing national missions. For example, “Make in India & Aatmanirbhar Bharat (Self-Reliant India)”. By developing scalable and efficient nanogenerators for flexible electronics, this research contributes to domestic technological capacity that reduce reliance on imported, expensive rare-earth materials and commercial electronic components.

  The Another example is “Digital India & Smart Cities Mission”. The realization of a fully connected Digital India requires billions of distributed Internet of Things (IoT) sensors to monitor urban infrastructure, agriculture, and environment. Providing a decentralized, self-sustaining power source for these remote IoT nodes directly empower the Smart Cities infrastructure.

  This research also aligns with the “Panchamrit and Net-Zero Goals by 2070” of India. By utilizing ambient mechanical vibrations as a localized renewable energy source, this technology supports India’s ambitious climate action targets pledged at COP26, contributing to the broader decarbonization of the micro-electronics sector.

References